UC Merced
UC Merced Electronic Theses and Dissertations

Title

Mathematical and physical modeling of reactive gas dynamics and aggregation dynamics at small scales

Permalink

https://escholarship.org/uc/item/7kx4h9j5

Author

Polimeno, Matteo

Publication Date

2024

Peer reviewed|Thesis/dissertation

UNIVERSITY OF CALIFORNIA, MERCED

Mathematical and physical modeling of reactive gas dynamics and aggregation dynamics at small scales

A dissertation submitted in partial satisfaction of the
requirements for the degree Doctor of Philosophy

in

Applied Mathematics

by

Matteo Polimeno

Committee in charge:

    Changho Kim, Chair

    François Blanchette, Co-Chair

    Shilpa Khatri

    Andrew Nonaka

2024

The dissertation of Matteo Polimeno is approved, and it is acceptable in quality and form for publication on microfilm and electronically:

_____
(Shilpa Khatri)

_____
(Andrew Nonaka)

_____
(François Blanchette, Co-Chair)

_____
(Changho Kim, Chair)

University of California, Merced

2024

TABLE OF CONTENTS

LIST OF FIGURES

LIST OF TABLES

ACKNOWLEDGEMENTS

MATTEO POLIMENO

Curriculum Vitae

mpolimeno@ucmerced.edu

RESEARCH INTERESTS

Modeling of Multi-Physics Multi-Scale Systems. Fluid Dynamics, Stochastic Processes, Partial Differential Equations, Data-driven Numerical Methods, Scientific and High Performance Computing.

EDUCATION

University of California, Merced   Fall 2019 - Spring 2024 (Expected)
Ph.D. Candidate in Applied Mathematics   *Merced, CA*

- Thesis: Mathematical and physical modeling of reactive gas dynamics and aggregation dynamics at small scales
- Advisors: Prof. Changho Kim, Prof. François Blanchette

San Diego State University   2017-2019
Master of Science in Applied Mathematics   *San Diego, CA*

- Concentration: Dynamical Systems
- Thesis: Characterizing Coherent Structures in Bose-Einstein Condensates: A DMD Approach
- Advisor: Prof. Christopher Curtis

PUBLICATIONS

M. Polimeno, C. Kim, and F. Blanchette, "Toward a realistic model of diffusion-limited aggregation: rotation, size-dependent diffusivities, and settling", ACS Omega **7**, 40826–40835 (2022).

C. W. Curtis, R. Carretero-González, and **M. Polimeno**, "Characterizing coherent structures in Bose-Einstein condensates through dynamic-mode decomposition", Phys. Rev. E **99**, 062215 (2019).

MANUSCRIPTS IN PREPARATION

M. Polimeno, C. Kim, I. Srivastava, A. Nonaka, J. B. Bell, A. L. Garcia, and F. Blanchette, "Thermodynamic consistency and fluctuations in mesoscopic stochastic simulations of reactive gas mixtures".

Awards and Fellowships

Graduate Dean's Dissertation Fellowship   Spring 2024
Graduate Division, UC Merced   *Merced, CA*

Applied Mathematics Excellence in Research Award   Spring 2023
Department of Applied Mathematics, UC Merced   *Merced, CA*

Best Graduate Poster Presentation Award   Spring 2023
Central Valley Regional SIAM Student Chapter Conference   *Merced, CA*

Sustainable Research Pathways Fellowship   Summer 2021, Summer 2022
Lawrence Berkeley National Laboratory   *Berkeley, CA*
- Sustainable Horizon Institute Summer Research Internship at Lawrence Berkeley National Laboratory

Research Experience

Affiliate   Summer 2022
Lawrence Berkeley National Laboratory   *Berkeley, CA*
Mentor: Dr. Andrew Nonaka   Full-time
- Incorporation of mean-field surface chemistry into the framework of fluctuating hydrodynamics
- Extensive use of the AMReX library

Affiliate   Summer 2021
Lawrence Berkeley National Laboratory   *Berkeley, CA*
Mentor: Dr. Andrew Nonaka   Full-time
- Incorporation of reactive stochastic chemistry into fluctuating hydrodynamics of gas mixtures
- Extensive use of the AMReX library

Teaching Experience

Teaching Assistant for Calculus II   Fall 2023
University of California, Merced   *Merced, CA*

Teaching Assistant for Vector Calculus   Spring 2023
University of California, Merced   *Merced, CA*

Teaching Assistant for Probability and Statistics   Fall 2022
University of California, Merced   *Merced, CA*

Teaching Assistant for Linear Algebra & Differential Equations   Spring 2021
University of California, Merced   *Merced, CA*

Teaching Assistant for Vector Calculus   Fall 2019, Spring 2020, Fall 2020
University of California, Merced   *Merced, CA*

Teaching Assistant for Calculus II   Fall 2018, Spring 2019
San Diego State University   *San Diego, CA*

SERVICE

Ad-hoc journal reviewer   Fall 2023
University of California, Merced   *Merced, CA*
  - Journal of Geophysical Research

Peer Code Review Initiative   Spring 2023 – Present
University of California, Merced   *Merced, CA*
  - Co-founded the Peer Code Review Initiative for the Applied Math Department at UC
    Merced to improve the maintainability and reproducibility of research software
    amongst graduate students, via GitHub Teams. This activity is supported by the
    UC Merced's NSF RTG grant.

Peer Mentoring   Fall 2023 – Present
University of California, Merced   *Merced, CA*
  - Peer mentoring of second-year graduate student to help them get familiar with the
    best practices of code development for scientific research

Math and Computer Science Research Engagement (MCoRE)   Summer 2023
University of California, Merced   *Merced, CA*
  - Mentoring local high school students from under-represented minorities
    participating in the MCoRE initiative, and guiding them through their research on a
    data science project culminated in a poster presentation

SELECTED CONFERENCE PRESENTATIONS

M. Polimeno, "A boundary integral approach to breaking up marine aggregates", APS
Annual Meeting of the Division of Fluid Dynamics, Washington, D.C., Nov. 2023.

M. Polimeno, "Thermodynamically-consistent formulation of stochastic chemistry for
modeling reactive gas dynamics at small scales", APS March Meeting, Las Vegas (NV),
Mar. 2023.

M. Polimeno, "Characterizing the growth rate and fractal dimension of aggregates formed
through Brownian dynamics", SIAM Annual Meeting, Pittsburgh (PA), July 2022.

M. Polimeno, "Modeling the formation mechanism and growth rate of aggregates through
Brownian dynamics", APS Annual Meeting of the Division of Fluid Dynamics, Phoenix
(AZ), Nov. 2021.

PROFESSIONAL MEMBERSHIPS

Society for Industrial and Applied Mathematics (SIAM): Member since 2020

American Physical Society (APS): Member since 2020

ABSTRACT OF THE DISSERTATION

Mathematical and physical modeling of reactive gas dynamics and aggregation dynamics at small scales

by Matteo Polimeno

Doctor of Philosophy in Applied Mathematics

University of California Merced, 2024

Committee Chair: Changho Kim

This thesis aims to characterize the behavior of reactive gas mixtures and aggregate dynamics at small scales. Since at scales ranging from nanometers to micrometers fluids are discrete systems made of individual particles, the full characterization of their dynamics requires modeling approaches capable of capturing both the mean behavior of the fluid and the impacts of thermal fluctuations due to random molecular motion. Here I present three different approaches to model fluid systems at small scales in a physically-accurate, mathematically-sound and computationally-efficient manner.

First, I discuss how to model the dynamics of reactive gas mixtures at the mesoscopic scale in a thermodynamically consistent manner. To this end, I incorporate a chemical Langevin equation approach into the framework of fluctuating hydrodynamics (*continuum stochastic* approach). I find that in order to obtain physically accurate results, one needs to fully characterize the temperature dependence of the rate constants of a chemical reaction. I validate this formulation by simulating a reversible dimerization reaction and characterize the spectrum of fluctuations at thermodynamic equilibrium.

Secondly, I discuss a Brownian dynamics formulation (*particle-based* approach) to model the formation of aggregates. I incorporate rotational effects, size-dependent diffusivities and settling under gravity into the well-established framework of Diffusion-Limited Cluster Aggregation. I characterize how the inclusion of rotational effects and settling lowers the fractal dimension typically found in aggregates, while size-dependent diffusivities slow down their growth rate.

Finally, I discuss a boundary integral formulation to solve the Stokes Equations (*continuum deterministic* approach) to characterize the internal and external stresses felt by different types of marine aggregates settling under gravity or exposed to some laminar shear flow. I find that the internal stresses induced by gravity distribute differently in aggregates compared to those induced by a shear flow, leading to different breakup distributions. Furthermore, I find that the largest stress felt by aggregates exposed to a shear background flow shows a quadratic dependence on the aggregate's radius, indicating that the contribution of extensional effects on the stresses is dominant over rotational effects.

Chapter 1

Introduction

In recent years, due in part to modern technological advances and the on-going miniaturization of many engineering devices, the modeling of fluid systems at small scales has become more prominent with the fluids community [80]. It is well known that at scales ranging from nanometers to micrometers, fluids are discrete systems made of individual particles [14], and thus the full characterization of their dynamics requires modeling approaches capable of balancing the need for high fidelity and computational efficiency [110]. Typically, these modeling efforts subscribe to one of the following two paradigms: the *discrete approach*, where one keeps track of individual fluid particles [64], or the *continuum approach*, which is based on the averaging of fluid properties over a volume [27]. Both approaches present advantages and drawbacks, and can be used to model a plethora of multi-scale [88] and multi-physics [31] fluid phenomena, in scientific domains spanning from biophysics [12] to nanotechnology [86].

The discrete approach, which typically includes so-called *particle-based methods* like Direct Simulation Monte Carlo [4], naturally captures thermal fluctuations caused by the random molecular motion of fluid particles [20]. Thus, it allows for great accuracy in the description of systems even at the atomic scale [97], and is often used in fields like biology and biophysics [33], where capturing the effects of said fluctuations is paramount to building physically accurate models. This framework is well-suited to describe various physical phenomena, from the formation of fractal aggregates in the ocean [74], to granular flow [96]. However, given the level of refinement that particle-based methods typically require, they tend to give rise to computationally intensive and poorly-scalable algorithms, which severely limits the size of the systems that can be analyzed, even on modern distributed architectures [3].

Conversely, the continuum approach is used to characterize the macroscopic behavior of fluid systems by modeling the dynamical evolution of fluids' properties like density

1

and momentum. This approach typically relies on numerically solving a set of Partial Differential Equations (PDEs) known as the incompressible Navier-Stokes equations,

$$\nabla \cdot \mathbf{u} = 0,$$
$$\rho \left(\frac{\partial \mathbf{u}}{\partial t} + (\mathbf{u} \cdot \nabla) \mathbf{u} \right) = \mu \nabla^2 \mathbf{u} - \nabla P + \mathbf{f}, \tag{1.1}$$

where $\vec{u}$ and P are the unknown velocity and pressure of the fluid, respectively, μ is the dynamic viscosity, ρ is the fluid density, and $\vec{f}$ is a body force. Many numerical schemes have been designed to solve Eq. (1.1), spanning from finite-difference methods [67] to finite-volume schemes [68]. These techniques are typically used to characterize fluid systems at large scales, such as to study the flow physics governing wind farms performance [89]. At small scales, however, viscous effects are often dominant over inertial effects, and one can simplify Eq. (1.1) to obtain a linear system of PDEs known as the Stokes Equations

$$\nabla \cdot \mathbf{u} = 0$$
$$-\nabla P + \mu \nabla^2 \mathbf{u} + \mathbf{f} = 0. \tag{1.2}$$

Eq. (1.2) is often used to describe fluid flows in the so-called *low Reynolds number regime*, where the Reynolds number is the non-dimensional ratio between inertial forces and viscous forces in a fluid [61], and it is defined as follows

$$Re = \frac{\rho U L}{\mu}. \tag{1.3}$$

Here U and L are some characteristic velocity and length, respectively. For instance, Stokes Equations can be used to characterize the flow around solid objects via boundary integral methods [83], and thus applied to problems that involve some solid boundary at small scales, as in sedimentation [42], like computing the hydrodynamic forces around marine aggregates [106].

Moreover, continuum methods typically do not require refinement to the level of particle-based methods, and thus tend to be more efficient and better scalable than discrete approaches [38]. As such, they provide a rich environment for the optimization of modern high-performance computing applications in the context of fluid dynamics simulations [8]. However, these methods are *deterministic* and designed to model the mean behavior of fluids. Thus, they are usually not capable of capturing the impact of thermal fluctuations arising from random molecular motion of fluids particles. Since simulations of fluid flows have been pushing towards ever-shrinking scales, the discrete nature of fluids should not be neglected *a priori*. It has become imperative, for instance, to build accurate models of reactive fluid systems, where *nonlinearity* interacts with

spontaneous fluctuations, such as combustion [66] and reaction fronts [78]. In fact, in some experimental settings, it was shown that long-ranged correlations in the fluctuations of concentration and temperature in the presence of sharp gradients, give rise to fluctuations that grow well beyond the microscopic scale [98]. Thus, and especially for reactive systems, capturing thermal fluctuations is paramount to modeling the dynamics of fluids at small scales. To this end, one can take advantage of a *continuum-stochastic approach* called fluctuating hydrodynamics.

Fluctuating hydrodynamics (FHD) is a well-established [63] framework to model fluid mixtures at the mesoscale, where thermal fluctuations play a significant role. To capture the aforementioned fluctuations, a stochastic forcing term is added to the dissipative fluxes in the conservation equations of Navier-Stokes, to obtain the so-called Fluctuating Navier-Stokes (FNS) equations [13] for the time evolution of a species density, ρ_s, momentum density $\rho\vec{u}$ and energy density ρE:

$$\frac{\partial \rho_s}{\partial t} = -\nabla \cdot (\rho_s \mathbf{u}) - \nabla \cdot \boldsymbol{\mathcal{F}}_s, \tag{1.4a}$$

$$\frac{\partial (\rho \mathbf{u})}{\partial t} = -\nabla \cdot (\rho \mathbf{u}\mathbf{u}^T) - \nabla P - \nabla \cdot \boldsymbol{\Pi}, \tag{1.4b}$$

$$\frac{\partial (\rho E)}{\partial t} = -\nabla \cdot (\rho E \mathbf{u} + P\mathbf{u}) - \nabla \cdot \boldsymbol{\mathcal{Q}} - \nabla \cdot (\boldsymbol{\Pi} \cdot \mathbf{u}). \tag{1.4c}$$

Here $\boldsymbol{\mathcal{F}}_s$, $\boldsymbol{\Pi}$, and $\boldsymbol{\mathcal{Q}}$ are fluxes for the species's mass, momentum, and heat densities, respectively, defined as the sum of a deterministic and stochastic part denoted with the overline and tilde notation, respectively

$$\boldsymbol{\mathcal{F}}_s = \overline{\boldsymbol{\mathcal{F}}}_s + \widetilde{\boldsymbol{\mathcal{F}}}_s, \quad \boldsymbol{\Pi} = \overline{\boldsymbol{\Pi}} + \widetilde{\boldsymbol{\Pi}}, \quad \boldsymbol{\mathcal{Q}} = \overline{\boldsymbol{\mathcal{Q}}} + \widetilde{\boldsymbol{\mathcal{Q}}}. \tag{1.5}$$

The deterministic fluxes are specified by functions of fluid state variables (i.e. ρ_s, $\mathbf{u}$, and the temperature T) by constitutive relations, while the stochastic fluxes are modeled by Gaussian white noise fields with the noise intensities being functions of fluid state variables. Thus, this method allows to still maintain the inherent computational efficiency of the deterministic continuum approach, while also capturing thermal fluctuations without requiring refinement to the level of particle-based methods. In fact, this formulation has been validated numerically many times [18, 94], and it has even been integrated into the FHDeX software [16], a massively-parallelized and GPU friendly suite of codes built under the Adaptive-Mesh Refinement for Exascale (AMReX) library, developed as part of the exascale computing project [77]. Furthermore, as will be shown in Chapter 2, FHD is particularly well-suited to model *reactive* fluid systems at small scales, where taking into account the stochastic nature of chemical reactions, as well as nonlinear kinetic effects, is paramount to build physically-accurate models.

In the remainder of this thesis, I will show how each of the three aforementioned approaches can be used to model various fluid systems at small scales. The structure of this thesis is as follows: in Chapter 2, I will show how fluctuating hydrodynamics can be used to model the dynamics of a reactive ideal gas mixture undergoing a reversible dimerization reaction at the mesoscopic scale. This work was conducted as part of a collaborative effort with the Multiscale Modeling and Stochastic Systems group at Lawrence Berkeley National Laboratory, and its results are being collected into a manuscript to be submitted to the *Journal of Chemical Physics* in the Summer of 2024. In Chapter 3, I will describe our particle-based method to simulate the formation of fractal aggregates in low Reynolds number regimes, and characterize the aggregates' growth rate and fractal dimension under different conditions. This work was conducted at UC Merced alongside my advisors Profs. Changho Kim and François Blanchette, and led to a publication in *ACS Omega* in October 2022 [82]. In Chapter 4, I will discuss a boundary-integral formulation to solve the Stokes Equations and characterize both the internal and external stresses in marine aggregates. I will show that the internal stresses induced by gravity distribute differently in aggregates compared to those induced by a shear flow, leading to different breakup distributions. The results of this work are being collected into a manuscript to be submitted for publication to *Physics Review Fluids* in the Summer of 2024. Finally, Chapter 5 contains the Conclusions.

Modeling Reactive Gas Dynamics: A Fluctuating Hydrodynamics Approach

2.1 Introduction

Stochastic modeling of chemical reactions was first popularized in the 1970's with the introduction of birth-death models based on the master equation [101]. These led to continuum formulations such as the Fokker-Planck and Langevin equations [100, 99], whose popularity was further enhanced by the introduction of Gillespie's Stochastic Simulation Algorithm (SSA) [40]. These models were originally limited to homogeneous systems, such as the Continuously Stirred Tank Reactor (CSTR), yet experiments [108] showed that systems with spatial extent produced interesting patterns, such as spiral waves. Therefore, species diffusion was incorporated both in continuum-deterministic models, such as those based on on the reaction-diffusion equation, and in stochastic models, such as those based on random walks.

More recently, the framework of reactive fluctuating hydrodynamics (RFHD) was used to model the transport and flow in fluid systems with chemical reactions [55] combining continuum and stochastic features of previous models. However, it is non-trivial to ensure that reactive fluctuating hydrodynamics simulations, for example in the context of reactive gas mixtures, is implemented in a thermodynamically consistent manner. It is essential that mesoscopic simulations of reactive systems reproduce the correct statistical distributions at thermodynamic equilibrium. Previously, Bhattacharjee et al. [18] presented a RFHD-based framework to model the dynamics of reactive gas mixtures. However, the formulation proposed in [18] does not account for the effect that fluctuating temperature in reactive gas mixtures has on the expression of the rate

constants, and it is thus not thermodynamically consistent.

In this Chapter we consider a fluctuating hydrodynamics simulation method of an ideal gas mixture undergoing reversible reactions described by the chemical Langevin equation. We present a rigorous analysis of a novel formulation that is thermodynamically-consistent and demonstrate that we are able to properly capture the spectrum of fluctuations in realistic gas mixtures, by correctly characterizing the temperature dependence of the rate constants of chemical reactions. The rest of this Chapter is organized as follows. In Section 2.2 we briefly explain the framework of RFHD. In Section 2.3 we provide the details of our formulation of stochastic chemistry. In Section 2.4 we show the accuracy of our formulation, by studying a simple dimerization reaction. Finally, Section 2.5 contains our Conclusions.

2.2 Reactive Fluctuating Hydrodynamics

In Section 2.2.1, we summarize the overall structure of the reactive fluctuating hydrodynamics formulation [13, 18] that provides the framework for our thermodynamically-consistent stochastic chemistry formulation. In Section 2.2.2, we focus on the reactive source term and discuss how it can be modeled using a chemical Langevin equation [56, 55].

2.2.1 Overall Structure

For a gas mixture of N_{spec} species, we denote the species mass densities and the total mass density as ρ_s ($s = 1, \cdots, N_{\text{spec}}$) and $\rho = \sum_{s=1}^{N_{\text{spec}}} \rho_s$, respectively, and the fluid velocity and the total specific energy (i.e. energy per mass) as $\mathbf{u}$ and E, respectively. The time evolution of the species mass densities (ρ_s), momentum density ($\rho\mathbf{u}$), and energy density (ρE) is described by the fluctuating Navier–Stokes (FNS) equations given in Eqs. (1.4) supplemented by a reaction term [13, 18]:

$$\frac{\partial \rho_s}{\partial t} = -\nabla \cdot (\rho_s \mathbf{u}) - \nabla \cdot \boldsymbol{\mathcal{F}}_s + M_s \Omega_s, \tag{2.1a}$$

$$\frac{\partial (\rho \mathbf{u})}{\partial t} = -\nabla \cdot (\rho \mathbf{u}\mathbf{u}^T) - \nabla P - \nabla \cdot \boldsymbol{\Pi}, \tag{2.1b}$$

$$\frac{\partial (\rho E)}{\partial t} = -\nabla \cdot (\rho E \mathbf{u} + p\mathbf{u}) - \nabla \cdot \boldsymbol{\mathcal{Q}} - \nabla \cdot (\boldsymbol{\Pi} \cdot \mathbf{u}). \tag{2.1c}$$

Here, $M_s \Omega_s$ is the reaction source term where M_s is the molar mass of species s and Ω_s is the molar concentration production rate of species s due to the chemical reactions associated with species s. This term will be discussed in more detail in Section 2.2.2.

As discussed in Chapter 1, while Eqs. (2.1) may superficially look the same as the deterministic Navier–Stokes equations, the species mass flux $\mathcal{F}_s$, the momentum flux $\mathbf{\Pi}$ and the heat flux $\mathcal{Q}$ are modeled via Eq. (1.5) as the sum of a deterministic and stochastic component, whose explicit forms are given in Ref. [13]. Thus, Eqs (2.1) account for both the mean behavior of a fluid, as well as the thermal fluctuations due to random molecular motion of fluid particles.

Note that the relation between the total specific energy E and the temperature T is given by

$$E = \frac{1}{2}|\mathbf{u}|^2 + e(T, \{\rho_s\}).$$

(2.2)

Here, the total specific internal energy $e = e(T, \{\rho_s\})$ is a function of temperature and chemical composition. In this paper, we assume an ideal gas mixture, for which we can simply express e as the weighted sum of the specific internal energy of each species e_s:

$$e(T, \{\rho_s\}) = \frac{1}{\rho} \sum_{s=1}^{N_{\text{spec}}} \rho_s e_s(T).$$

(2.3)

Note that the e_s's are functions of temperature and their functional forms are provided as modeling inputs. In addition, the equation of state is given by the ideal gas law:

$$P_s = \frac{\rho_s RT}{M_s}, \quad P = \sum_{s=1}^{N_{\text{spec}}} P_s = RT \sum_{s=1}^{N_{\text{spec}}} \frac{\rho_s}{M_s},$$

(2.4)

where P_s is the partial pressure of species s and R is the ideal gas constant.

2.2.2 CLE-based Stochastic Chemistry

We assume that the chemistry of the gas mixture is described by elementary reactions, which can be grouped into N_{rxn} pairs of reversible reactions. We write reaction r ($r = 1, \cdots, N_{\text{rxn}}$) as

$$\sum_{s=1}^{N_{\text{spec}}} \nu_{sr}^+ \mathfrak{M}_s \underset{k_r^-}{\overset{k_r^+}{\rightleftharpoons}} \sum_{s=1}^{N_{\text{spec}}} \nu_{sr}^- \mathfrak{M}_s.$$

(2.5)
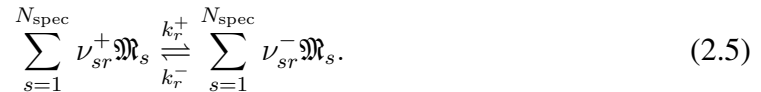
Here, $\mathfrak{M}_s$ represents the chemical symbol of species s. We introduce the superscripts $+$ and $-$ to indicate the forward and reverse reactions, respectively, and denote the number of molecules of species s on the reactant side for the forward and reverse reactions as ν_{sr}^+ and ν_{sr}^-, respectively. We define the stoichiometric coefficients of species s for the reaction r as $\nu_{sr} = \nu_{sr}^- - \nu_{sr}^+$. We also denote the reaction rate constants of the forward and reverse reactions by k_r^+ and k_r^-, respectively.

In the chemical Langevin equation (CLE) [56, 55], the molar concentration production rate for species s, denoted by Ω_s, is expressed as the sum of deterministic and stochastic parts:

$$\Omega_s = \overline{\Omega}_s + \widetilde{\Omega}_s. \tag{2.6}$$

To express $\overline{\Omega}_s$ and $\widetilde{\Omega}_s$, we introduce the mean forward and reverse rates a_r^+ and a_r^- of reaction r. Here we assume that the deterministic reaction rates obey the law of mass action for gas phase reactions [60, 41] which expresses $a_r^{\pm}$ as

$$a_r^{\pm} = k_r^{\pm} \prod_{s=1}^{N_{\text{spec}}} [X_s]^{\nu_{sr}^{\pm}}, \tag{2.7}$$

where $[X_s]$ is the molar concentration of species s. Here, the forward and reverse reaction constants, k_r^+ and k_r^-, are functions of temperature. Standard function forms for these rates and the relationship between these rates that is needed to ensure thermodynamic consistency are discussed in Section 2.3.

The mean production rate $\overline{\Omega}_s$ is then expressed as

$$\overline{\Omega}_s = \sum_{r=1}^{N_{\text{rxn}}} \nu_{sr} \left(a_r^+ - a_r^- \right). \tag{2.8}$$

Assuming that reaction occurrences follow Poisson statistics and applying the Gaussian approximation [55], one can express the stochastic contribution $\widetilde{\Omega}_s$ as

$$\widetilde{\Omega}_s = \frac{1}{\sqrt{N_A}} \sum_{r=1}^{N_{\text{rxn}}} \nu_{sr} \left(\sqrt{a_r^+} \boldsymbol{\mathcal{W}}_r^+ - \sqrt{a_r^-} \boldsymbol{\mathcal{W}}_r^- \right), \tag{2.9}$$

where N_A is the Avogadro constant and $\boldsymbol{\mathcal{W}}_r^{\pm}$ denote Gaussian white noise fields satisfying

$$\langle \boldsymbol{\mathcal{W}}_r^{\alpha}(\mathbf{x}, t) \boldsymbol{\mathcal{W}}_{r'}^{\alpha'}(\mathbf{x}', t') \rangle = \delta_{r,r'} \delta_{\alpha,\alpha'} \delta(\mathbf{x} - \mathbf{x}') \delta(t - t'). \tag{2.10}$$

Note that the factor $1/\sqrt{N_A}$ reflects conversion from the variance of the Poisson distribution in terms of number density to molar concentration.

2.3 Chemistry Formulation

Although reactions are often discussed in terms of forward and reverse rates, these rates are not independent. The rates must be compatible with thermodynamic equilibrium for the system. In Section 2.3.1, we review the basic thermodynamics and chemical kinetics of ideal gas mixtures and show how thermodynamic equilibrium constrains the forward and reverse rates. As part of this discussion, we introduce the symmetric form of reactions that arise from kinetic theory as discussed in Ref. [41]. In Section 2.3.2, we introduce our enthalpy model and derive our main results.

2.3.1 Basic Thermodynamics and Chemical Kinetics of Ideal Gas Mixtures

Chemical Potential and Equilibrium Constant

The thermodynamics of reaction is based on the chemical potential of the reacting species. For an ideal gas mixture, the specific chemical potential of each species s is given by [41]:

$$\mu_s([\boldsymbol{X}], T) = \bar{\mu}_s^\circ(T) + \frac{RT}{M_s} \log \frac{P_s}{P^{st}} = \bar{\mu}_s^\circ(T) + \frac{RT}{M_s} \log \frac{RT[X_s]}{P^{st}} = \mu_s^\circ(T) + \frac{RT}{M_s} \log [X_s],$$
(2.11)

since $P_s = [X_s]RT$. Here, $[\boldsymbol{X}]$ is a vector containing the molar concentrations $[X_s]$ of each species s and P^{st} is a reference pressure. Note that $\bar{\mu}_s^\circ$ and $\mu_s^\circ = \bar{\mu}_s^\circ + \frac{RT}{M_s} \log \frac{RT}{P^{st}}$ are the chemical potentials of the pure substance at the reference pressure and at unit molar concentration, respectively. Since we express reaction rates using molar concentrations $[X_s]$ rather than using partial pressures P_s in this paper, we use μ_s° rather than $\bar{\mu}_s^\circ$. However, one can equivalently use P_s and $\bar{\mu}_s^\circ$ and the corresponding results are summarized in Appendix A.1.

We use a hat notation to denote a dimensionless per-particle quantity. For chemical potential, we define

$$\hat{\mu}_s([\boldsymbol{X}], T) = \frac{M_s}{RT} \mu_s([\boldsymbol{X}], T), \quad \hat{\mu}_s^\circ(T) = \frac{M_s}{RT} \mu_s^\circ(T),$$
(2.12)

and thus have

$$\hat{\mu}_s = \hat{\mu}_s^\circ + \log[X_s].$$
(2.13)

For each reaction r, the condition $\sum_s \nu_{sr}^+ \hat{\mu}_s = \sum_s \nu_{sr}^- \hat{\mu}_s$ must hold at equilibrium. Hence, using Eq. (2.13), at equilibrium we have

$$\exp\left(-\sum_{s=1}^{N_{\text{spec}}} \nu_{sr} \hat{\mu}_s^\circ(T)\right) = \prod_{s=1}^{N_{\text{spec}}} \frac{[X_s]^{\nu_{sr}^-}}{[X_s]^{\nu_{sr}^+}}.$$
(2.14)

We can then define the equilibrium constant as

$$K_r(T) = \exp\left(-\sum_{s=1}^{N_{\text{spec}}} \nu_{sr} \hat{\mu}_s^\circ(T)\right).$$
(2.15)

Law of Mass Action and Rate Constants

We note the $K_r(T)$ is a thermodynamic quantity that depends only on the properties of the system at equilibrium; it does not depend on the reaction rates. In this section, we discuss how $K_r(T)$ constrains the forward and reverse reaction rates. Following Ref. [41], we first consider the mean rate of progress of reaction r denoted by $\tau_r = a_r^+ - a_r^-$. The symmetric form for τ_r is deduced from statistical physics [53]

$$\tau_r = \lambda_r \left\{ \exp\left(\sum_{s=1}^{N_{\text{spec}}} \nu_{sr}^+ \hat{\mu}_s \right) - \exp\left(\sum_{s=1}^{N_{\text{spec}}} \nu_{sr}^- \hat{\mu}_s \right) \right\}, \tag{2.16}$$

where λ_r is the symmetric reaction constant of reaction r. This form of the rate of progress expresses the reaction in terms of a single rate that characterizes how the system relaxes to equilibrium. Using Eq. (2.13), we rewrite this equation as

$$\tau_r = \lambda_r \left\{ \exp\left(\sum_{s=1}^{N_{\text{spec}}} \nu_{sr}^+ \hat{\mu}_s^\circ \right) \prod_{s=1}^{N_{\text{spec}}} [X_s]^{\nu_{sr}^+} - \exp\left(\sum_{s=1}^{N_{\text{spec}}} \nu_{sr}^- \hat{\mu}_s^\circ \right) \prod_{s=1}^{N_{\text{spec}}} [X_s]^{\nu_{sr}^-} \right\}. \tag{2.17}$$

Hence, by defining the rate constants as

$$k_r^\pm(T) = \lambda_r(T) \exp\left(\sum_{s=1}^{N_{\text{spec}}} \nu_{sr}^\pm \hat{\mu}_s^\circ(T) \right), \tag{2.18}$$

we recover the law of mass action

$$\tau_r = k_r^+ \prod_{s=1}^{N_{\text{spec}}} [X_s]^{\nu_{sr}^+} - k_r^- \prod_{s=1}^{N_{\text{spec}}} [X_s]^{\nu_{sr}^-}. \tag{2.19}$$

At chemical equilibrium $\tau_r = 0$. Noting that $k_r^\pm(T)$ share the same factor $\lambda_r(T)$, one can show that for the system to be thermoynamically consistent the forward and reverse rates must be related through the equilibrium constant:

$$K_r(T) = \frac{k_r^+(T)}{k_r^-(T)}. \tag{2.20}$$

Equivalently, one can say that the symmetric constant $\lambda_r(T)$ defines a relation that each pair of rate constants $k_r^\pm(T)$ must satisfy:

$$\lambda_r(T) = k_r^+(T) \exp\left(-\sum_{s=1}^{N_{\text{spec}}} \nu_{sr}^+ \hat{\mu}_s^\circ(T) \right) = k_r^-(T) \exp\left(-\sum_{s=1}^{N_{\text{spec}}} \nu_{sr}^- \hat{\mu}_s^\circ(T) \right). \tag{2.21}$$

The relationship Eq, (2.20) is required for thermodynamic consistency. Consequently, for thermodynamic consistency only one of the forward and reverse rate constants can specified; the other must be obtained via Eq. (2.20) or equivalently Eq. (2.21).

In practice, the functional form of a reaction rate constant is modeled by an empirical expression. The most commonly used form is the modified Arrhenius equation [62, 45]:

$$k(T) = \mathfrak{A} \left(\frac{T}{T^{st}} \right)^{\beta} e^{-\alpha/RT}, \tag{2.22}$$

where $\mathfrak{A}$ is a temperature-independent constant, β is a dimensionless number, α has units of energy per mole, and T^{st} denotes a standard or reference temperature. While some theoretical justifications are available for this form [60], its parameters are usually determined by fitting reaction rate data to this form. Note that this form is used in several standard chemical kinetics databases (e.g. the NIST chemical kinetics database [72] or CHEMKIN [52]) and the parameter values are available.

We note that, even if one of the rate constants, say $k^+(T)$, is modeled by the modified Arrhenius equation, the other rate constant, $k^-(T)$, will not, in general, be described by the same form. This is because $k^-(T)$ cannot be specified independently. Instead it is determined by $K(T)$ and $k^+(T)$ via Eq. (2.20) and its functional form can obey the modified Arrhenius equation *only if* $K(T)$ follows the same form as in Eq. (2.22), i.e.

$$K(T) \sim \left(\frac{T}{T^{st}} \right)^{B} e^{-A/RT} \tag{2.23}$$

for some choice of parameters A and B. In the following section, we consider a simple heat capacity model and show that the resulting $K(T)$ is of the form (2.23) and, as a result, both rate constants can be modeled using the modified Arrhenius equation.

2.3.2 Constant Heat Capacity Model

Assumption

We assume that the specific heat at constant pressure, $c_{p,s}$, is constant for each species s. The specific enthalpy of species s can then be expressed as a linear function of temperature,

$$h_s(T) = h_s^{st} + \int_{T^{st}}^{T} c_{p,s} \, dT' = h_s^{st} + c_{p,s}(T - T^{st}). \tag{2.24}$$

Since the specific internal energy $e_s(T)$ of species s is given as $e_s(T) = h_s(T) - RT/M_s$, it can also be expressed as a linear function of temperature where the specific heat at constant volume, $c_{v,s}$, is also constant so that

$$e_s(T) = e_s^{st} + c_{v,s}(T - T^{st}), \tag{2.25}$$

where

$$e_s^{st} = h_s^{st} - \frac{RT^{st}}{M_s}, \quad c_{v,s} = c_{p,s} - \frac{R}{M_s}. \tag{2.26}$$

One can also derive the pure-component specific entropy of species s,

$$s_s^\circ(T) = s_s^{st} + \int_{T^{st}}^{T} \frac{c_{p,s}}{T'} dT' = s_s^{st} + c_{p,s} \log \frac{T}{T^{st}}. \tag{2.27}$$

We note that the values of $c_{p,s}$, h_s^{st}, and s_s^{st} are readily available in thermochemical databases (e.g. the NIST Chemistry WebBook [70, 1]). Although the specific heat capacity is actually a function of temperature, the constant specific heat capacity model remains valid in a rather wide temperature range in many cases as demonstrated using the NO_2 dimerization example in Section 2.4.

Equilibrium Constant

We show here that for our constant specific heat capacity model the general expression for $K_r(T)$, Eq. (2.15) can be written in the form (2.23), which is identical to the modified Arrhenius equation for rate constants. As discussed above, we can write the chemical potential in terms of enthalpy and entropy,

$$\hat{\mu}_s^\circ(T) = \frac{M_s}{RT}\{h_s(T) - Ts_s^\circ(T)\} + \log \frac{RT}{P^{st}}, \quad \hat{\mu}_s^\circ(T^{st}) = \frac{M_s}{RT^{st}}(h_s^{st} - T^{st}s_s^{st}) + \log \frac{RT^{st}}{P^{st}}. \tag{2.28}$$

Note that logarithm terms appear because we use μ_s° instead of $\overline{\mu}_s^\circ$, see Eq. (2.11). For the simplified model considered here, from Eqs. (2.24) and (2.27), we obtain

$$\hat{\mu}_s^\circ(T) - \hat{\mu}_s^\circ(T^{st}) = \frac{M_s(h_s^{st} - c_{p,s}T^{st})}{R} \left(\frac{1}{T} - \frac{1}{T^{st}} \right) - \left(\frac{M_s}{R}c_{p,s} - 1 \right) \log \frac{T}{T^{st}}. \tag{2.29}$$

By defining

$$\epsilon_s = h_s^{st} - c_{p,s}T^{st} = e_s^{st} - c_{v,s}T^{st}, \tag{2.30}$$

$$\hat{c}_{v,s} = \frac{M_s}{R}c_{v,s} = \frac{M_s}{R}\left(c_{p,s} - \frac{R}{M_s} \right), \tag{2.31}$$

we rewrite Eq. (2.29) as

$$\hat{\mu}_s^\circ(T) - \hat{\mu}_s^\circ(T^{st}) = \frac{M_s\epsilon_s}{R}\left(\frac{1}{T} - \frac{1}{T^{st}} \right) - \hat{c}_{v,s} \log \frac{T}{T^{st}}. \tag{2.32}$$

By substituting Eq. (2.32) into Eq. (2.15), we finally obtain

$$K_r(T) = K_r(T^{st}) \exp\left[-\frac{A_r}{R}\left(\frac{1}{T} - \frac{1}{T^{st}}\right)\right] \left(\frac{T}{T^{st}}\right)^{B_r}, \qquad (2.33)$$

where

$$A_r = \sum_{s=1}^{N_{\text{spec}}} \nu_{sr} M_s \epsilon_s, \quad B_r = \sum_{s=1}^{N_{\text{spec}}} \nu_{sr} \hat{c}_{v,s}. \qquad (2.34)$$

Rate Constants

The form of $K_r(T)$ given by Eq. (2.33) for this simplified model implies that if one of the rate constants can be written in the modified Arrhenius form then that other can be as well. In particular, when we write the forward and reverse rates in modified Arrhenius form as

$$k_r^\pm(T) = k_r^\pm(T^{st}) \exp\left[-\frac{\alpha_r^\pm}{R}\left(\frac{1}{T} - \frac{1}{T^{st}}\right)\right] \left(\frac{T}{T^{st}}\right)^{\beta_r^\pm}, \qquad (2.35)$$

using relation (2.20), the relation between forward and reverse rates can then be simplified to

$$\alpha_r^- = \alpha_r^+ - A_r, \quad \beta_r^- = \beta_r^+ - B_r. \qquad (2.36)$$

2.4   Numerical Example

In this section, we consider an ideal gas mixture with a reversible dimerization reaction,

$$2\mathrm{A} \underset{k^-}{\overset{k^+}{\rightleftharpoons}} \mathrm{A_2}, \tag{2.37}$$

and perform reactive FHD simulations. In Section 2.4.1, we describe how to model the reaction and determine reaction parameters. In Section 2.4.2, we briefly explain our numerical implementation of reactive FHD and the determination of FHD simulation parameters. In Section 2.4.3, we present our simulation study.

2.4.1   Reaction Modeling and Parameters

Our simulation model is inspired by the experimental study of the dimerization of nitrogen dioxide [21]. While the chemical kinetics was measured in the presence of nitrogen gas in the study, we first consider the case where the ideal gas mixture only contains NO_2 and N_2O_4 and then investigate the case where N_2 is also included. For the species index s, A (or NO_2) is set to $s = 1$ and A_2 (or N_2O_4) to $s = 2$. When nitrogen is added, N_2 is set to $s = 3$. Since we only consider one reversible reaction (i.e. $N_{\mathrm{rxn}} = 1$), we drop the reaction index r. By the law of mass action, the forward and reverse rates are expressed as $a^+ = k^+[\mathrm{A}]^2$ and $a^- = k^-[\mathrm{A_2}]$, respectively. The chemical production rates of each species are given as

$$\Omega_1 = -2\left(a^+ + \sqrt{\frac{a^+}{N_A}}\boldsymbol{\mathcal{W}}^+\right) + 2\left(a^- + \sqrt{\frac{a^-}{N_A}}\boldsymbol{\mathcal{W}}^-\right), \tag{2.38}$$

$$\Omega_2 = \left(a^+ + \sqrt{\frac{a^+}{N_A}}\boldsymbol{\mathcal{W}}^+\right) - \left(a^- + \sqrt{\frac{a^-}{N_A}}\boldsymbol{\mathcal{W}}^-\right). \tag{2.39}$$

We use cgs units and, particularly, $\mathrm{mol/cm^3}$ for molar concentration. If one interprets $[X_s]$ as a unitless quantity normalized by unit molar concentration, the units of both k^+ and k^- coincide with those of a^+ and a^-, i.e., $\mathrm{mol/cm^3 \cdot s}$, and thus give a unitless equilibrium constant [81] in Eq. (2.20). If one considers the units of $[X_s]$, the units of k^+ and k^- are $\mathrm{cm^3/mol \cdot s}$ and $\mathrm{s^{-1}}$, respectively.

We assume that each chemical species has constant heat capacity and the reaction rate constants, $k^+(T)$ and $k^-(T)$, follow the modified Arrhenius equation, or equivalently, Eq. (2.35). For the reference temperature $T^{st} = 350\,\mathrm{K}$, the values of the reaction parameters, $k^\pm(T^{st})$, $\alpha^\pm$, and $\beta^\pm$, that we use for our simulation study are given in Table 2.1. We obtain the parameter values of the reverse reaction, $k^-(T^{st})$, α^-, and β^-,

	units	+ (forward reaction)	− (reverse reaction)
$k^{\pm}(T^{st})$	mol/cm^3·s	4.07×10^{11}	6.24×10^7
$\alpha^{\pm}$	erg/mol	-5.34×10^{10}	5.37×10^{11}
$\beta^{\pm}$	unitless	0.645	-1.10

Table 2.1: Reaction parameter values for the dimerization reaction (2.37). These parameters appear in Eq. (2.35)

	units	$s = 1$ (A)	$s = 2$ (A$_2$)
$\hat{\mu}_s^{\circ}(T^{st})$	unitless	-7.27	-2.33
ε_s	erg/g	4.69×10^9	-1.73×10^9
$\hat{c}_{v,s}$	unitless	3.64	9.02

Table 2.2: Thermodynamic parameter values for A and A$_2$. These values are obtained from the thermochemistry data of NO$_2$ and N$_2$O$_4$.

from Ref. [21] via NIST Chemical Kinetics Database [72]. We determine the parameter values of the forward reaction, $k^+(T^{st})$, α^+, and β^+, using the relations (2.20) and (2.36) with the values, $K(T^{st}) = 6.52 \times 10^3$, $A = -5.90 \times 10^{11}$ erg/mol, and $B = 1.74$. We obtain the latter values using the thermochemistry data of NO$_2$ and N$_2$O$_4$ in the NIST Chemistry WebBook [70]. More specifically, for each species, we first compute the values of h_s^{st}, s_s^{st}, and $c_{p,s}$ by evaluating the Shomate equation at T^{st}. We then determine the values of $\hat{\mu}_s^{\circ}(T^{st})$, ϵ_s, and $\hat{c}_{v,s}$ by using Eqs. (2.28), (2.30), (2.31), respectively, and finally $K(T^{st})$ by Eq. (2.15) and A and B by Eq. (2.34). The values of $\hat{\mu}_s^{\circ}(T^{st})$, ϵ_s, and $\hat{c}_{v,s}$ are given in Table 2.2.

Figure 2.1 shows the values of $K(T)$, $k^+(T)$, and $k^-(T)$ computed from our constant heat capacity model. In panel (a), we compare the equilibrium constant values of our model with those directly obtained at each temperature by evaluating the Shomate equation, where the temperature dependence of heat capacity is considered. It is remarkable that our constant heat capacity model reproduces the equilibrium constant $K(T)$ faithfully (within about 0.1% errors) in the temperature range $300\,\mathrm{K} \leq T \leq 400\,\mathrm{K}$. In panel (b), the temperature dependence of $k^+(T)$ and $k^-(T)$ is compared. As temperature increases, $k^+(T)$ decreases gradually, whereas $k^-(T)$ increases significantly. These behaviors can be mainly explained by the signs and magnitudes of the parameters α^+ and α^-. We note that the value of α^+ computed from α^- and A via Eq. (2.36) is negative but rather small.
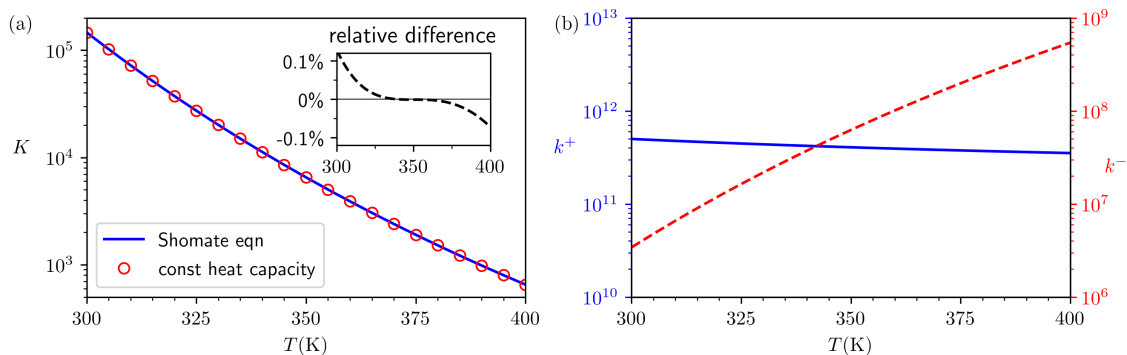
Figure 2.1: In panel (a), the values of the equilibrium constant $K(T)$ obtained from our constant heat capacity model are compared with those computed by the Shomate equation in the temperature range $300\,\mathrm{K} \leq T \leq 400\,\mathrm{K}$. Their relative differences, $(K_{\mathrm{model}} - K_{\mathrm{Shomate}})/K_{\mathrm{Shomate}}$, are shown in the inset. In panel (b), the values of the forward and reverse reaction rate constants, $k^+(T)$ and $k^-(T)$, are plotted versus T. Two y-axes are used; the left one is for $k^+(T)$ (depicted by the blue solid line), whereas the right one is for $k^-(T)$ (by the red dashed line).

2.4.2 Implementation of Reactive FHD

We construct numerical methods to solve reactive FNS equations (2.1) by incorporating chemistry source terms $M_s\Omega_s$ into the existing (nonreactive) FNS solvers [13, 94]. These FNS solvers are based on a method-of-lines approach, where the FNS equations are discretized first in space and the resulting stochastic ordinary differential equations are solved by a stochastic time integration scheme. For spatial discretization, a finite-volume representation is employed in the original FNS solver developed in Ref. [13], whereas a staggered spatial discretization is used in the one developed in Ref. [94]. For temporal integration, both FNS solvers use an explicit, three-stage, low-storage Runge–Kutta (RK3) scheme [2]. Since chemistry source terms are given in the form of Langevin equation, they are readily incorporated into the RK3 scheme. Since species mass densities ρ_s and energy density ρE (and thus temperature T) are located at cell centers in both FNS solvers, the same procedure to include chemistry can be applied to both solvers. We develop reactive FNS solvers based on both original and staggered FNS solvers. For numerical results, we use the staggered one [94]. We refer the reader to Section S1 in the Supplementary Material for a detailed description of the implementation of reactive FHD.

We determine FHD simulation parameters as follows. To choose the equilibrium state, which is needed for the setup of both equilibrium and nonequilibrium simulations,

the equilibrium species mass densities, $\rho_1^{eq} = 1.35 \times 10^{-3}\,\mathrm{g/cm}^3$ and $\rho_2^{eq} = 5.13 \times 10^{-4}\,\mathrm{g/cm}^3$, are determined so that the sum of partial pressures of A and A$_2$ is equal to 1 atm at $T^{eq} = T^{st} = 350\,\mathrm{K}$. The simulation box is a cube of side length $L = 2.56 \times 10^{-4}\,\mathrm{cm}$ with periodic boundary conditions and is discretized into 32^3 cells of side length $\Delta x = 8 \times 10^{-6}\,\mathrm{cm}$. We use time integration step size $\Delta t = 1 \times 10^{-12}\,\mathrm{s}$. Note that thermochemistry parameters, ϵ_s and $\hat{c}_{v,s}$, which are used to determine the reaction parameters, are also used to define the internal energy of each species, $e_s(T) = \epsilon_s + \frac{R}{M_s}\hat{c}_{v,s}T$. For N$_2$, $\epsilon_3 = -3.10 \times 10^9\,\mathrm{erg/g}$ and $\hat{c}_{v,3} = 2.51$. To evaluate transport coefficients [43], each species is assumed to be a hard sphere of diameter d_s: $d_1 = 3.8 \times 10^{-8}\,\mathrm{cm}$, $d_2 = 4.6 \times 10^{-8}\,\mathrm{cm}$, and $d_3 = 3.0 \times 10^{-8}\,\mathrm{cm}$.

2.4.3 Simulation Results

Equilibrium Simulations

To demonstrate that reactive FHD based on our chemistry formulation reproduces the correct statistical distributions at equilibrium, we first perform equilibrium simulations of the NO$_2$/N$_2$O$_4$ mixture. We run each simulation up to 2×10^6 steps with $\Delta t = 1 \times 10^{-12}\,\mathrm{s}$. To estimate an equilibrium average $\langle\cdot\rangle$, we discard the first 2×10^5 steps and compute time average.

To confirm that thermodynamic equilibrium is achieved, one can estimate the cell variance $\langle\delta\phi^2\rangle = \langle(\phi - \phi^{eq})^2\rangle$ of each field quantity ϕ (e.g. ρ_s, T) in each fluid cell and compare this with the value predicted by equilibrium statistical mechanics [13]. For example, temperature fluctuations in a cell of volume ΔV are characterized by

$$\langle\delta T^2\rangle = \frac{k_{\mathrm{B}}T_0^2}{\rho c_{v,mix}\Delta V}, \tag{2.40}$$

where k_{B} is the Boltzmann constant and

$$c_{v,mix} = \frac{1}{\rho}\sum_{s=1}^{N_{\mathrm{spec}}}\rho_s c_{v,s}, \tag{2.41}$$

and our simulation result $\langle\delta T^2\rangle = 2.53\pm0.01\,\mathrm{K}^2$ coincides with the correct value $2.53\,\mathrm{K}^2$. However, to show that fluctuations in different cells are uncorrelated at thermodynamic equilibrium, one should also compute covariances between different cells.

Instead of computing the cell variance and covariances of each field quantity, we investigate the static structure factor [2]. While the structure factor contain essentially the same information as the cell variance and covariances, the former is more convenient to
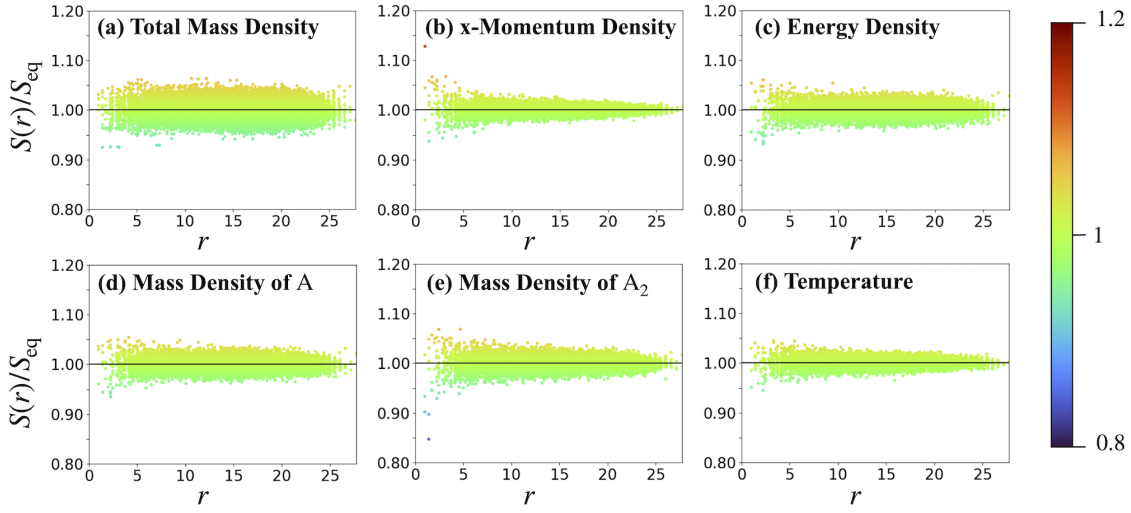
Figure 2.2: Equilibrium structure factor spectra obtained from reactive FHD based on our chemistry formulation. For various field variables, the structure factor values $S(\mathbf{k})$ are normalized by the theoretical values S_{eq} and plotted versus $r = \sqrt{\kappa_x^2 + \kappa_y^2 + \kappa_z^2}$, where $\kappa_i = k_i \left(\frac{2\pi}{L}\right)^{-1}$ is the integer wave index in the i-direction. Panels show the structure factors for (a) ρ, (b) ρu_x, (c) ρE, (d) ρ_1, (e) ρ_2, and (f) T. Each data point is colored based on its normalized value $S(r)/S_{eq}$ (see the color bar). The horizontal black line is drawn at the expected theoretical value for visual clarity.

compute and easier to visualize and analyze. The structure factor for the field variable ϕ is defined as

$$S_\phi(\mathbf{k}) = \Delta V \langle \delta\widehat{\phi}_{\mathbf{k}} \delta\widehat{\phi}_{\mathbf{k}}^* \rangle, \tag{2.42}$$

where V is the volume of the system, $\mathbf{k} = (k_x, k_y, k_z)$ is a vector of wavenumbers, $\delta\widehat{\phi}_{\mathbf{k}}$ is the discrete Fourier transform coefficient of $\delta\phi$ for wavevector $\mathbf{k}$, and $\delta\widehat{\phi}_{\mathbf{k}}^*$ is its complex conjugate. When thermodynamic equilibrium is achieved (i.e. exhibiting the correct cell variance value with zero covariance values), the structure factor of each field becomes a constant function (i.e. $S_\phi(\mathbf{k}) = S_{\phi,eq}$) and its constant value $S_{\phi,eq}$ is related to the correct cell variance via $S_{\phi,eq} = \Delta V \langle \delta\phi^2 \rangle$. For example, the structure factor of the temperature field is given as

$$S_T(\mathbf{k}) = S_{T,eq} = \frac{k_B T_0^2}{\rho c_{v,mix}}. \tag{2.43}$$

For various field variables (ρ, ρu_x, ρE, ρ_1, ρ_2, and T), we show in Figure 2.2 the static structure factors that we obtain from our equilibrium simulation. For each field ϕ,
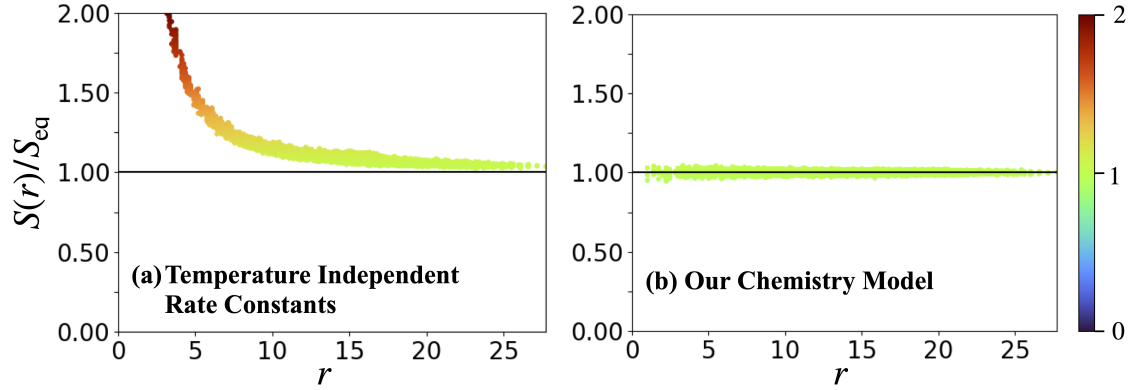
Figure 2.3:   For the temperature field variable, equilibrium structure factor spectra obtained from the temperature-independent rate constant case and our chemistry model are compared. Note that the same data are shown in panel (b) of this figure and panel (f) of Figure 2.2 but different vertical scales are used.

we normalize the values of $S_\phi(\mathbf{k})$ by the correct structure factor value $S_{\phi,eq}$, which can be computed from the correct equilibrium cell variance [13]. To see whether $S_\phi(\mathbf{k})$ does not depend on $\mathbf{k}$, we plot the normalized structure factor values $S_\phi(\mathbf{k})/S_{\phi,eq}$ versus $r = \sqrt{\kappa_x^2 + \kappa_y^2 + \kappa_z^2}$, where $\kappa_i = k_i \left(\frac{2\pi}{L}\right)^{-1}$ is the integer wave index in the i-direction. We observe that all structure factors exhibit flat spectra with the correct values. For the corresponding nonreactive system (i.e. with $k^+ = k^- = 0$), we also observe the same behaviors (see Figure A.1 in Appendix A.4.1). Hence, these simulation results confirm that the incorporation of our stochastic formulation does not disturb the thermodynamic equilibrium state correctly established by nonreactive FHD. In Appendix A.2, by analyzing the chemistry source terms $M_s\Omega_s$ in the FNS equations (2.1) and the structure of the linearized FNS equations for dimerization, we also analytically show that our chemistry formulation gives flat structure factors with the correct values.

   We now turn into the case where a thermodynamically-inconsistent chemistry formulation is used. In an equilibrium simulation, particularly with small temperature fluctuations (note that the magnitude of temperature fluctuations in our dimerization example is $\langle \delta T^2 \rangle^{1/2} = 1.6\,\mathrm{K}$, it is tempting to use temperature-independent rate constants, i.e. $k^\pm(T) = k^\pm(T^{eq})$. However, when these rates are used in FHD simulations, remarkably significant errors appear in the structure factors. Figure 2.3 compares the temperature structure factor of the temperature-independent rate constants case with that of our chemistry model. The structure factor spectrum is not flat and more significant deviations are observed for smaller wave vectors $\mathbf{k}$. This implies that
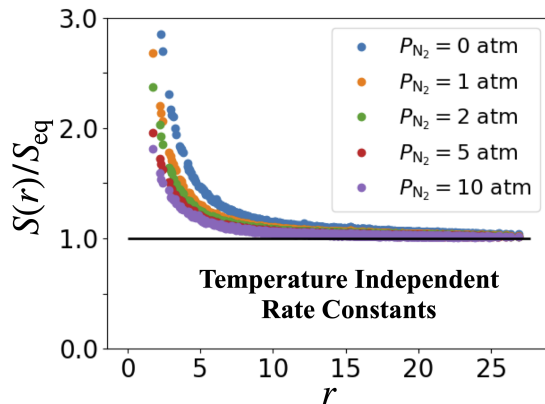
Figure 2.4: For various partial pressure values of N_2, the temperature structure factor spectra obtained from the temperature-independent rate constant case are compared. For visual clarity, rather than plotting all data points, representative values of $S(r)/S_{eq}$ obtained by averaging within each subinterval of r are shown.

temperature fluctuations in different fluid cells are correlated and these incorrect correlations are long-ranged. On the other hand, at short length scales (i.e. large $\mathbf{k}$), fluctuational behaviors are rather similar to those of the nonreactive FHD system. As shown in Figure A.2 in Appendix A.4.2, the structure factor spectra of the other field variables show similar shapes. In Appendix A.2, we provide an explanation on why thermodynamically-inconsistent chemistry causes errors in the small $\mathbf{k}$ region of the structure factor spectra. Roughly speaking, the impact of fluctuations from reaction becomes dominant at long-length scales, whereas that from transport processes (e.g. diffusion) becomes dominant at short-length scales. For a stochastic reaction-diffusion system, a similar behavior was discussed with the concept of the penetration depth [56].

We also perform reactive FHD simulations with N_2 and compare the structure factor spectra of our chemistry model and the temperature-independent case. While maintaining the sum of the equilibrium partial pressures of A and A_2 to be 1 atm, we consider ideal gas mixtures with $P_{N_2} = 1, 2, 5$, and 10 atm. As shown for the temperature structure factor in Figure 2.4, FHD simulations with the temperature-independent rate constants give incorrect spectra with shapes similar to the simulation without N_2 (i.e. more significant errors at smaller $\mathbf{k}$). However, the magnitude of the errors decreases as P_{N_2} increases. This behavior is consistent with the tendency that the impact of incorrect reaction becomes less significant as the mole fraction of the inert gas increases.
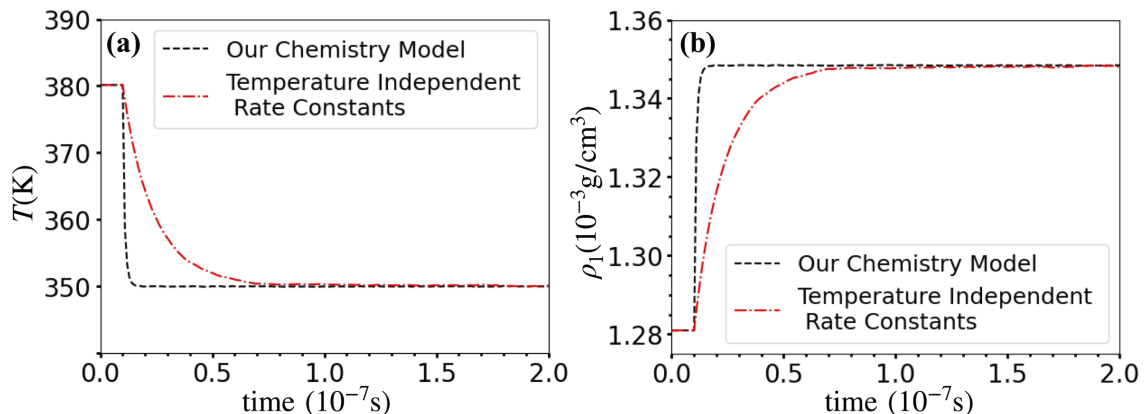
Figure 2.5: The time profiles of spatially averaged temperature (panel (a)) and monomer mass density (panel (b)). The black dashed lines show the results of our chemistry model, whereas the red dotted lines show the temperature-independent rate constant case. Note that chemistry is initially turned off for the first 10^4 time steps, after which reactive FHD is run for additional 1.9×10^5 time steps.

Non-Equilibrium Simulations

We perform non-equilibrium simulations of the NO_2/N_2O_4 mixture with an initial condition perturbed from the equilibrium condition considered above and compare the results from our chemistry model and the temperature-independent rate constant case. We choose the initial condition with $T^{init} = 380\,K$, $\rho_1^{init} = 1.28 \times 10^{-3}\,g/cm^3$, and $\rho_2^{init} = 5.80 \times 10^{-4}\,g/cm^3$ using the relations

$$\rho_1^{init} + \rho_2^{init} = \rho_1^{eq} + \rho_2^{eq}, \tag{2.44}$$

$$\rho_1^{init} e_1(T^{init}) + \rho_2^{init} e_2(T^{init}) = \rho_1^{eq} e_1(T^{eq}) + \rho_2^{eq} e_2(T^{eq}), \tag{2.45}$$

so that a macroscopic well-mixed system with this perturbed initial condition will attain the prescribed equilibrium. For equilibration, we first simulate the system without reaction for 10^4 steps. Then we turn on reaction and simulate the system for 1.9×10^5 steps.

Figure 2.5 shows the time profiles of spatially averaged temperature and monomer mass density. While both our chemistry model and the temperature-independent rate constant case approach the prescribed equilibrium state, their time-transient behaviors are different as expected from their different rate constant values for $T \neq T^{eq}$. We note that the time profiles of the spatially averaged variables can be reproduced by the macroscopic well-mixed system with the corresponding rate constants (i.e. solving ordinary

differential equations). Hence, we confirm that our reactive FHD faithfully reproduces the chemical kinetics of a well-mixed bulk system if there is no mean flow.

2.5   Conclusion

In this work, we discussed an approach to model the behavior of reactive ideal gas mixtures at the mesoscopic scale based on the framework of reactive fluctuating hydrodynamics. We have found that, to properly simulate the dynamics of reactive gases, thermodynamic consistency requires to account for temperature fluctuations in the expression of the rate constants. We verified our implementation by running equilibrium and non-equilibrium simulations for the dimerization of nitrogen dioxide. For the equilibrium simulations, we analyzed the spectrum of fluctuations for several fields of interest, and showed that our formulation produces results consistent with those obtained for the case of non-reactive mixtures, in agreement with theormodynamic theory. Moreover, we showed how even for systems that are initially perturbed from the equilibrium conditions, our reactive FHD formulation accurately reproduces the kinetics of a well-mixed gas mixture.

Chapter 3

Modeling Aggregate Dynamics: Part A, aggregation

3.1 Introduction

The aggregation of small particles into larger clusters occurs in a great variety of contexts. It has been reported in metallic crystal [22, 10] and aerogel formation [112], soot clustering [26], proteins accumulations [102], wastewater treatment [71], and marine aggregates forming in the oceans [7, 24]. In all these cases, smaller particles move, at least in part, in an effectively random manner and may aggregate upon encountering other similar particles. The progressively larger aggregates thus formed often exhibit fractal structures [22, 10, 112, 26, 102, 71, 7, 24].

Arguably the most effective and influential models of aggregation have been the Diffusion-Limited-Aggregation (DLA) and Diffusion-Limited-Cluster-Aggregation (DLCA) models. In the DLA model [104], individual particles undergo stochastic motion until they encounter a cluster that they then stick to, whereas in the DLCA model [59, 73], many particles move simultaneously, form clusters when encountering each other, and continue moving stochastically as clusters. In most cases, the rationale for the stochastic motion of the particles is that they are subject to large numbers of molecular collisions. The effect of these collisions can be modeled as random forces in Langevin dynamics models or directly as random displacements in Brownian dynamics models [19].

The translational diffusivity of individual particles is well known to be inversely proportional to their size, as captured by the Stokes–Einstein relation [32]. As aggregates grow in size, the resistance of the surrounding fluid increases and aggregates are therefore expected to move slower than individual particles. This effect was studied early on in two-

[75, 85] and three-dimensional systems [9] but has been neglected in many DLCA studies. Furthermore, until recently, it was not clear how to determine the hydrodynamic radius of a fractal aggregate in a manner consistent with the Stokes–Einstein relation. A recent study [106] showed that the radius of gyration of an aggregate is an appropriate measure of its size. We study here the effects on aggregation of having size-dependent diffusivities, following and extending the work of Refs. [75], [9].

Early DLA models, where the particles were modeled as spheres and the aggregates formed were fixed, did not include the effects of particle rotation. However, once clusters are allowed to move stochastically, they are expected to rotate as they are subjected to random torques as well. While early two-dimensional studies of DLCA incorporated the effects of rotation [76], these effects were only recently taken into consideration in three-dimensional systems by Jungblut *et al.* [50]. In contradiction to the prior assumption that the effects of rotation on aggregation would be negligible, they demonstrated that the rotation of clusters significantly alter the structure of the resulting aggregates. However, this conclusion was drawn by using constant rotational diffusivity. As indicated by the Stokes–Einstein–Debye relation [30], the rotational diffusivity of an object is inversely proportional to the cube of its size, which, for aggregates, was shown to be well captured by the radius of gyration [106]. Based on these physical observations, we revisit here the effects of rotation. To this end, we present a DLCA model that incorporates rotational effects into Brownian dynamics and accounts, to the best of our knowledge for the first time, for the size-dependence of the rotational diffusivity.

Another factor that can affect the dynamics of particles and clusters during the aggregation process is the density difference between the particles and the surrounding fluid. In many instances, particles such as soot, plankton, or metal atoms are denser than the surrounding medium. The gravitational acceleration will therefore cause particles to settle downward at a speed that increases with their size [103, 48, 95, 106]. While this effect has been well quantified for aggregates already formed, to the best of our knowledge, it has not been incorporated in three-dimensional DLCA models. We therefore also study here the influence of a size-dependent settling velocity on the formation of aggregates.

The quantity typically used to characterize the fractal structures of randomly formed aggregates is their fractal dimension [92]. Models of DLCA (see for instance Ref. [74]) as well as experiments [25, 93] have reported fractal dimensions in the 1.7–1.8 range. However, lower fractal dimensions (1.5–1.6) have also been measured in soot aggregates [26] and a broad range of fractal dimensions (1.28–1.86) have been measured in marine aggregates [54]. In addition, models incorporating rotation [76, 50, 49] have reported fractal dimensions in the 1.5–1.6 range.

The rest of this Chapter is organized as follows. In Section 3.2 we provide details on the formulation of our aggregation model, for spherical particles that undergo translational

and rotational Brownian motion, and are subject to size-dependent diffusivities and settling under gravity. In Section 3.3 we validate our choices of parameters. In Section 3.4 we give the details of our numerical implementation. In Section 3.5 we explain the time range considered in our analysis, and discuss the results obtained in our simulations for the growth rate and fractal dimension of the aggregates. In Section 3.6 we present our Conclusions, and in Section 3.7 we discuss current and future directions for our efforts on modeling aggregate dynamics.
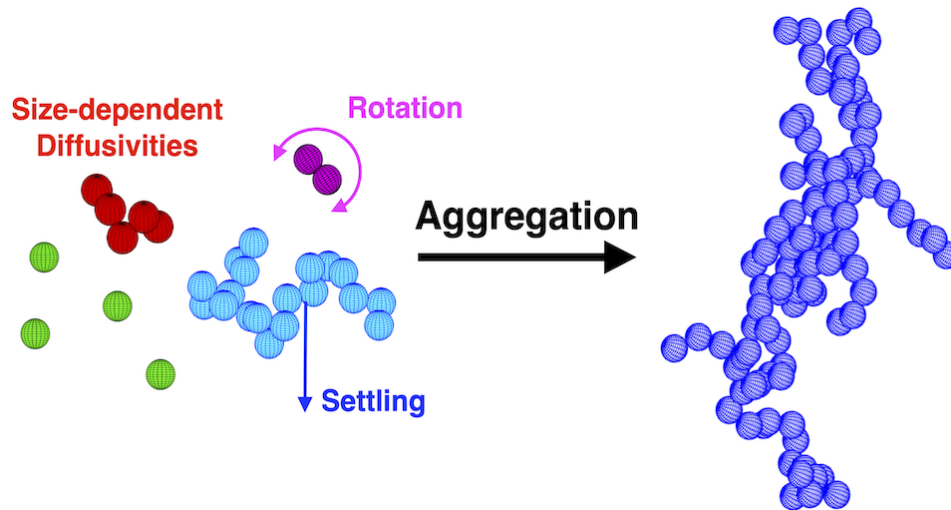
3.2 Method

In our model, aggregates are built from identical spheres. We consider spheres of radius $R'_1 \approx 1\mu\mathrm{m}$ or smaller, so that inertial effects are negligible. Brownian dynamics are applied to aggregates to randomly translate and rotate them [19]. In addition, following the DLCA model [74], if any two spheres overlap (i.e. their centers of mass are within one sphere diameter), the aggregates containing them are made to merge irreversibly and move as a single aggregate thereafter. Hence, as time progresses, spheres merge into aggregates of various sizes and eventually form a single large aggregate. Snapshots taken from a typical simulation of our model are shown in Fig. 3.1 and the structure of the final aggregate obtained is shown in Fig. 3.2.
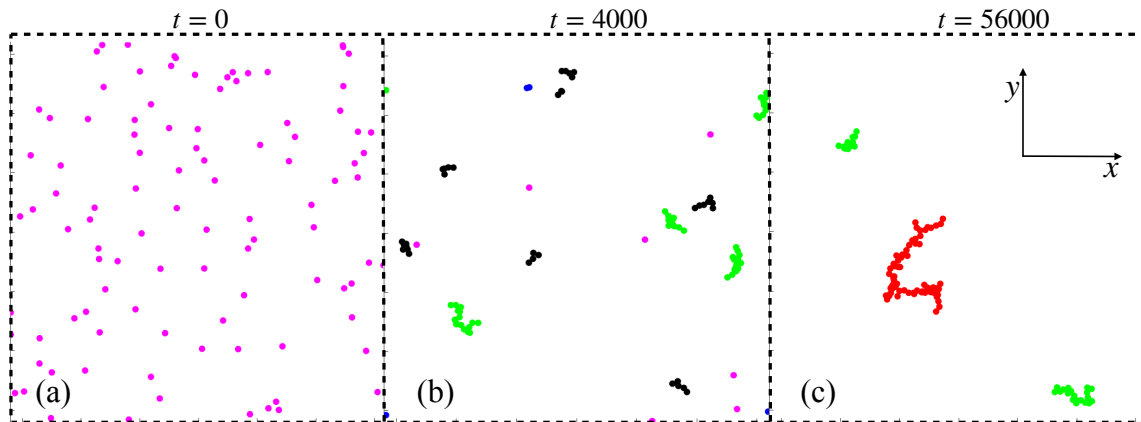
Figure 3.1: Snapshots taken from a typical simulation. Panel (a) displays the initial distribution of $N = 100$ spheres and panels (b) and (c) depict the distributions of aggregates formed at times $t = 4000$ and 56000, respectively. The simulation domain was a cubic box with side length $L = 128$ with periodic boundaries in every direction. For visual clarity, projected images onto the xy-plane are shown. Different colors are used to show the the number of spheres M in an aggregate; magenta for $M = 1$, blue for $2 \leq M < 10$, black for $10 \leq M < 30$, green for $30 \leq M < 60$, and red for $60 \leq M$.
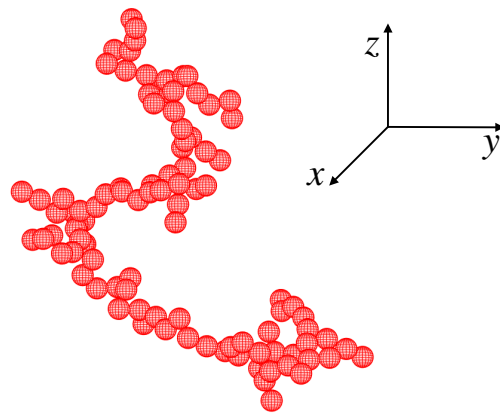
Figure 3.2: Sample aggregate with $M = 100$ spheres. This aggregate was obtained at the end of the simulation shown in Fig. 3.1.

3.2.1   Non-dimensionalization

To write the relevant equations in non-dimensional form, we use the radius, R_1', of a single sphere as our length scale and a diffusive time scale, $\tau' = (R_1')^2/2D_1'$, where D_1' is the translational diffusion coefficient of a single sphere. Here, primes indicate dimensional quantities. We can then define non-dimensional quantities, denoted without a prime, as follows:

$$\vec{x} = \vec{x}'/R_1', \quad t = t'/\tau'. \tag{3.1}$$

3.2.2   Transformation between the center-of-mass and laboratory frames

For an aggregate made of M spheres, we define the position of the mth sphere within the aggregate in the laboratory frame of reference, $\vec{x}_m$, as

$$\vec{x}_m = \vec{x}_c + Q\vec{x}_{m,\text{body}} \quad \text{for } m = 1, \cdots, M. \tag{3.2}$$

Here, $\vec{x}_{m,\text{body}}$ is the position of the mth sphere of the aggregate in a frame of reference that moves with the body of the aggregate. The center of mass of the aggregate is given by $\vec{x}_c = \frac{1}{M}\sum_{m=1}^{M}\vec{x}_m$ and Q is a 3×3 rotation matrix, which we refer to as the orientation matrix of the aggregate.

3.2.3   Translation

To update the position of the center of mass of the aggregate at each time step Δt, we compute

$$\vec{x}_c(t + \Delta t) = \vec{x}_c(t) + \Delta\vec{x}, \tag{3.3}$$

where $\Delta\vec{x} = \sqrt{2D\Delta t}\,\vec{\mathcal{N}}(0,1)$ is a vector denoting a single step taken by the aggregate. Here, D is the translational diffusion coefficient of the aggregate, and $\vec{\mathcal{N}}(0,1)$ denotes a three-dimensional vector with independent random components drawn from the standard normal distribution (i.e. with zero mean and unit variance).

3.2.4   Rotation

To update the orientation of a given aggregate, we evaluate

$$Q(t + \Delta t) = R\, Q(t), \tag{3.4}$$

where R is a rotation matrix. To define R at each time step, we select a three-dimensional vector $\Delta\vec{\theta} = (\Delta\theta_x, \Delta\theta_y, \Delta\theta_z)$ as

$$\Delta\vec{\theta} = \sqrt{2D_\theta \Delta t}\, \vec{\mathcal{N}}_\theta(0, 1), \tag{3.5}$$

where D_θ is the rotational diffusion coefficient of the aggregate and $\vec{\mathcal{N}}_\theta(0, 1)$ is another three-dimensional random vector sampled similarly to $\vec{\mathcal{N}}(0, 1)$. To obtain the rotation matrix R corresponding to $\Delta\vec{\theta}$, we note that the action of R is equivalent to imposing a rigid body rotation with angular velocity $\Delta\vec{\theta}/\Delta t$ to every column $\hat{q}_k$ of the orientation matrix Q over a time step Δt. Therefore, over each time step, we have

$$\frac{d}{dt}\hat{q}_k = \frac{\Delta\vec{\theta}}{\Delta t} \times \hat{q}_k, \tag{3.6}$$

or equivalently in matrix form

$$\frac{dQ}{dt} = \left(\bar{\bar{\bar{\epsilon}}} \cdot \frac{\Delta\vec{\theta}}{\Delta t}\right)Q = \frac{A}{\Delta t}Q, \tag{3.7}$$

where $\bar{\bar{\bar{\epsilon}}}$ is the Levi-Civita permutation tensor and we defined the matrix

$$A = (\bar{\bar{\bar{\epsilon}}} \cdot \Delta\vec{\theta}) = \begin{pmatrix} 0 & \Delta\theta_z & -\Delta\theta_y \\ -\Delta\theta_z & 0 & \Delta\theta_x \\ \Delta\theta_y & -\Delta\theta_x & 0 \end{pmatrix}, \tag{3.8}$$

so that for any vector $\vec{x}$ we have $A\vec{x} = \Delta\vec{\theta} \times \vec{x}$. The exact solution to eq. (3.7) can be expressed by using a matrix exponential as

$$Q(t + \Delta t) = \left(e^{\frac{A}{\Delta t}\cdot\Delta t}\right)Q(t) = e^A Q(t) \tag{3.9}$$

and we therefore have that $R = e^A$. Note that for validation purposes (see section 3.3), we also associate to Q a cumulative angle vector $\vec{\theta}$ defined with components restricted to be between $-\pi$ and π and such that $Q = \exp(\bar{\bar{\bar{\epsilon}}} \cdot \vec{\theta})$.

To efficiently compute the matrix exponential e^A, we first let $\Delta\vec{\theta} = \Delta\psi\,\hat{\Theta}$ for a scalar $\Delta\psi = \|\Delta\vec{\theta}\|$ capturing the rotation angle and a unit vector $\hat{\Theta} = \Delta\vec{\theta}/\|\Delta\vec{\theta}\|$ indicating the rotation axis. Noting that A is anti-symmetric, we then use Rodrigues' formula to compute its exponential [37]

$$R = e^A = I + \frac{\sin(\Delta\psi)}{\Delta\psi}A + \frac{1 - \cos(\Delta\psi)}{\Delta\psi^2}A^2. \tag{3.10}$$

We note that while the same result can be obtained using quaternions [11], we selected the method above as it is easier to relate directly to the physical situation under consideration.

In summary, to implement Brownian rotation, we first generate the random vector $\Delta\vec{\theta}$. We then construct the anti-symmetric matrix A, and compute its exponential, which yields the rotation matrix R used to update the orientation matrix $Q(t)$. Finally, using eqs. (3.3) and (3.4), we can update the position of any sphere as

$$
\begin{aligned}
\vec{x}_m(t + \Delta t) &= \vec{x}_c(t + \Delta t) + Q(t + \Delta t)\,\vec{x}_{m,\text{body}}, \\
&= \vec{x}_c(t) + \Delta\vec{x} + R\,Q(t)\,\vec{x}_{m,\text{body}}.
\end{aligned}
\tag{3.11}
$$

3.2.5   Aggregation

We consider several aggregates undergoing Brownian motion as described by eq. (3.11). We initially confine N single spheres, each of which is assigned a random initial position $\vec{x}_m(0)$ which is uniformly distributed in a cubic domain with periodic boundary conditions applied in all directions. After all spheres (or later aggregates) have moved, we compute the closest distance between all aggregate pairs. If this distance is within one sphere diameter, the spheres or aggregates merge irreversibly, moving as a single aggregate thereafter. Note that while overlapping between spheres can occur, we show in section 3.3 that our choice of time step size confines the overlapping volume to be less than 5% of the total volume of the newly formed aggregate. Once a new aggregate forms, we compute its center of mass $\vec{x}_c$, accounting for periodicity, set its orientation matrix Q to the identity matrix I, and update the relative position of its constituents $\vec{x}_{m,\text{body}}$. Note that $\vec{x}_{m,\text{body}}$ changes only when aggregation occurs. In Fig. 3.3, panels (a) through (c) show snapshots of the typical evolution of a system with $N = 100$ spheres, as aggregates and single spheres undergo Brownian motion and merge. In panel (d), we show a sample aggregate of size $M = 100$.
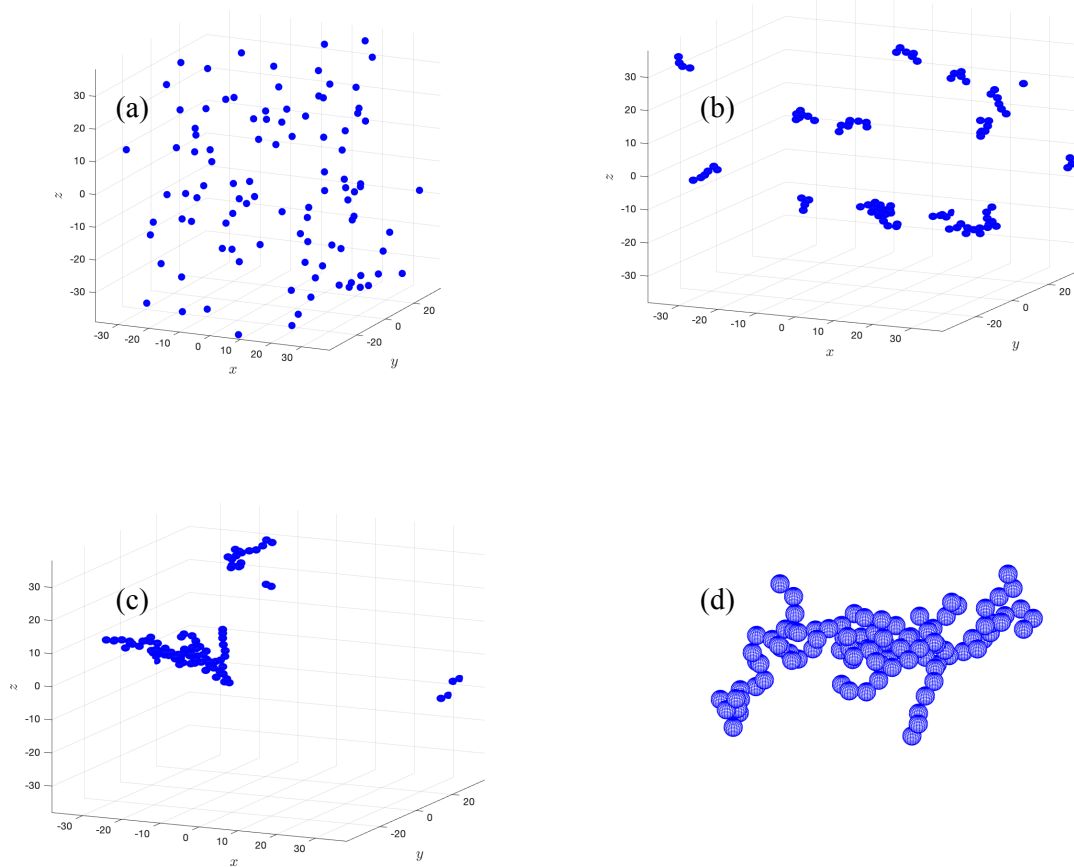
Figure 3.3: Time snapshots of a typical system with $N = 100$ spheres at time $t = 0$ in panel (a), $t = 200$ in panel (b), and $t = 1200$ in panel (c). Eventually, a single aggregate containing $M = 100$ spheres remains, as shown from a closer perspective in panel (d).

3.2.6 Size-dependent diffusivities

To build a more realistic model of aggregation, we allow diffusivities to be size-dependent, as was previously done for translational diffusivity [9]. It has been shown [106] that the best length scale to describe the hydrodynamic resistance of fractal aggregates is the radius of gyration, R_g, and it was found that the translational and rotational friction coefficients of an aggregate are proportional to R_g and R_g^3, respectively. Since the corresponding diffusivities are inversely proportional to the friction coefficients, D and D_θ are proportional to $1/R_g$ and $1/R_g^3$, respectively, which is consistent with the Stokes–Einstein [32] and Stokes–Einstein–Debye equations [30] for the diffusivities of a sphere. For an aggregate made of M spheres of uniform density, the radius of gyration is defined as

$$R_g = \sqrt{\frac{3}{5} + \frac{1}{M} \sum_{m=1}^{M} \|\vec{x}_m - \vec{x}_c\|^2}. \tag{3.12}$$

Here, $\vec{x}_m$ denotes the position of the mth sphere in the aggregate and $\vec{x}_c$ is the center of mass of the aggregate. Note that the definition of R_g for point-mass particles is slightly modified by the addition of $3/5$ to accurately account for the non-zero radius of the spheres, which also recovers the radius of gyration of a single unit sphere with uniform mass distribution: $R_{g1} = \sqrt{3/5}$.

Following Ref. [106], we express the dimensional magnitude of the drag F'_D and torque Q' of aggregates as

$$F'_D = C_T \mu' R'_g U', \quad Q' = C_\theta \mu' (R'_g)^3 \Omega', \tag{3.13}$$

where R'_g is the dimensional radius of gyration, μ' the dynamic viscosity of water, U' the translational speed of the aggregate, Ω' its angular speed, and C_T and C_θ are proportionality factors that depend on the geometry of the object. For single spheres, recalling that $R_{g1} = \sqrt{3/5}$, we have

$$C_T = 6\pi \sqrt{\frac{5}{3}}, \quad C_\theta = 8\pi \left(\frac{5}{3}\right)^{3/2}, \tag{3.14}$$

and for fractal aggregates [106], we use

$$C_T = 18, \quad C_\theta = 25. \tag{3.15}$$

In eq. (3.13), the coefficients in front of U' and Ω' are, respectively, the translational and rotational friction coefficients. By the Einstein relation, we then set the translational and rotational diffusivities to be the ratio of the thermal energy to the appropriate friction coefficient:

$$D' = \frac{k_b T'}{C_T \mu' R'_g}, \quad D'_\theta = \frac{k_b T'}{C_\theta \mu' (R'_g)^3}, \tag{3.16}$$

where k_b is the Boltzmann constant and T' the temperature of the system. We note that eq. (3.16) is consistent with the Stokes–Einstein [32] and Stokes–Einstein–Debye equations [30] for the diffusivities of a sphere.

For a single sphere, the dimensional translational diffusivity is

$$D_1' = \frac{k_b T'}{6\pi\sqrt{5/3}\mu' R_{g1}'} = \frac{k_b T'}{6\pi\mu' R_1'}, \tag{3.17}$$

and, consequently, our corresponding characteristic time scale is

$$\tau' = \frac{(R_1')^2}{2D_1'} = \frac{3\pi(R_1')^3\mu'}{k_b T'}. \tag{3.18}$$

In dimensionless terms, the diffusivities for a single sphere are

$$D = 0.5, \quad D_\theta = D_\theta'\tau' = 0.375, \tag{3.19}$$

and for aggregates

$$D = \frac{D'\tau'}{(R_1')^2} = \frac{0.5}{R_g}, \quad D_\theta = D_\theta'\tau' = \frac{0.375}{R_g^3}. \tag{3.20}$$

Note that in eq. (3.20), we approximated $C_T \approx 18 \approx 6\pi$, and $C_\theta \approx 25 \approx 8\pi$, to simplify the final expression of the diffusivities.

3.2.7 Settling

To incorporate the effects of the gravitational acceleration, g', we consider aggregates with an excess density of $\Delta\rho'$ relative to the surrounding fluid. The corresponding weight is then $F_W' = g'\frac{4}{3}\pi(R_1')^3\Delta\rho' M$, where M is the number of spheres in a given aggregate. Equating the weight to the drag and using eq. (3.13), we find that the settling speed of an aggregate is then

$$U' = \frac{4\pi g'(R_1')^3\Delta\rho' M}{3C_T R_g'\mu'}. \tag{3.21}$$

In non-dimensional form, this settling speed becomes

$$U = \left(\frac{4\pi^2}{C_T}\right)\frac{g'\Delta\rho'(R_1')^4}{k_b T'}\left(\frac{M}{R_g}\right) = \Gamma\frac{M}{R_g}, \tag{3.22}$$

where we defined the quantity

$$\Gamma = \left(\frac{4\pi^2}{C_T}\right)\frac{g'\Delta\rho'(R_1')^4}{k_b T'}, \tag{3.23}$$

which is proportional to the gravitational potential energy of a single sphere made dimensionless using the thermal energy. To compute the value of Γ, we select approximate typical parameter values appropriate to aggregates made of organic matter. To study the impact of various settling speeds, we select three density differences of $\Delta\rho' = 100$, 200, or 400kg/m^3 and use other parameter values of $R_1' = 1\mu\text{m}$, $g' = 10\text{m/s}^2$, and $k_bT' = 4 \times 10^{-21}\text{J}$. We obtain that single spheres have settling speeds $U_1 = 0.525$, 1.05, or 2.10, and that aggregates of more than one sphere have $\Gamma \approx 0.55$, 1.10, or 2.20, and correspondingly have a settling speed of $U = 0.55M/R_g$, $U = 1.10M/R_g$, and $U = 2.20M/R_g$.

3.3 Validation

3.3.1 Dynamics

To validate our approach and implementation, we begin by studying a single sphere undergoing Brownian motion as described by eq. (3.11). We let the sphere move for 10 time steps of size $\Delta t = 0.01$ and record its position and orientation at the final time $t_f = 0.1$.

We first verified that the position of the particle was approximately normally distributed in all three dimensions. We confirmed that the data obtained followed to a good approximation a normal distribution of mean zero and variance $\sigma^2 = 2Dt_f = 0.1$. We also verified that the cumulative angle vector $\vec{\theta}(t_f)$ associated to the final orientation of the sphere $Q(t_f)$ was normally distributed in each coordinate with mean zero and variance $\sigma^2 = 2D_\theta t_f = 0.075$ and again observed close agreement to the theoretical distribution as can be seen for the x-component in Fig. 3.4. Note that our data set was collected at a relatively short time t_f to avoid the impact of periodicity.

3.3.2 Overlap

Our model allows for some overlap between spheres in their last step prior to aggregation. However, we select the time step size to be sufficiently small so that overlap remains minimal. In terms of the distance $\tilde{d}$ between two attached spheres, the overlapping volume is

$$V_{\text{overlap}} = 1 - \frac{3}{4}\tilde{d} + \frac{\tilde{d}^3}{16} \quad \text{for } \tilde{d} \leq 2. \tag{3.24}$$

To quantify the overlap, we run 20 simulations for Case 4 using $\Delta t = 0.01$ with $N = 100$ spheres, until all spheres have merged into a single aggregate. Using eq. (3.24), we compute the distribution of overlapping volumes. From Fig. 3.5, it can readily be seen that
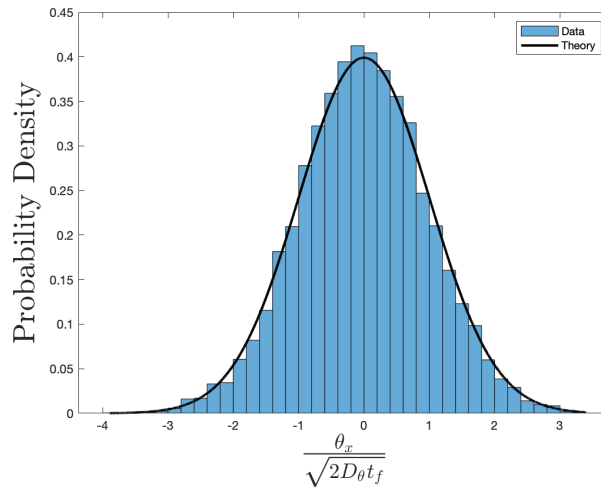
Figure 3.4: Normal distribution of the x-component of the angle vector $\vec{\theta}(t_f)$ associated to the final orientation $Q(t_f)$ of the sphere after 10 time steps. A total of 10^5 samples were collected.

our choice of time step size confines the percentage of overlap amongst any two attached spheres in an aggregate to be less than 5% of their total volume, and usually to be less than 2%. Based on these results, we conclude that our choice of $\Delta t = 0.01$ is a reasonable compromise between overlap minimization and computational efficiency.

3.3.3 Number of nearest neighbors

To help characterize the fractal structure of the aggregates formed in our simulations, we record the number of nearest neighbors of each sphere, defined as the number of spheres that lie within a distance of two from the sphere under consideration. A histogram showing the distribution of the number of nearest neighbors of all spheres within aggregates of size $M \geq 25$ obtained at t_{max} in the case with settling where $U_1 = 1.05$, $\Gamma = 1.10$ and $U = 1.10 M/R_g$ is shown in Figure 3.6. This result is typical for the aggregates we observed; a majority of spheres have two neighbors and roughly equal numbers of spheres have one or three neighbors, while a few spheres have four or five neighbors.
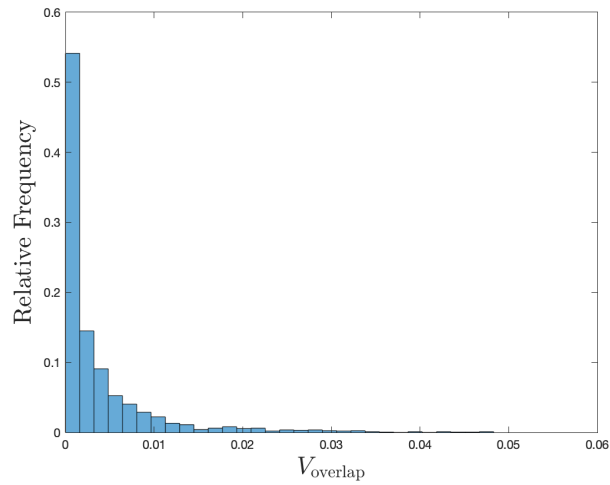
Figure 3.5: Percentage of the overlapping volume amongst attached spheres in aggregates made of $M = 100$ spheres, for simulations run using a time step size of $\Delta t = 0.01$. A total of 20 samples were collected.
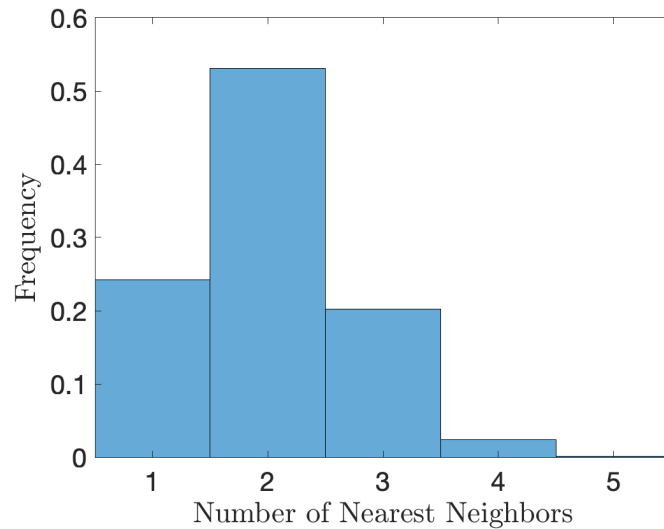
Figure 3.6: Histogram of the number of nearest neighbors for aggregates of size $M \geq 25$ collected at t_{max} in the case with settling where $U_1 = 1.05$, $\Gamma = 1.10$ and $U = 1.10M/R_g$. The vertical axis is normalized as frequency. A total of 20 samples were collected for the volume fraction $\phi = 8 \times 10^{-4}$.

3.4 Numerical Set Up

To characterize the impact of size-dependent diffusivities and rotation on the structure of aggregates and their growth dynamics we study four different cases:

- **Case 1**: $D = 0.5$, $D_\theta = 0$,

- **Case 2**: $D = 0.5$, $D_\theta = 0.375$,

- **Case 3**: $D = 0.5/R_g$, $D_\theta = 0$,

- **Case 4**: $D = 0.5/R_g$, $D_\theta = 0.375/R_g^3$.

In Case 1, we follow the traditional DLCA approach, see for instance Ref. [74], where rotational diffusion is not incorporated and translational diffusivity is kept constant. In Case 2, we incorporate rotation, keeping diffusivities constant, as in Ref. [50]. In Case 3, while rotation is absent, we allow translational diffusivity to be size-dependent, similarly to Ref. [9]. In Case 4, we use more realistic size-dependent diffusivities for both translation and rotation. To the best of our knowledge, the latter model has not been studied to date.

As discussed in Section 3.2.7, when spheres have a greater density than the surrounding fluid, they will, in addition to being subject to Brownian dynamics, settle under the influence of gravity. While this effect was neglected up to this point as it is often small, it is more likely to become influential for larger aggregates. We therefore study **Case 5**, with the same conditions as Case 4 supplemented by a size-dependent aggregate settling speed, U, which is determined by balancing the weight and the drag force as characterized by their radius of gyration [106]. As detailed in Section 3.2.7, we consider three different sets of parameters corresponding to **Cases 5a**, **5b**, and **5c**. In these cases, single spheres are computed to have settling speeds of, respectively, $U_1 = 0.525$, 1.05, and 2.10, while aggregates containing M spheres have $\Gamma = 0.55$, 1.10, and 2.20 for a settling speed of

$$U = 0.55\frac{M}{R_g} \quad \text{(Case 5a)}, \quad U = 1.10\frac{M}{R_g} \quad \text{(Case 5b)}, \quad U = 2.20\frac{M}{R_g} \quad \text{(Case 5c)}.$$

(3.25)

In our simulations, the ratio M/R_g is typically of order one and does not exceed 20. We note that a size-dependent aggregate Péclet number is found to be $Pe = U'R_g'/D' = 2\Gamma R_g M$. This indicates that whenever settling is present its importance grows very quickly with aggregate size, as both M and R_g grow, with a magnitude prescribed by the dimensionless gravitational potential energy of a single sphere Γ. We implement this settling speed as a bias in the vertical direction. Placing the entire system in a frame of reference moving at the settling speed of a single sphere, we select the vertical

displacement Δz of single spheres as before and that of aggregates of more than one sphere as $\Delta z = \sqrt{2D\Delta t}\,\mathcal{N}(0,1) - (U - U_1)\Delta t$.

For all cases considered in our simulations, we initially confine single spheres to a cubic box of side length $L = 128$ with periodic boundary conditions applied in all directions. The time step size is chosen to be $\Delta t = 0.01$ in all cases except when rotational diffusion is constant (Case 2) and large aggregates are present, when Δt was chosen to be as small as $\Delta t = 0.001$. The total number of spheres N is varied between 100 and 400, giving a range of volume fraction $\phi = \frac{4}{3}\pi N/L^3$ between 2×10^{-4} and 10^{-3}. We collect 400 samples for Cases 1–4, and 100 samples for Case 5, for each volume fraction considered in this study.

3.5 Results and Discussion

We monitor over time the radius of gyration R_g of the aggregates as well as the number of spheres M they contain. To characterize the dynamical evolution of the aggregates, we introduce a weighted average of the radius of gyration within a system:

$$\bar{R}_g = \frac{1}{N}\sum_{n=1}^{N} R_g^{(n)}, \tag{3.26}$$

where $R_g^{(n)}$ denotes the radius of gyration of the aggregate containing the nth sphere. We note that $\bar{R}_g$ is computed from each sample as a function of time and that in this average, aggregates with a large number of spheres, M, will have a larger weight, as their radius of gyration is summed M times. We then take the average of $\bar{R}_g$ over all samples formed in the same conditions, which we denote $\langle \bar{R}_g \rangle$.

3.5.1 Growth Rate

We investigate the size growth of aggregates over time using the weighted average of the radius of gyration $\langle \bar{R}_g \rangle$ and compare the results of Cases 1–4 to discuss the effects of size-dependent diffusivities as well as rotation. To minimize computational time and focus on dynamics relevant to very large systems, independent of the domain size considered, we usually interrupt simulations before a single aggregate is formed for all cases except Case 2, where all spheres quickly merge into a single aggregate. For the other six cases, for each volume fraction, we first run 36 samples until all spheres have merged into a single aggregate. Then, we run the next 64 samples until a stopping time, t_s. To determine t_s, we monitor the growth over time of the average radius of gyration $\langle \bar{R}_g \rangle$ of aggregates and compute a reference slope S at the early stages of the simulations. The stopping time
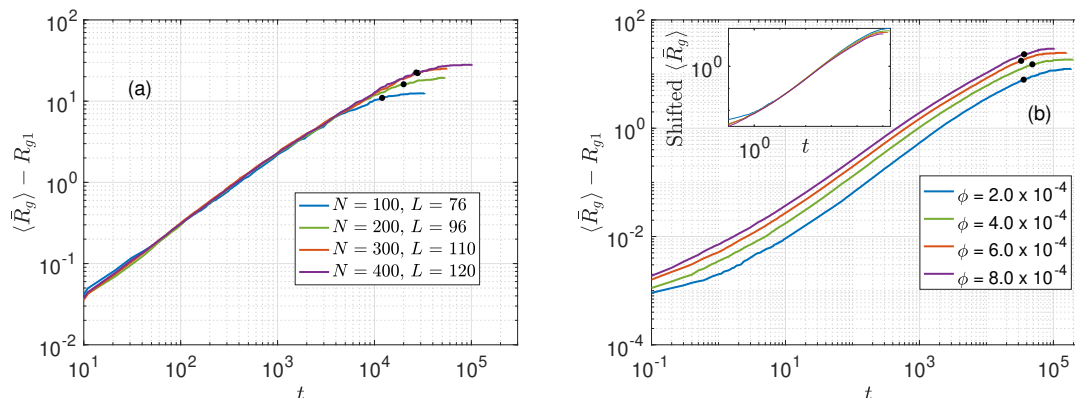
Figure 3.7: Growth over time of the average radius of gyration of aggregates, $\langle \bar{R}_g \rangle$, relative to their initial value, R_{g1}, for Case 4. Panel (a) compares the results obtained for a fixed volume fraction $\phi = 10^{-3}$ and different system sizes (specified by the total number N of spheres and the different domain side lengths L). Panel (b) compares the results of different volume fractions ϕ for a fixed system size with side length $L = 128$. On each curve, t_{max} is shown as a black dot. The inset shows the same curves superimposed by vertical translation.

is then determined as the first time for which the slopes on the intervals $[t_s - 2000, t_s]$ and $[t_s, t_s + 2000]$ are both smaller than $0.05S$. In all cases, from our first 100 samples, we can reliably identify the maximum time, t_{max}, before the domain size begins to have an impact on the system. We identify this time by computing the same slopes discussed above and determine when the slopes on either side of t_{max} are less than half of the reference slope S. We use t_{max} as the largest time considered when fitting the growth rate of aggregates over time. For Cases 1, 3, and 4, we run an additional 300 samples up to t_{max} only (for Case 2 we run these additional samples until a single aggregate is formed). A total of 400 samples were used for Cases 1–4, whereas 100 samples were used for Cases 5a–5c.

Before comparing those results, we first report the effects of finite system-size on the time profile of $\langle \bar{R}_g \rangle$ and also investigate the dependence of the latter quantity on the volume fraction ϕ to justify our choice of simulation parameter values. We note that, contrary to molecular dynamics simulation models whose finite system-size effects have been well understood (see for example Refs. [57], [64]), these effects have not been as systematically investigated for aggregation models.

We show in Fig. 3.7(a) the time profiles of the average radius of gyration of aggregates obtained from 36 samples in Case 4 for different domain sizes, L, and a fixed volume fraction $\phi = 10^{-3}$. For reference, we note that $\langle \bar{R}_g \rangle = R_{g1}$ at $t = 0$ and that if two spheres

	Diffusivities	Exponent $\alpha^\dagger$	Fractal dimension $d^\ddagger$
Case 1	$D = 0.5, D_\theta = 0$	1.02	1.82 ± 0.02
Case 2	$D = 0.5, D_\theta = 0.375$	Not applicable	1.23 ± 0.10
Case 3	$D = 0.5/R_g, D_\theta = 0$	0.66	1.81 ± 0.02
Case 4	$D = 0.5/R_g, D_\theta = 0.375/R_g^3$	0.71	1.69 ± 0.01

Table 3.1: Values of the exponent α and the fractal dimension d for Cases 1–4
† See eq. (3.27) for mathematical definition and Fig. 3.9 for actual estimation;
‡ See eq. (3.28) for mathematical definition and Fig. 3.11 for actual estimation.

meet and form an aggregate the increase in radius of gyration is approximately 0.5. We observe that there is a time period where the growth of $\langle \bar{R}_g \rangle$ is independent of L and is well described by a power law (i.e. a straight line in the log-log plot). At later times, the number of spheres available for aggregation decreases and eventually the growth saturates as too few spheres remain to maintain growth. This behavior happens later for larger domains as they initially contain more spheres.

We also investigate aggregate growth for various volume fractions and for a fixed domain size, $L = 128$, as shown in Fig. 3.7(b). We see that the very early growth for $t \lesssim 1$ is faster for larger volume fractions. This is a reflection of the higher probability that two spheres have initial positions that are separated by a very short distance when the volume fraction is larger. Less time is then required for spheres to first encounter each other. However, the increase in $\langle \bar{R}_g \rangle$ during this time period is rather small ($< 10^{-2}$). More significantly, in a wide time range for $t > 1$, all curves can be superimposed by vertical translation, indicating that the slopes of the curves at a fixed time in the log-log scales appear independent of the volume fraction ϕ. Thus, in a time period where the curves exhibit a nearly constant slope, the growth over the time period can be characterized by an exponent α in the following relation:

$$\langle \bar{R}_g \rangle = C(\phi)t^\alpha + R_{g1}. \tag{3.27}$$

The values of α estimated in Cases 1, 3, and 4 are given in Table 3.1. Overall similar trends are observed for Cases 1–4 except that an acceleration in growth appears before saturation in Case 2, as discussed below. For all cases, corresponding plots to Fig. 3.7(b) are given in Fig. 3.8. The rest of this Section will focus on Cases 1–4, while Cases 5a–5c will be analyzed in further detail in Section 3.5.3.

We now consider the effects of rotational diffusion and size-dependent diffusivity on aggregate growth over the time interval $1 \leq t \leq t_{max}$, where the volume fraction of
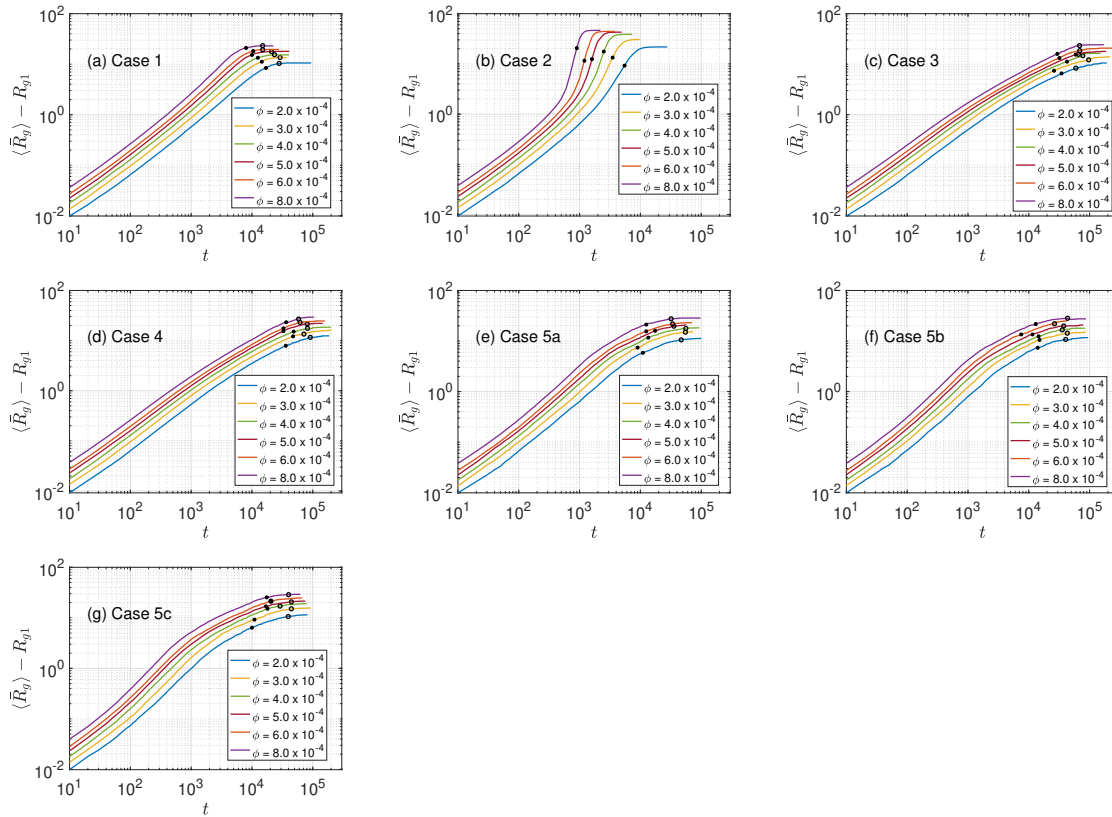
Figure 3.8: We plot over time the growth in the average radius of gyration $\langle \bar{R}_g \rangle$ compared to its initial value R_{g1} for various volume fractions ϕ for all cases considered: (a) Case 1, (b) Case 2, (c) Case 3, (d) Case 4, (e) Case 5a, (f) Case 5b, (g) Case 5c. The black dots indicate the maximum times, t_{max}, at which we collect data for further analysis, and the open circles are the stopping times, t_s, at which we interrupt simulation runs for the second batch of 64 samples.

spheres has only a negligible effect. We show in Fig. 3.9 the temporal evolution of the average size of aggregates for $\phi = 6 \times 10^{-4}$ for Cases 1–4. For $t < 100$, the four curves
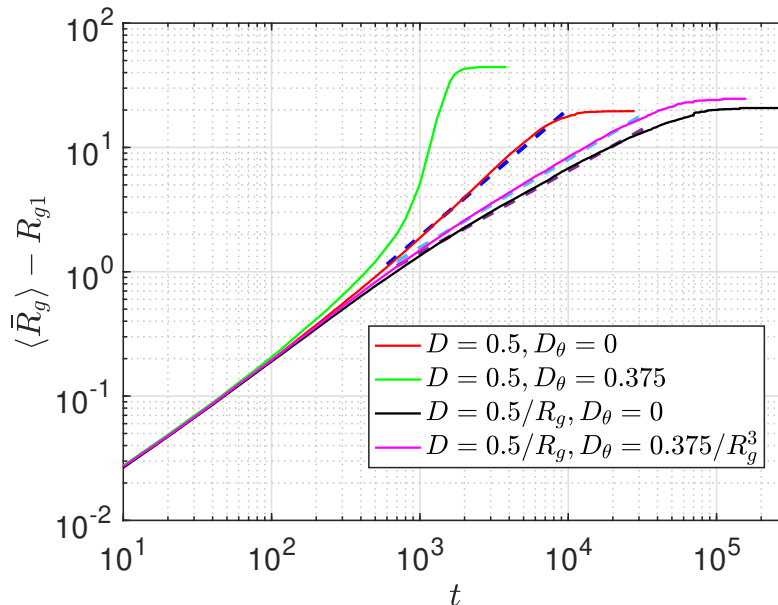
Figure 3.9: Comparison of the growth patterns of average radius of gyration observed in Cases 1–4 for volume fraction $\phi = 6 \times 10^{-4}$. The time profiles of $\langle \bar{R}_g \rangle - R_{g1}$ are shown in the log-log scales as solid lines. For each case except Case 2, linear regressions are also shown as dashed lines, which are obtained over the range starting when $\langle \bar{R}_g \rangle - R_{g1} = 1$ and ending when the size of the systems starts impacting the results at time t_{max}.

overlap, indicating that, at those early times, aggregates exhibit the same growth dynamics. In this regime, the size-dependence of the diffusivities is still weak, as most aggregates are still small, and aggregates move as if their diffusivities were constant. Moreover, rotational diffusion has no effect on single spheres which still constitute most of the aggregates.

As time increases past $t = 100$, differences in the four cases emerge. Unsurprisingly, when the diffusivities are reduced with aggregate size, the growth slows. In the absence of rotation, we see that Case 3 produces a slower growth than Case 1, and similarly Case 4 produces a slower growth than Case 2, which has constant non-zero diffusivities for both translation and rotation. In the latter case (green curve), the growth of the aggregates accelerates as time progresses and becomes faster than a power law. This is due to the larger displacements induced by a fixed rotational diffusivity applied to larger aggregates. In fact, this is the only case where we had to reduce the simulation time step size, using

values as low as $\Delta t = 0.001$ to limit the magnitude of those displacements. Such larger displacements clearly facilitate aggregation, yielding much faster growth. However, it is unlikely that real aggregates can maintain a constant rotational diffusivity as they grow because the resistance of the surrounding fluid to rotation typically grows with the cube of the aggregate size [106].

The second fastest growth, which exhibits a power-law behavior throughout, is observed to be the classic DLCA with fixed translational diffusivity and without rotation (Case 1, red curve). In this case, the growth is nearly linear in time, with a best fit yielding $\langle \bar{R}_g \rangle = C_1(\phi)t^{1.02} + R_{g1}$.

In the two cases where diffusivities are size-dependent, whether rotation is absent (Case 3, black curve) or present (Case 4, magenta curve), the growth is quite similar and appears to follow a power law, but is markedly slower than for DLCA. The presence of rotation again is observed to accelerate growth, as it provides an additional displacement which increases the odds of coming into contact with another aggregate. However, because of the strong dependence of D_θ on R_g, this effect remains small. The growth rate therefore appears to be mostly set by the translational diffusivities. Best fits of the growth rates are found to be $\langle \bar{R}_g \rangle = C_3(\phi)t^{0.66} + R_{g1}$ in the absence of rotation (Case 3) and $\langle \bar{R}_g \rangle = C_4(\phi)t^{0.71} + R_{g1}$ for the most complete model (Case 4) that includes both rotation and size-dependence. Note that while the prefactors in the above relationships depend on ϕ, the powers of t found are consistent across all the volume fractions analyzed.

3.5.2 Fractal Dimension

We now wish to characterize the structure of aggregates observed in the course of aggregation in terms of their fractal dimension, d. To this end, we use the well-known relationship [74, 9] between the number of spheres M in an aggregate and its size, here characterized by the radius of gyration R_g:

$$M \sim (R_g)^d. \tag{3.28}$$

As shown in Fig. 3.10(d) for Case 4, R_g grows approximately as a power of M, with that power being the inverse of the fractal dimension, consistent with eq. (3.28). From Fig. 3.10(a) and (c), it can be seen that Cases 1 and 3 yield a similar relationship, as does Case 2 (Fig. 3.10 (b)), with the caveat that in that case the size of the largest aggregates eventually becomes limited by the domain size.

To find d, we apply eq. (3.28) to data collected at time t_{max}. We focus on aggregates of size $M \geq 25$ to ensure that we are looking at fractal-like objects. Fig. 3.11(b) shows a linear fit of the radius of gyration as a function of M for Cases 1–4 and the fractal dimensions found are listed in Table 3.1. Since the choice of the range of M values for
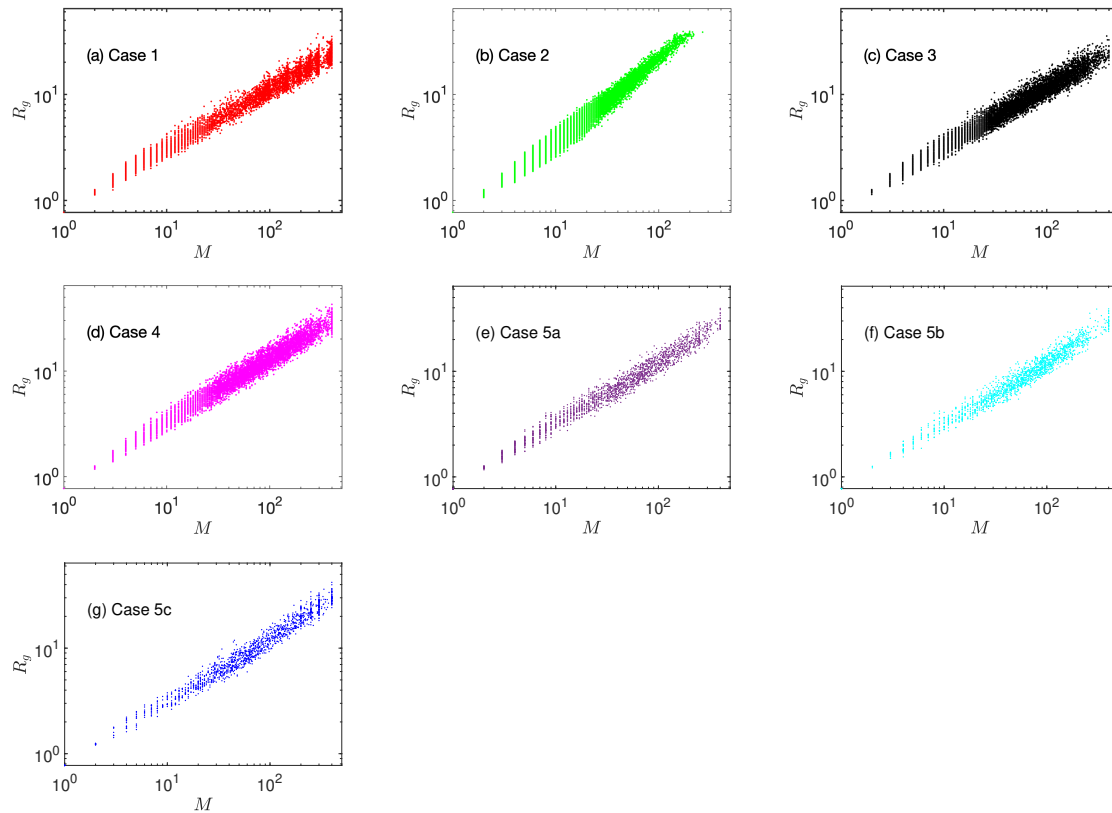
Figure 3.10: Radius of gyration of aggregates, R_g, as a function of the number of sphere they contain, M, for all five cases considered for all volume fractions: (a) Case 1, (b) Case 2, (c) Case 3, (d) Case 4, (e) Case 5a, (f) Case 5b, (g) Case 5c. We used all volume fractions in order to have more data and thus a more reliable estimate of d. Data points were obtained at the time t_{max} (shown in Figure 3.7) from 400 samples for Cases 1–4 and 100 samples for Cases 5a–5c. For Case 2, aggregates of maximum radius [106] greater than or equal to half the side length of the domain were discarded.
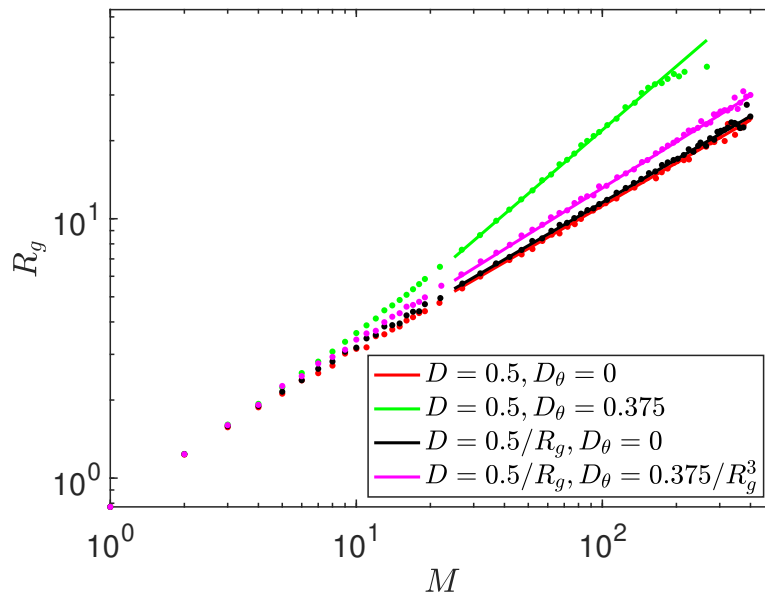
Figure 3.11: Radius of gyration, R_g, of aggregates observed at time t_{max} as a function of the number of spheres in an aggregate, M. We compare the results of Cases 1–4 for all volume fractions, where, for visual clarity, each dot represents the average value of R_g computed over a small interval around a given value of M. Solid lines depict the linear regression results based on data for which $M \geq 25$. For Case 2 (green line), aggregates of maximum radius greater or equal to half the domain size were discarded. A full scatter plot of all Cases considered is shown in Fig. 3.10.

linear regression may affect the resulting estimated value of d, we also compute linear regressions using two different ranges, $M \geq 5$ and $M \geq 50$, and use them to quantify the level of uncertainty in the d values.

Our results for cases without rotation, Cases 1 and 3, are consistent with previous numerical simulations of DLCA, for example, Refs. [9], [74]. However, including rotational diffusion lowers the fractal dimension of the aggregates, most significantly when it is constant. This can be understood by noting that larger aggregates subject to rotation will have their tips experience the largest displacements. This in turn increases the probability that contact with surrounding aggregates will take place at or near the tips, resulting in an object with a more linear structure and therefore a smaller fractal dimension.

The trend of rotational diffusion lowering fractal dimension was previously reported in two-dimensional simulations [76, 85] as well as a recent simulation study with a setup

similar to Case 2 with a constant rotational diffusivity by Jungblut *et al.* [50]. In the latter study, using Langevin dynamics rather than Brownian dynamics and considering systems of volume fraction approximately 10 times greater than ours, a value of fractal dimension of 1.55 ± 0.02 was reported, which is greater than what was found in the present study. We note that this fractal dimension was obtained using data for both smaller aggregates than what was used here and considering aggregates that had reached the percolation limit, where an aggregate can connect with itself via the periodic boundary conditions, both of which tend to increase the computed fractal dimension.

As can be seen comparing Cases 1 and 3, incorporating a size-dependent translational diffusivity is found to cause only a very small reduction of the fractal dimension. The aggregates' structure then appears to remain qualitatively the same and to simply be formed slower when D is size-dependent. Finally, the model with both rotation and size-dependent diffusivities, Case 4, shows a slightly reduced fractal dimension, $d = 1.69$, compared to DLCA. This is most likely due to the inclusion of rotational diffusion, which generates less compact aggregates. However, taking into account the size dependence of the rotational diffusion greatly reduces this effect. The ratio of the diffusivities, $D/D_\theta = \frac{4}{3}R_g^2$, indicates that as the aggregates become larger, translational diffusion becomes dominant, and the resulting aggregates are closer in structure to those formed by DLCA.

3.5.3 Settling

We present in this section results for Cases 5a–5c, where settling is added to Case 4 using a different value of the single sphere gravitational potential energy Γ in each case. From equations (3.25) and (3.28), we see that for $d > 1$, the settling speed of an aggregate increases with its size, potentially affecting the formation dynamics of aggregates and their resulting structure. Note that for Cases 5a–5c, results presented were obtained from 100 samples. Figure 3.12(a) shows that, at early times, incorporating settling in the simulations does not have a significant effect on the growth of aggregates. This is because settling affects dynamics when aggregates have different settling speeds, which only happens when a range of aggregate sizes is present. However, in the time range $40 < t < 100$ the growth of the aggregates is accelerated by the presence of settling, and it can readily be seen that increasing the value of Γ enhances this effect. This acceleration is attributable to larger aggregates settling faster and effectively capturing smaller aggregates located in a vertical column beneath them as they settle. We note that this process takes place over a settling time scale, which here is significantly faster than the diffusive time scale. As a result, finite system-size effects can be felt earlier than in the absence of settling. In other words, in a periodic domain, larger aggregates can quickly collect all smaller aggregates within their
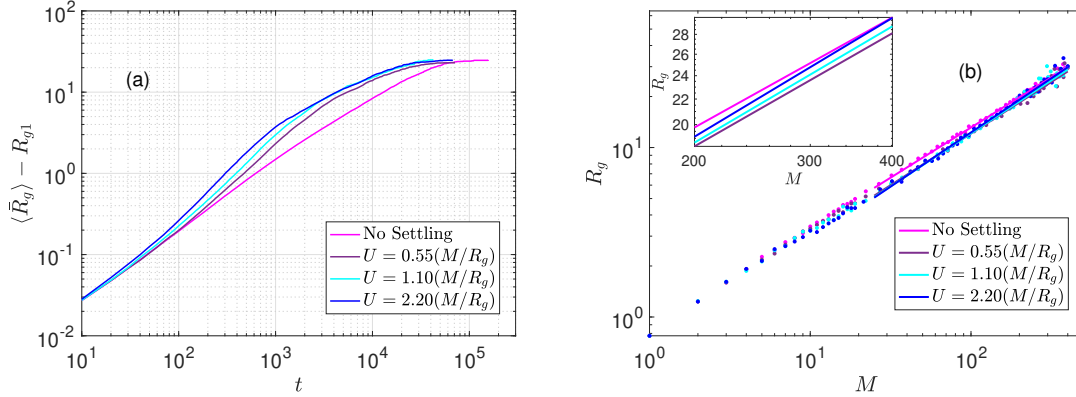
Figure 3.12: Comparison of simulation results without settling (Case 4: magenta) and with size-dependent settling for different values of Γ (Cases 5a: purple, 5b: cyan, and 5c: blue). Size-dependent diffusivities are used in all four cases. Panel (a) shows the time profiles of $\langle \bar{R}_g \rangle - R_{g1}$ in the log-log scales for volume fraction $\phi = 6 \times 10^{-4}$. Panel (b) compares the results of Cases 4, and 5a–5c for all volume fractions, where, for visual clarity, each dot represents the average value of R_g computed over a small interval around a given value of M. Solid lines depict the linear regression results based on data for which $M \geq 25$. The inset shows only the fitted lines for the range $M \geq 200$ to emphasize where they differ.

vertical column and then continue to grow slowly due to horizontal diffusive effects. More care to avoid system-size effects must therefore be taken in simulations of aggregation that include settling.

As can be seen in Figure 3.12(b) and in the values listed in Table 3.2, the fractal dimension of aggregates formed in the presence of settling decreases as the importance of settling, characterized by the gravitational potential energy of a single sphere Γ, increases. For the largest effect of settling we considered, $\Gamma = 2.20$, we find a fractal dimension of $d = 1.56 \pm 0.06$. Moreover, settling breaks the isotropy of the system and distinguishes the vertical direction (denoted with coordinate z) from the horizontal directions (denoted with coordinates x and y). To quantify the effect of this break in symmetry, we measure coordinate specific components of the radius of gyration for Cases 5a–5c. We define the vertical component of the radius of gyration of an aggregate as

$$R_z = \sqrt{\frac{1}{M} \sum_{m=1}^{M} (z_m - z_c)^2}, \tag{3.29}$$

and we define R_x and R_y analogously. Figure 3.13 compares the scatter plot of R_y versus R_x with that of R_z versus R_x at $t = 4000$ from 100 samples for $\phi = 8 \times 10^{-4}$ for Case
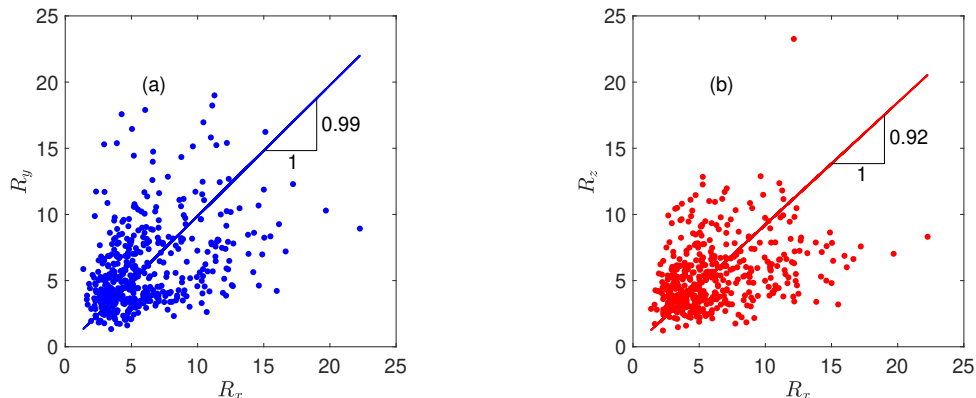
Figure 3.13: Evidence of anisotropy in aggregates formed in the presence of settling, for $\Gamma = 1.10$ (Case 5b). Here, the quantities R_η ($\eta = x, y, z$) represent the contribution of each direction η to the radius of gyration of an aggregate, see equation (3.29). Panel (a) shows a scatter plot of R_y versus R_x and panel (b) shows a scatter plot of R_z versus R_x. The solid lines are best fitted line obtained by averaging the polar angle of the data points and are of slope 0.99 for panel (a) and 0.92 for panel (b). Simulation results were collected at $t = 4000$ for $\phi = 8 \times 10^{-4}$ from 100 samples.

5b, with Cases 5a and 5c exhibiting similar results. The best fits, obtained by averaging the polar angle of the data plotted, are, respectively $R_y = 0.99 R_x$ and $R_z = 0.92 R_x$. This indicates that, as a statistical average, the size of an aggregate in the x and y directions is effectively the same, but that aggregates are on average smaller in the vertical direction.

Even in the absence of settling, individual aggregates do not generally have the same extent in every direction. However, the direction in which they are shortest is then uniformly distributed. In the presence of settling, the shortest direction is statistically preferentially aligned with the vertical. We define the average aggregate aspect ratio γ using the best fit of R_z versus R_x as

$$R_z = \gamma R_x \tag{3.30}$$

and compute it also for Cases 5a and 5c. The results are summarized in Table 3.2. While this aspect ratio remains close to one, it nonetheless reflects the influence of the settling direction on the structure of the aggregates formed and shows that the anisotropy increases with the magnitude of the settling speed. We note that, at earlier times, a smaller difference between the horizontal and vertical directions is observed, presumably because the effects of settling are not yet at their peak. At later times, the vertical extent is also observed to be closer to the horizontal extent. We suspect that finite system-size effects then come

	Single Sphere Grav. P.E. $\Gamma^{\dagger}$	Fractal Dimension $d^{\ddagger}$	Aspect Ratio $\gamma^{\S}$
Case 4	0.0	1.69 ± 0.01	0.99
Case 5a	0.55	1.64 ± 0.08	0.94
Case 5b	1.10	1.60 ± 0.07	0.92
Case 5c	2.20	1.56 ± 0.06	0.90

Table 3.2: Values of the fractal dimension d for Cases 4 and 5a–5c
† See equation (3.22) for relation between Γ and settling speed U and equation (3.23) for its definition;
‡ See equation (3.28) for mathematical definition and Figure 3.12(b) for actual estimation;
§ See equation (3.30) for mathematical definition.

into play in this behavior as settling first depletes available aggregates in vertical columns and further growth effectively occurs sufficiently slowly through horizontal diffusive processes to allow rotational diffusion to re-orient aggregates in an isotropic manner. When the departure from statistical isotropy becomes significant, the assumption of scalar diffusivities is no longer appropriate and diffusivity tensors must be used to describe the Brownian motion of each aggregate [84, 105]. This will be an important consideration to incorporate in future simulations where settling effects are dominant.

3.6   Conclusions

In this work, we studied the impact of size-dependent diffusivities and rotation on the formation mechanisms of aggregates. To this end, we investigated the growth rate and fractal dimension of aggregates by computing the radius of gyration R_g over time. To ensure that the conclusions of our simulation study be independent of the size of the simulation domain, we systematically investigated the finite system-size effects on these quantities. We considered a dilute regime where the solid volume fraction was seen to only be impactful in the very early stages of aggregation.

We found that including size-dependent translational diffusivity, D, into the traditional Diffusion-Limited Cluster Aggregation (DLCA) model has a negligible impact on the fractal dimension, d, of the aggregates formed, which remained near $d = 1.8$. However, we observed that a size-dependent D significantly reduces the growth rate of aggregates, with their average radius of gyration growing like $\langle \bar{R}_g \rangle \sim t^{0.66}$ compared to $\langle \bar{R}_g \rangle \sim t^{1.02}$ in DLCA.

The effects of non-zero rotational diffusion, D_θ, were found to be significant for a constant D_θ. The aggregates then grew much faster and had a significantly reduced fractal dimension, $d = 1.23$. However, this scenario is not appropriate to systems where diffusive effects are due to molecular effects, as the rotational friction coefficient quickly increases with aggregate size. The use of a more realistic, size-dependent, D_θ greatly reduced the impact of rotational diffusion as larger aggregates rotated much more slowly owing to the $D_\theta \sim R_g^{-3}$ scaling. Nonetheless, the fractal dimension of aggregates formed with size-dependent D_θ was reduced compared to DLCA, yielding $d = 1.69$, and their growth rate was accelerated to scale as $\langle \bar{R}_g \rangle \sim t^{0.71}$.

To obtain even more realistic models of aggregation, we also included gravitational effects, causing the aggregates to settle at a rate depending on their size and on the choice of a dimensionless parameter here set to $\Gamma = 0.55, 1.10, 2.20$. We found that settling, much like rotational diffusion, hastened the growth of aggregates and resulted in aggregates of smaller fractal dimension, $d = 1.64, 1.60, 1.56$ for the parameters we considered. We also observed the breaking of isotropy in this case, resulting in aggregates with a slightly shorter vertical extent compared to their horizontal extent. Depending on the size and density of the aggregating spheres, the impact of settling can vary from negligible to dominant and a more systematic study of this effect remains to be completed. Our simulations revealed that finite system-size effects quickly come into play in the presence of settling, so that obtaining results applicable to larger systems likely require significantly greater computational effort.

3.7   Further Modeling Improvements

In order to obtain a more realistic model of aggregation, several other factors will eventually need to be taken into account. For example, particles may only stick to each other with a certain probability rather than automatically as we have assumed [69], leading to a transition from DLCA to Reaction-Limited Cluster Aggregation (RLCA). In addition, aggregates are known to break up, or disaggregate [46, 5], either under the effect of external flows or under the stress due to their own settling, or thermal fluctuations [51]. It has been observed that the growth of aggregates is not strictly irreversible, and that both restructuring and breaking up need to be included to accurate model their growth dynamics. In fact, the effects of the breakup of aggregates is often studied in experimental settings [91], and it is known to be an important factor especially in marine systems. Numerical models of the effects of disaggregation are traditionally based on reversible aggregation approaches [58, 47], where aggregates are allowed to break at random locations after a critical length is reached. Thus, these models do not account for the impact that different conditions, from external forces to background flows, might have in inducing stresses on the aggregates, or how the aggregates structures could affect the way they break. Therefore, to extend the validity and increase the applicability of disaggregation models, a different approach is needed.

In Chapter 4, we will present a novel boundary integral formulation of Stokes Equations to characterize the stresses that aggregates experience as a result of an external force, torque, or background flow. This formulation allows us to study the distribution of stresses in aggregates of different structures and under different conditions, which will be insightful to build more accurate disaggregation models.

Chapter 4

Modeling Aggregate Dynamics: Part B, disaggregation

4.1 Introduction

Near the surface of the ocean, particulates and other microorganisms tend to cluster and form fractal aggregates as they meet. The resulting marine aggregates play an important role in the oceanic carbon cycle [44], and in the transport of microplastics from the ocean surface towards the ocean floor, an issue of major environmental concern [28]. Aggregates initially grow over time and the mechanisms that lead to aggregates formation have been studied extensively [74, 50, 82]. However, it is also well known that aggregates often break up either as they settle under gravity or because of stresses induced by some background flow [91]. Nonetheless, a full characterization of their rupture (disaggregation) is often lacking in numerical models.

Traditionally, disaggregation has been incorporated into models of aggregate dynamics by including a given probability that aggregates might break once they reach a pre-determined critical size [58]. In this so-called *reversible aggregation* approach, aggregates simply break at random locations, regardless of their structure or of the conditions they are exposed to. Recently, there have been renewed efforts to characterize the stresses induced on aggregates immersed in some background flow, particularly in experimental settings [29, 90, 23], and in some simulations [36, 111]. For instance, De La Rosa et al. [29] ran experiments to study the fragmentation of aggregates made of magnetic particles in high-Reynolds-number turbulent von Kármán flows. The authors found that by knowing the intensity of turbulence and the cohesive forces and shapes of the individual particles, one can predict the average size of aggregates exposed to turbulent flows. Zhao et al. [111]

developed one-way coupled numerical simulations to analyze the flocculation dynamics of aggregates exposed to turbulent shear. They investigated the influence of the shear rate on the aggregates' size, and identified what they refer to as *optimal shear rate*, which would "promote preferential concentration of the primary particles without producing sufficiently large stresses to break up the emerging aggregates" [111]. Other studies, such as Zaccone et al. [107] investigated the rupture of compact colloidal aggregates immersed in intermediate and high Reynolds number flows, via a process called *crack propagation*, a mechanism that resembles the fracture mechanics of brittle materials. While this model successfully accounts for the scaling of the size of colloidal aggregates with fractal dimensions close to 3 with the applied hydrodynamic stress, its applicability is typically limited to systems with compact aggregates, as discussed in Ref. [39]. To overcome some of those limitations, Gastaldi et al. [39] proposed a model to characterize the distribution of internal stresses in aggregates based on the method of reflections [42]. In this model, aggregates are made of spheres and translate at a constant velocity, under the effect of a constant force, in an unbounded fluid that is at rest at infinity. Using the method of reflections, the Stokes Equations are then solved to compute the flow velocity and thus extract the drag force acting on each sphere to finally characterize the internal stresses within the aggregates. While this approach gives accurate results for low-density aggregates, it can introduce errors when trying to characterize the stresses in compact aggregates since the method of reflections is valid for widely separated particles, rather than ones in close proximity. These authors provide sample results of computed internal stresses but do not extract trends or distributions of the location of large stresses likely to lead to break up. Thus, while there has been significant progress in recent years, most numerical models have yet to capture the dynamics of disaggregation in a manner than can be incorporated into particulate stochastic models.

Here, we propose a boundary-integral formulation of the Stokes Equations [83] that allows us to characterize the external and internal stresses felt by aggregates of various fractal dimensions subjected to some external force or background flow. We study how the internal stresses distribute in aggregates of different structures, and characterize how different conditions might affect the rupture of aggregates. The rest of this Chapter is organized as follows: in Section 4.2 we give the details of our boundary-integral formulation of Stokes Equations to compute the stresses in aggregates and explain how we characterize the distribution of the aggregates' internal stresses. In Section 4.3 we discuss the results obtained in our simulations considering aggregates subject to a constant force or to a shear flow. We compute the distribution of internal stresses, the scaling of the maximum internal stress, and the relative sizes of aggregates formed after a single break-up event. Finally, Section 4.4 contains our Conclusions. The results of this Chapter are being collected into a manuscript for publication purposes.

4.2 Methods

4.2.1 Types of aggregates considered

To model marine aggregates, we use the well-established numerical framework of diffusion-limited aggregation (DLA) [104]. In order to study aggregates of different fractal dimensions d [73], we use two different DLA-based routines to build aggregates: Individually-Added Aggregation (IAA) with $d \sim 2.3$, and Cluster-to-Cluster Aggregation (CCA) with $d \sim 1.8$. Our aggregates are built from solid cubic particles, closely following Yoo et al. [106], to which we refer the interested reader for a detailed description of both the IAA and CCA aggregation routines used in this work. In Figure 4.1 we display a typical more compact IAA-type aggregate, panel (a), and a typical more wispy CCA-type aggregate, panel (b). Since our focus is on characterizing the stresses felt by marine aggregates under different conditions, we note that the main advantage of building aggregates from solid cubes is that their surface is a simple collection of squares. This fact will be exploited to accurately compute these stresses via a boundary-integral approach [83] , as discussed in detail in Section 4.2.2.

(a) **(b)**

$d \approx 2.3$ $d \approx 1.8$
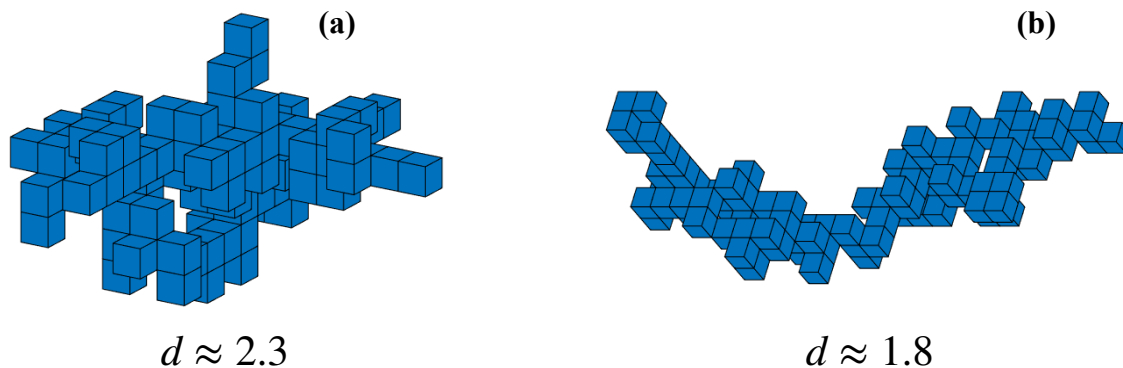
Figure 4.1: Panel (a): typical aggregate formed via IAA-routine; panel (b): typical aggregate formed via CCA-routine. In both cases, aggregates are made of 100 cubes. IAA-type aggregates are generally more compact than CCA-type aggregates, as quantified by their fractal dimension d listed under each aggregate.

4.2.2 Computation of External Stresses

In this paper, we consider aggregates made of cubes with side-length of 2μm, which approximately corresponds to the diameter of individual phytoplankton cells [34, 6]. This

allows us to neglect inertial effects in the description of the flow on the aggregates, and model the relevant dynamics simply using Stokes equations

$$\vec{\nabla} \cdot \vec{u}_{\text{tot}} = 0$$
$$-\vec{\nabla} P_{\text{d}} + \mu \nabla^2 \vec{u}_{\text{tot}} = 0, \tag{4.1}$$

where $\vec{u}_{\text{tot}}$ represents the fluid's velocity and P_{d} is the dynamic pressure, defined at a point $\vec{x}_{\text{p}}$ in the fluid as $P_{\text{d}}(\vec{x}_{\text{p}}) = P(\vec{x}_{\text{p}}) + \rho \vec{g} \cdot \vec{x}_{\text{p}}$, where $\vec{g}$ is the gravitational acceleration. In this work, we assume that both the density, ρ, and the viscosity, μ, are constant. As shown in [83], for some point $\vec{x}_0$ located outside, on, or inside the surface S of any solid object, the solution to Eq. (4.1) can be expressed using a boundary integral formulation, known as the representation formula

$$\vec{u}_{\text{tot}}(\vec{x}_0) = -\frac{1}{8\pi\mu} \int_S \vec{f}(\vec{x}) \cdot \bar{\bar{G}}(\vec{x}, \vec{x}_0) dS(\vec{x}) + \frac{1}{8\pi} \int_S \vec{u}_{\text{tot}}(\vec{x}) \cdot \bar{\bar{T}}(\vec{x}, \vec{x}_0) \cdot \hat{n} dS(\vec{x}), \tag{4.2}$$

where

$$\bar{\bar{G}}(\vec{x}, \vec{x}_0) = \left(\frac{\bar{\bar{I}}}{||\vec{x} - \vec{x}_0||} + \frac{(\vec{x} - \vec{x}_0)(\vec{x} - \vec{x}_0)}{||\vec{x} - \vec{x}_0||^3} \right)$$
$$\bar{\bar{\bar{T}}}(\vec{x}, \vec{x}_0) = -6 \frac{(\vec{x} - \vec{x}_0)(\vec{x} - \vec{x}_0)(\vec{x} - \vec{x}_0)}{||\vec{x} - \vec{x}_0||^5} \tag{4.3}$$

are the so-called single- and double-layer potential, respectively, and the vector $\vec{f}$ is generally referred to as a *density function*, but in this paper it will be referred to as a *vector of stresses*. For ease of notation, in what follows we will assume that the center of mass of the aggregates is at the origin.

We are interested in finding the vector of stresses $\vec{f}$ in the scenarios when aggregates are settling under gravity, or are subjected to some background flow in an infinite ambient. Thus, exploiting the linearity of Stokes equations, we decompose the total flow $\vec{u}_{\textbf{tot}}$ into the sum of an undisturbed component $\vec{u}^\infty$, which would prevail in the absence of the aggregate, and a disturbance component $\vec{u}$, due to the boundary of the aggregate. Next, we require that the total velocity of the fluid on the boundary of any aggregate must satisfy solid-body motion

$$\vec{u}_{\text{tot}}(\vec{x}_{\text{s}}) = \vec{V} + \vec{\Omega} \wedge \vec{x}_{\text{s}}, \tag{4.4}$$

or, equivalently, $\vec{u} = \vec{V} + \vec{\Omega} \wedge \vec{x}_{\text{s}} - \vec{u}^\infty$. Here $\vec{V}$ and $\vec{\Omega}$ are the unknown translational and rotational velocity of the aggregate, respectively. Then, since we are ultimately interested in finding the stresses induced by a flow on the surface of an aggregate, we use the known [83] theoretical result

$$\lim_{\vec{x}_0^{\text{out}} \to \vec{x}_{\text{s}}} \int_S \vec{u} \cdot \bar{\bar{T}}(\vec{x}, \vec{x}_0^{\text{out}}) \cdot \hat{n} dS(\vec{x}) = 4\pi \vec{u}(\vec{x}_{\text{s}}) + \int_S \vec{u}(\vec{x}) \cdot \bar{\bar{T}}(\vec{x}, \vec{x}_{\text{s}}) \cdot \hat{n} dS(\vec{x}), \tag{4.5}$$

where $\vec{x}_0^{\text{out}}$ is a point *outside* of the aggregate, $\vec{x}_{\text{s}}$ is a point that lies *on* the surface of the aggregate, and the last integral should be interpreted in the principal value sense. Applying (4.2) to $\vec{u}$ and then using (4.5) yields

$$\vec{u}(\vec{x}_{\text{s}}) = -\frac{1}{8\pi\mu}\int_S \vec{f}(\vec{x})\cdot\bar{\bar{G}}(\vec{x},\vec{x}_{\text{s}})dS(\vec{x}) + \frac{1}{2}\vec{u}(\vec{x}_{\text{s}}) + \frac{1}{8\pi}\int_S \vec{u}(\vec{x})\cdot\bar{\bar{\bar{T}}}(\vec{x},\vec{x}_{\text{s}})\cdot\hat{n}dS(\vec{x}). \quad (4.6)$$

Finally, plugging in $\vec{u} = \vec{V} + \vec{\Omega} \wedge \vec{x}_{\text{s}} - \vec{u}^{\infty}$ into (4.6), and using the identities [83]

$$\int_S \vec{V}\cdot\bar{\bar{\bar{T}}}(\vec{x},\vec{x}_{\text{s}})\cdot\hat{n}dS(\vec{x}) = -4\pi\vec{V}, \quad \int_S (\vec{\Omega}\wedge\vec{x}_{\text{s}})\cdot\bar{\bar{\bar{T}}}(\vec{x},\vec{x}_{\text{s}})\cdot\hat{n}dS(\vec{x}) = -4\pi\vec{\Omega}\wedge\vec{x}_{\text{s}} \quad (4.7)$$

after simplifications yields

$$\vec{V}+\vec{\Omega}\wedge\vec{x}_{\text{s}}+\frac{1}{8\pi\mu}\int_S \vec{f}(\vec{x})\cdot\bar{\bar{G}}(\vec{x},\vec{x}_{\text{s}})dS(\vec{x}) = \frac{1}{2}\vec{u}^{\infty}(\vec{x}_{\text{s}}) - \frac{1}{8\pi}\int_S \vec{u}^{\infty}(\vec{x})\cdot\bar{\bar{\bar{T}}}(\vec{x},\vec{x}_{\text{s}})\cdot\hat{n}(\vec{x})dS(\vec{x}),$$
$$(4.8)$$

which is a representation formula valid on the surface of solid objects that accounts for the presence of a background flow $\vec{u}^{\infty}$, and where the last integral should still be interpreted in the principal value sense. A full derivation of Eq. (4.8) is provided in Appendix B.1. We note that the identities (4.7) apply to points *on* the surface of a solid object, and that the simplification used in Ref. [106], which claims that the double-layer integral in Eq. (4.2) is identically zero, is applicable only to points outside of a solid object, as shown in [83]. Finally, we also note that Eq. (4.8) is valid for the computation of the external stresses due to the disturbance flow, and further validation is being done as of this writing to include the contribution of the external stresses due to the background flow to obtain the total stresses. However, given the nature of the flow considered in this work, the results are expected to be qualitatively consistent with what will be shown in Section 4.3.

Now, we need to determine the unknown vectors $\vec{f}$, $\vec{V}$ and $\vec{\Omega}$. To this end, we assume that a known external force and torque are imposed on the aggregates, and since all forces must be in equilibrium in inertia-free regimes, we can then relate the total force, $\vec{F}$, and torque, $\vec{Q}$, to the stress vectors as follows

$$\int_S \vec{f}(\vec{x})dS(\vec{x}) = \vec{F},$$
$$\int_S \vec{x} \wedge \vec{f}(\vec{x})dS(\vec{x}) = \vec{Q}. \quad (4.9)$$

Combining Eqs. (4.8) and (4.9) yields the following linear system

$$\vec{V} + \vec{\Omega} \wedge \vec{x}_{\mathrm{s}} + \frac{1}{8\pi\mu} \int_S \vec{f}(\vec{x}) \cdot \bar{\bar{G}}(\vec{x}, \vec{x}_{\mathrm{s}}) dS(\vec{x}) = \frac{1}{2}\vec{u}^\infty(\vec{x}_{\mathrm{s}})$$

$$- \frac{1}{8\pi} \int_S \vec{u}^\infty(\vec{x}) \cdot \bar{\bar{T}}(\vec{x}, \vec{x}_{\mathrm{s}}) \cdot \hat{n}(\vec{x}) dS(\vec{x}),$$

$$\int_S \vec{f}(\vec{x}) dS(\vec{x}) = \vec{F},$$

$$\int_S \vec{x} \wedge \vec{f}(\vec{x}) dS(\vec{x}) = \vec{Q},$$

$$(4.10)$$

Note that, in what follows, we will assume that the stresses $\vec{f}$ are constant over a given square face, and that the point $\vec{x}_{\mathrm{s}}$ is always located at the center of a square face. We provide a simple graphic of how we characterize an aggregate in Figure 4.2. To
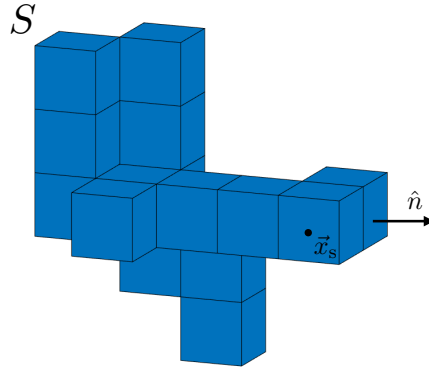
Figure 4.2: Graphic of how we characterize a given fractal aggregate. Here S is the surface of the aggregate, $\vec{x}_{\mathrm{s}}$ is a point on the surface of the object, and the vector $\hat{n}$ is the outward unit normal to the surface.

discretize our system, we introduce the index $k = 1, \ldots, N_{\mathrm{f}}^{(\mathrm{ext})}$, where $N_{\mathrm{f}}^{(\mathrm{ext})}$ is the number of external faces in an aggregate, and we label S_i the i-th external face, where $i = 1, \ldots, N_{\mathrm{f}}^{(\mathrm{ext})}$. Thus, i represents the index that will go over every external square face of the aggregate as we compute the single- and double-layer integrals over the entire boundary $S = \sum_{i=1}^{N_{\mathrm{f}}^{(\mathrm{ext})}} S_i$, evaluating them at the center $\vec{x}_{\mathrm{s},k}$ of every square face, one k

index at a time. Then, for a given k we can write

$$\vec{V} + \vec{\Omega} \wedge \vec{x}_{s,k} + \sum_{i=1}^{N_f^{(ext)}} \vec{f}_i \int_{S_i} \bar{\bar{\bar{G}}}(\vec{x}, \vec{x}_{s,k}) dS_i = \frac{1}{2}\vec{u}^{\infty}(\vec{x}_{s,k})$$

$$- \frac{1}{8\pi} \sum_{i=1}^{N_f^{(ext)}} \int_{S_i} \vec{u}^{\infty}(\vec{x}) \cdot \bar{\bar{\bar{T}}}(\vec{x}, \vec{x}_{s,k}) \cdot \hat{n}_i dS_i,$$

$$\sum_{i=1}^{N_f^{(ext)}} \vec{f}_i \Delta A = \vec{F},$$

$$- \sum_{i=1}^{N_f^{(ext)}} \vec{f}_i \wedge \vec{x}_{s,i} \Delta A = \vec{Q},$$

$$(4.11)$$

where ΔA is the area of the square face S_i and $\bar{\bar{\bar{G}}}(\vec{x}, \vec{x}_{s,k}) = \frac{1}{8\pi\mu}\bar{\bar{G}}(\vec{x}, \vec{x}_{s,k})$. Once fully discretized, we obtain a dense linear system of size $3(N_f^{(ext)} + 2) \times 3(N_f^{(ext)} + 2)$, that, after removing the tilde ($\sim$) notation from the single-layer integrals to ease our notation, can compactly be written as

$$\bar{\bar{A}}\vec{f} = \vec{b}, \qquad (4.12)$$

where

$$\bar{\bar{A}} = \begin{bmatrix} \int_{S_1} \bar{\bar{G}}(\vec{x}, \vec{x}_{s,1}) dS_1 & \int_{S_2} \bar{\bar{G}}(\vec{x}, \vec{x}_{s,1}) dS_2 & \cdots & \int_{S_{N_f^{(ext)}}} \bar{\bar{G}}(\vec{x}, \vec{x}_{s,1}) dS_{N_f^{(ext)}} & \bar{\bar{I}}_1 & [\vec{x}_{s,1}]_{\wedge} \\ \int_{S_1} \bar{\bar{G}}(\vec{x}, \vec{x}_{s,2}) dS_1 & \int_{S_2} \bar{\bar{G}}(\vec{x}, \vec{x}_{s,2}) dS_2 & \cdots & \int_{S_{N_f^{(ext)}}} \bar{\bar{G}}(\vec{x}, \vec{x}_{s,2}) dS_{N_f^{(ext)}} & \bar{\bar{I}}_2 & [\vec{x}_{s,2}]_{\wedge} \\ \vdots & \vdots & \ddots & \vdots & \vdots & \vdots \\ \int_{S_1} \bar{\bar{G}}(\vec{x}, \vec{x}_{s,N_f^{(ext)}}) dS_1 & \int_{S_2} \bar{\bar{G}}(\vec{x}, \vec{x}_{s,N_f^{(ext)}}) dS_2 & \cdots & \int_{S_{N_f^{(ext)}}} \bar{\bar{G}}(\vec{x}, \vec{x}_{s,N_f^{(ext)}}) dS_{N_f^{(ext)}} & \bar{\bar{I}}_{N_f^{(ext)}} & [\vec{x}_{s,N_f^{(ext)}}]_{\wedge} \\ \hline \bar{\bar{I}}_1 \Delta A & \bar{\bar{I}}_2 \Delta A & \cdots & \bar{\bar{I}}_{N_f^{(ext)}} \Delta A & \bar{\bar{0}} & \bar{\bar{0}} \\ \hline [\vec{x}_{s,1}]_{\wedge} & [\vec{x}_{s,2}]_{\wedge} & \cdots & [\vec{x}_{s,N_f^{(ext)}}]_{\wedge} & \bar{\bar{0}} & \bar{\bar{0}} \end{bmatrix},$$

$$(4.13)$$

$$
\vec{f} = \begin{bmatrix} \vec{f}_1 \\ \vec{f}_2 \\ \vdots \\ \vec{f}_{N_{\mathrm{f}}^{(\mathrm{ext})}} \\ \hline \vec{V} \\ \hline \vec{\Omega} \end{bmatrix}, \quad \vec{b} = \begin{bmatrix} DL_1 \\ DL_2 \\ \vdots \\ DL_{N_{\mathrm{f}}^{(\mathrm{ext})}} \\ \hline \vec{F} \\ \hline \vec{Q} \end{bmatrix}, \tag{4.14}
$$

with

$$
DL_k = \frac{1}{2}\vec{u}^\infty(\vec{x}_{\mathrm{s},k}) - \frac{1}{8\pi}\sum_{i=1}^{N_{\mathrm{f}}^{(\mathrm{ext})}} \int_{S_i} \vec{u}^\infty(\vec{x}) \cdot \bar{\bar{T}}(\vec{x}, \vec{x}_{\mathrm{s},k}) \cdot \hat{n}_i dS_i, \quad k = 1, \ldots, N_{\mathrm{f}}^{(\mathrm{ext})}, \tag{4.15}
$$

and we defined the cross-product operator acting on any 3x1 vector $\vec{z}$ as follows

$$
[\vec{z}]_\wedge = \begin{bmatrix} 0 & -z_3 & z_2 \\ z_3 & 0 & -z_1 \\ -z_2 & z_1 & 0 \end{bmatrix}. \tag{4.16}
$$

The single layer integrals are solved analytically as in [106], while the double layer integrals $\int_{S_i} \vec{u}^\infty(\vec{x}) \cdot \bar{\bar{T}}(\vec{x}, \vec{x}_{\mathrm{s},k}) \cdot \hat{n}_i dS_i$ are solved numerically, by first mapping the square S_i to the square $\tilde{S} = \{(\eta_1, \eta_2, \eta_3) : \eta_{1,2} \in [-1, 1], \eta_3 = 0\}$, oriented in the positive vertical direction. To perform the mapping, we construct a linear operator $\bar{\bar{R}}$ such that

$$
\begin{aligned}
\vec{\eta} &= \bar{\bar{R}}(\vec{x} - \vec{x}_{\mathrm{s},i}), \\
\bar{\bar{R}}\hat{n} &= \hat{k}
\end{aligned} \tag{4.17}
$$

where $\vec{x}_{\mathrm{s},i}$ is the center of face S_i, $\vec{\eta} = [\eta_1, \eta_2, 0]^T$ is a 3×1 vector, and $\hat{k} = [0, 0, 1]^T$ is the unit normal vector in the positive vertical direction. After the mapping, the double-layer integral then becomes

$$
\int_{\tilde{S}} \vec{u}^\infty(\bar{\bar{R}}^T\vec{\eta} + \vec{x}_{\mathrm{s},i}) \cdot \bar{\bar{T}}(\bar{\bar{R}}^T\vec{\eta} + \vec{x}_{\mathrm{s},i}, \vec{x}_{\mathrm{s},k}) \cdot \bar{\bar{R}}^T\hat{k}d\tilde{S}, \tag{4.18}
$$

$$\vec{\eta} = \bar{\bar{R}}(\vec{x} - \vec{x}_{\mathrm{s},i})$$
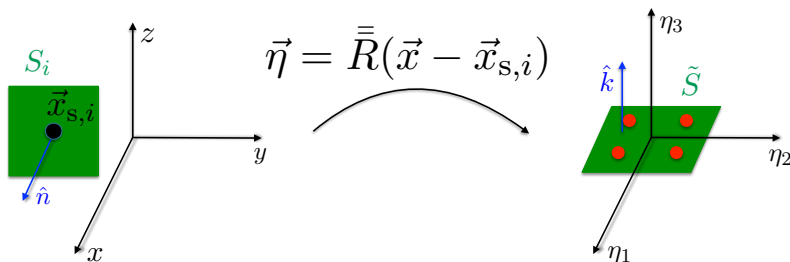
Figure 4.3: Graphic of how we map any face S of a given cube in an aggregate to the square $\tilde{S}$ defined such that each any vector $\vec{\eta} = [\eta_1, \eta_2, \eta_3]^T$ lying on the plane will satisfy $\eta_1 \in [-1, 1]$, $\eta_2 \in [-1, 1]$ and $\eta_3 = 0$, and whose normal vector is $\hat{k} = [0, 0, 1]^T$. The red dots displayed on $\tilde{S}$ represents the evaluation points of our discretization, for the case in which we were to use only two points in each direction for the Midpoint Rule.

as the Jacobian of the transformation is unity. Then, we evaluate (4.18) using the Midpoint Rule, discretizing $\tilde{S}$ using an even number of points in each direction to avoid integrating at the singularity. This allows us to fill the first block of the right-hand side of (4.12). The second and third blocks on the right hand side are filled out by the user-input vectors $\vec{F}$ and $\vec{Q}$, for the external force and torque, respectively. Note that solving this system will yield the translational and rotational velocities of the aggregates, $\vec{V}$ and $\vec{\Omega}$, respectively, and the stresses $\vec{f}$ felt by the aggregates on their *external* faces. We solve (4.12) by simple matrix inversion, and select the least-square solution in those cases in which the system is not full-rank. While matrix inversion is not the most efficient way to solve such a large linear system, it was found that, for the typical aggregate considered, this did not yield any significant additional computational cost.

4.2.3 Computation of Internal Stresses

To compute the internal stresses, we assume that the total force acting on the aggregates is equally distributed across all their constituting cubes. This assumption is motivated by a corresponding assumption that our aggregates are objects of constant density, and that the only forces considered in this work is their weight, or is set to zero. Therefore, the sum of the stresses over all the faces of a cube times their area equals the total force acting on the aggregate, $\vec{F}$, over the number of cubes in the aggregate, M. Moreover, the stresses found on two adjacent faces are assumed to be equal to each other in magnitude but opposite in

direction. Mathematically, those assumptions can be written as follows

$$\vec{F}_m = \vec{F}/M, \quad m = 1, 2, \ldots, M$$

$$\vec{F}_m = \sum_{n=1}^{6} \vec{f}(\vec{x}_n) \Delta A \qquad (4.19)$$

$$\vec{f}(\vec{x}_j)^{(+)} = -\vec{f}(\vec{x}_j)^{(-)}, \quad j = 1, 2, \ldots, N_{\mathrm{f}}^{(\mathrm{int})}.$$

Here $\vec{F}_m$ is the force acting on a single cube, $N_{\mathrm{f}}^{(\mathrm{int})}$ is the total number of internal faces in an aggregate, and $\vec{f}(\vec{x}_j)^{(\pm)}$ are the stresses found on two adjacent faces oriented in opposite directions. Using (4.19), we set up a constrained optimization problem [17]

$$\begin{aligned} &\text{minimize } ||\vec{f}||^2 \\ &\text{subject to } \bar{\bar{C}}\vec{f} = \vec{d}, \end{aligned} \qquad (4.20)$$

where the $N_{\mathrm{f}}^{(\mathrm{int})} \times N_{\mathrm{f}}^{(\mathrm{int})}$ matrix $\bar{\bar{C}}$, and the $N_{\mathrm{f}}^{(\mathrm{int})} \times 1$ vector $\vec{d}$ are built according to the constraints (4.19). To solve (4.20), we first define the Lagrangian function

$$L(\vec{f}; \vec{\lambda}) = (\vec{f})^T \vec{f} + \vec{\lambda}^T (\bar{\bar{C}}\vec{f} - \vec{d}), \qquad (4.21)$$

where $\vec{\lambda}$ is a $N_{\mathrm{f}}^{(\mathrm{int})} \times 1$ vector of Lagrange multipliers, and then compute the related optimality conditions

$$\begin{aligned} \vec{\nabla}_{\vec{f}} L &= 2\vec{f} + \bar{\bar{C}}^T \vec{\lambda} = \vec{0}, \\ \vec{\nabla}_{\vec{\lambda}} L &= \bar{\bar{C}}\vec{f} - \vec{d} = \vec{0}. \end{aligned} \qquad (4.22)$$

Eq. (4.22) can be concisely written as the following block-matrix linear system

$$\begin{bmatrix} 2\bar{\bar{I}} & \bar{\bar{C}}^T \\ \bar{\bar{C}} & \bar{\bar{0}} \end{bmatrix} \begin{bmatrix} \vec{f} \\ \vec{\lambda} \end{bmatrix} = \begin{bmatrix} \vec{0} \\ \vec{d} \end{bmatrix}, \qquad (4.23)$$

whose solution will give us the smallest $\vec{f}$ that satisfies (4.20). Here $\bar{\bar{I}}$ is the $N_{\mathrm{f}}^{(\mathrm{int})} \times N_{\mathrm{f}}^{(\mathrm{int})}$ identity matrix. Once the stress vectors on every internal face have been computed, we extract their magnitude, as a proxy for the likelihood that an aggregate may break. A simple schematics of the process for a typical aggregate made of 100 cubes settling under gravity is shown in Figure 4.4.
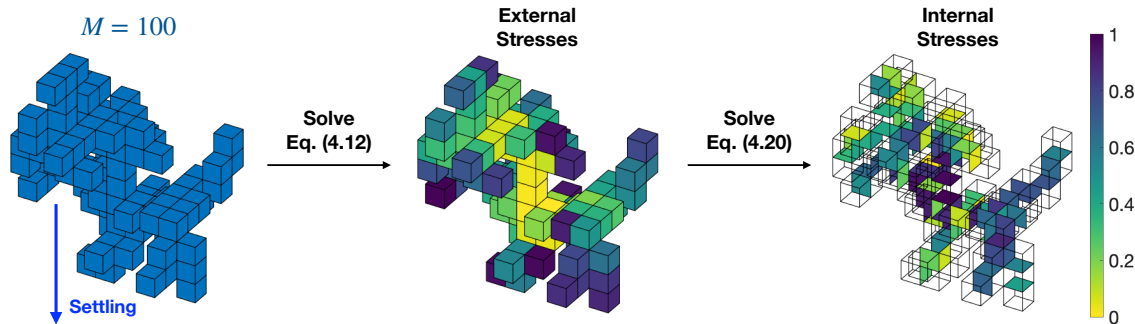
Figure 4.4: Simple schematics of how we characterize the stresses in an aggregate made of $M = 100$ cubes, settling under gravity. The aggregate is depicted in the left-hand column. In the middle column we show the magnitude of all the external stresses found by solving (4.12), normalized by the largest external stress. Finally, the right-hand column shows the magnitude of all the internal stresses found by solving (4.20), normalized by the largest internal stress.

4.2.4 Characterizing the distribution of the internal stresses

To quantify how the internal stresses distribute across the aggregates' structure, we compute the distance, say R, between the internal faces of the aggregates and their center of mass. Then, using the maximum radius

$$R_{\max} = 1 + \max_{m=1,\dots,M}||\vec{x}_m - \vec{x}_{\mathrm{cm}}||, \tag{4.24}$$

we partition the aggregates in three regions, which we will refer to as *shells*, as follows

- Inner Shell: $R < R_{\max}/3$,

- Middle Shell: $R_{\max}/3 \leq R < 2R_{\max}/3$,

- Outer Shell: $R \geq 2R_{\max}/3$.

While we have studied other possible subdivisions of the aggregates, we found that for the typical sizes analyzed in this work, three shells provide a good quantitative picture of the distribution of the internal stresses. We provide a simple graphic of the shells for a typical aggregate made of $M = 100$ cubes in Figure 4.5. To characterize the distribution of internal stresses, we first normalize them by the maximum internal stress and then compute the relative frequency of stresses of a given magnitude range within each shell, using a constant bin size. Then, to model disaggregation we break the aggregate into two newly
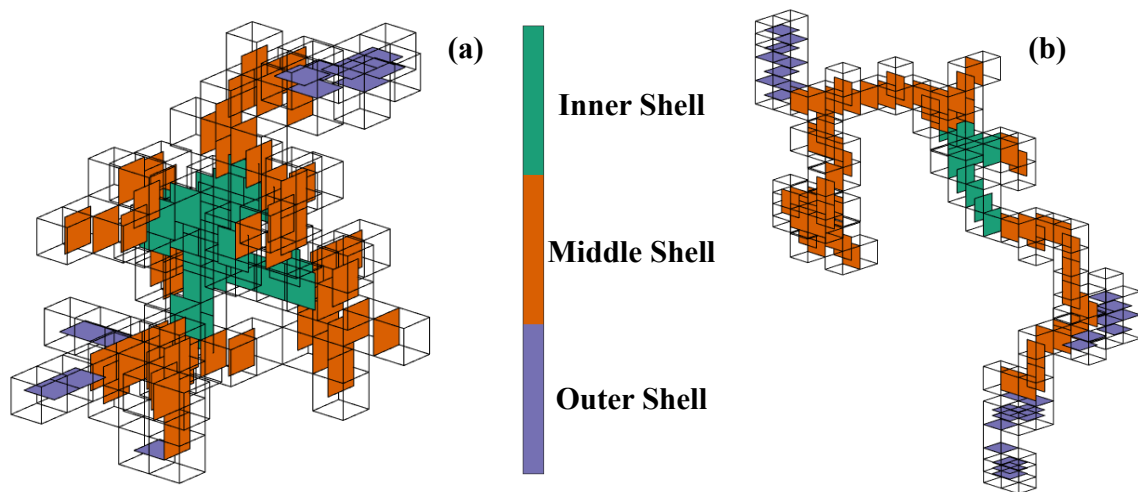
Figure 4.5: Simple schematics of how we characterize the shells in an aggregate made of $M = 100$ cubes, for IAA-type, panel (a), and CCA-type aggregates, panel (b). The internal faces of the aggregates belonging to the Inner Shell are depicted in green. The internal faces belonging to the Middle Shell are depicted in orange. Finally the internal faces belonging to the Outer Shell are depicted in purple. All the external faces are made transparent for visual clarity.

formed aggregates based on the location of the internal face where the maximum internal stress was found, as shown in Figure 4.6 for a typical object made of $M = 100$ cubes settling under gravity. We label the sub-aggregate with the smaller number of cubes with a subscript 1, and the sub-aggregate with the greater number of cubes with a subscript 2. For each sub-aggregate obtained, we compute the maximum radius, as well as the number of their constituting cubes, to quantify the size and mass of the two new aggregates compared to the original.
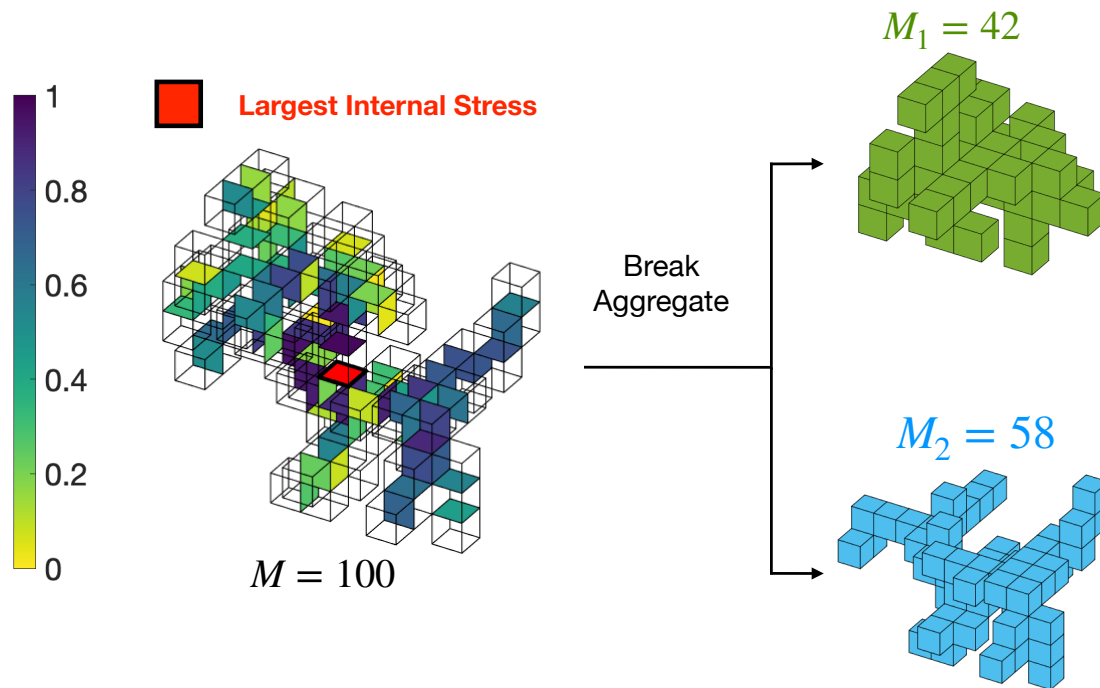
Figure 4.6: Simple schematics of our disaggregation routine. The left-hand column shows the magnitude of all the internal stresses found by solving (4.20) for the settling case for an object made of $M = 100$ cubes. The middle column highlights the location of the face subjected to the largest stress, where we choose to break the aggregate into two. Finally, the right-hand column depicts the two aggregates resulting from the break-up.

4.2.5   Cases Considered

We aim to characterize the internal stresses induced on the aggregates either by the action of some external force, or by some background flow. To this end, we study two

different cases

- **Settling in a fluid at rest (Settling Case)**: $\vec{u}^\infty(\vec{x}) = \vec{0}$, $\vec{F} = (\rho - \rho_{\text{agg}})\vec{g}MV$, $\vec{Q} = \vec{0}$
- **Shear flow in the absence of forces (Shear Case)**: $\vec{u}^\infty(\vec{x}) = \gamma_t y[1, 0, 0]^T$, $\vec{F} = \vec{0}$, $\vec{Q} = \vec{0}$.

In the Settling Case, we impose an external force $\vec{F}$ proportional to the number of cubes constituting a given aggregate, M, while we set both the background flow $\vec{u}^\infty(\vec{x})$ and the external torque $\vec{Q}$ to zero. Here ρ is the density of the fluid, ρ_{agg} is the density of the aggregate, $\vec{g}$ is the acceleration due to gravity, and V is the volume of a single cube of side-length two after non-dimensionalization. In the Shear Case, we impose a canonical laminar shear flow in the horizontal direction, and proportional to the spatial coordinate y, and with some shear rate γ_t [91]. For this case, we set both the external force $\vec{F}$ and torque $\vec{Q}$ to zero. Note that because the system is linear, all computed stresses are proportional to either the imposed force, or the shear rate. For both cases, we compute the internal stresses for aggregates made of a range of M cubes varying from 25 to 200, collecting 400 samples per M. To analyze the distribution of the internal stresses relative to the size and structure of the aggregates, we sort the internal stresses in the shells discussed in Section 4.2.4, averaging over all the samples collected. We compare the results for the two cases considered for IAA- and CCA-type aggregates to characterize the impact that the structure of the aggregates have on the distribution of the internal stresses, and understand how different external conditions might affect the rupture of aggregates.

4.3 Results and Discussion

4.3.1 Settling Case

We begin by studying the Settling Case, corresponding to an aggregate denser than the ambient, settling under gravity in a fluid at rest. In Figure 4.7, we show the distribution of nondimensionalized internal stresses in the three shells discussed in Section 4.2.4, for 400 samples of a single aggregate made of $M = 200$ cubes. Here we use the weight of each aggregate divided by the area of the face of a single cube as a reference stress. In panels 4.7(a) and (b), we display the distribution of the total range of internal stresses computed for IAA-type and CCA-type aggregates, respectively. It can be seen that for all shells and for both cases, the stress probability density function is greatest for small stresses and decays in a manner consistent with a power-law for both IAA and CCA. Furthermore, we find that approximately 98% of the stresses have a magnitude smaller than half the maximum stress observed, leaving only rare instances of high stress. We focus on the distribution tails in panels 4.7(c) and (d) by plotting on a logarithmic scale
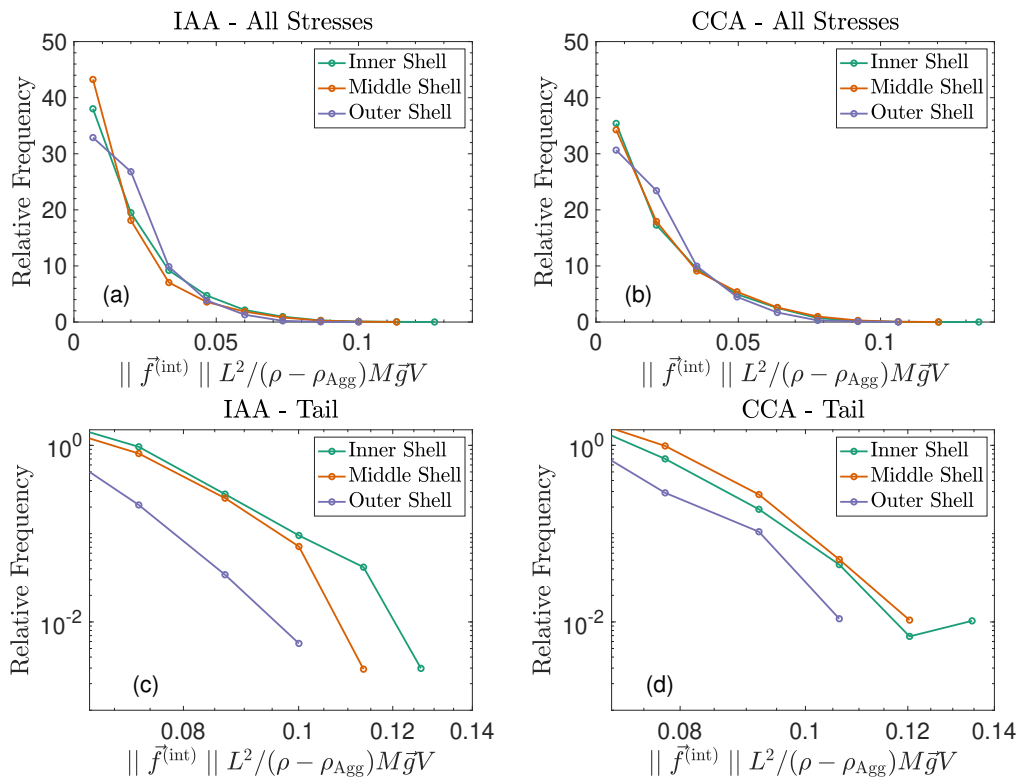
Figure 4.7:   Distribution of internal stresses for the Settling Case in the inner (green), middle (orange), and outer (purple) shells for IAA-type, panels (a) and (c), and CCA-type aggregates, panels (b) and (d). In panels (a) and (b) we show the full range of inner stresses found in the three shells, while in panels (c) and (d) we zoom in on the tail of the distribution and only display on a log-log scale the distribution of normalized stresses greater than half of the maximum internal stress computed for IAA-type and CCA-type aggregates, respectively.

only the stresses whose value is greater than half the maximum internal stress found across samples for IAA-type and CCA-type aggregates, respectively. In IAA-type aggregates the inner shell has roughly 2% of stresses that lie above this threshold, the middle shell has 1.5% of such stresses, and the outer shell only 0.3%. For CCA-type aggregates, the inner shell has 1.4% of large stresses, while the middle shell and outer shell have 2% and 0.5% of large stresses, respectively. We can see that the larger half of internal stresses distribute similarly in the two types of structures analyzed. In both cases, the outer shell contains far fewer large internal stresses in both structures, while the inner and middle shells contain a larger proportion. This indicates that settling IAA- and CCA- type aggregates are more likely to experience large stresses that could lead to rupture closer to their center of mass, rather than towards the far edges of their structure.

In fact, when we break up the aggregates in two at the location of the maximum internal stress, we find that the distribution of the relative masses of the newly formed aggregates is at least qualitatively similar for IAA-type and CCA-type aggregates, as shown in Figure 4.8. Here we analyze the relative masses of the two aggregates formed after rupture, compared to the mass of the original aggregate. From panel 4.8(a), it can be seen that IAA-type aggregates tend to break into a smaller aggregate made on average of 15% of the mass of the original aggregate, and a larger aggregate made of the remaining 85% of the original mass, as shown by the two high peaks located toward the tails of the distribution. From panel 4.8(b), it can be seen that the distribution of masses for CCA-type aggregates is more uniform. In fact, we find that CCA-type aggregates break into a smaller aggregate made on average of 20% of the mass of the original aggregate, and a larger aggregate made of the remaining 80% of the original mass. Moreover, if one focuses on the region in panels 4.8(a) and (b) where the abscissa is 0.5, it can be seen that CCA-type aggregates have a slightly higher tendency of breaking into two aggregates whose masses are roughly equal, compared to IAA-type aggregates. This agrees with the fact that, owing to their mode of formation, CCA-aggregates are more linear and often have a long thin connection between larger portions on either sides (see Figure 4.5), and thus, it is more likely that CCA-aggregates would lose a greater proportion of their original mass when breaking in two, compared to IAA-type aggregates.

Since the external force imposed in the Settling Case is proportional to the number of cubes M constituting a given aggregate, we verify whether the maximum internal stress also scales linearly with the mass of the aggregates. To this end, in Figure 4.9 we display a box and whisker plot for the maximum internal stress as a function of the number of cubes M in the aggregates, for IAA-type, panel (a), and CCA-type, panel (b), aggregates. The dashed black lines represent the best fits to the data. We see that on average the internal stresses scale nearly constantly with mass for both IAA-type and CCA-type aggregates, as expected, with a best fit of 0.077 for IAA and 0.073 for CCA

Figure 4.8: Relative mass for IAA-type, panel (a), and CCA-type aggregates, panel (b), for $M = 25, 50, 100, 150, 200$ for all the samples collected in our simulations. We display the ratio between the mass of the smaller of the two aggregate and the original in red, while the ratio between the larger of the two aggregates and the the original is shown in blue.

Figure 4.9:   Box and whisker plots of the maximum internal stress computed on each aggregate in the simulations, for IAA-type aggregates, panel (a), and CCA-type aggregates, panel (b), for the Settling Case. The black dashed line represents the best constant fit to the data, found to be 0.077 for IAA and 0.073 for CCA.

4.3.2 Shear Case
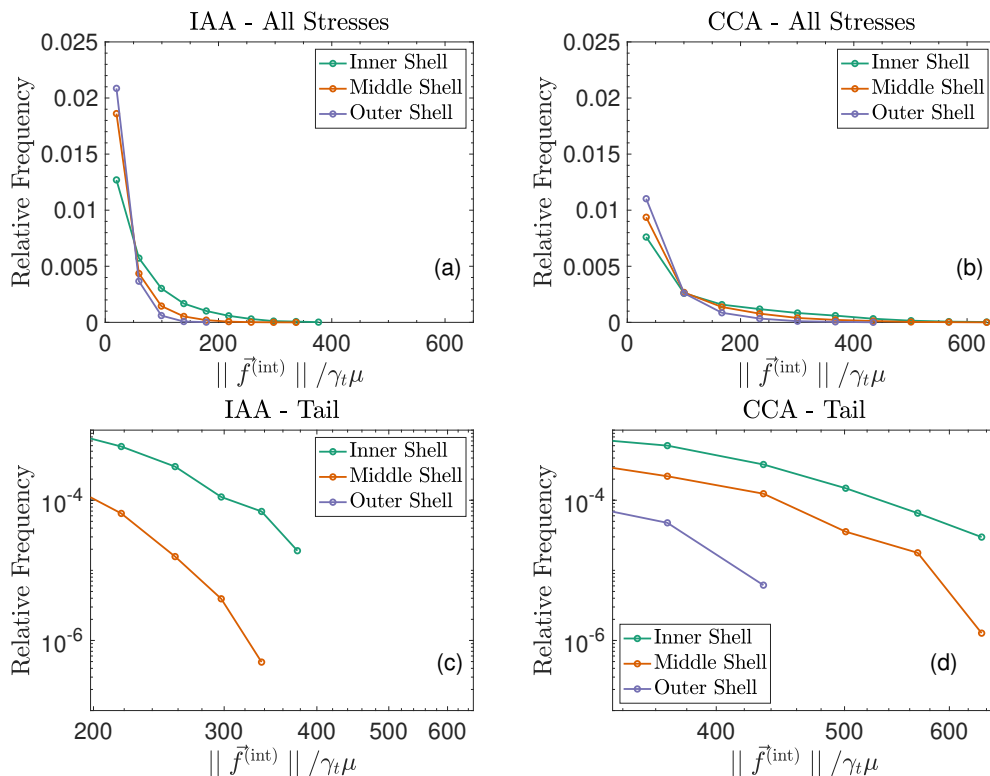
Figure 4.10: Distribution of internal stresses for the Shear Case in the inner (green), middle (orange), and outer (purple) shells for IAA-type, panels (a) and (c), and CCA-type aggregates, panels (b) and (d). In panels (a) and (b) we show the full range of inner stresses found in the three shells, while in panels (c) and (d) we zoom in on the tail of the distribution and only display on a log-log scale the distribution of normalized stresses greater than half of the maximum internal stress computed for IAA-type and CCA-type aggregates, respectively.

We now consider neutrally buoyant aggregates, subject to no force or torque in a turbulent background flow modeled as a local shear. In Figure 4.10 we show the distribution of internal stresses in the three shells discussed in Section 4.2.4, for 400 samples for IAA-type aggregates and CCA-type aggregates made of $M = 200$ cubes. In panels 4.10(a) and (b), we display the total range of stresses computed for IAA-type and CCA-type aggregates. As in the Settling Case, the overall trend is similar for both types of structures, with the internal stress density functions decaying monotonically away from

zero in all three shells. However, the evidence on whether the decay is consistent with a power law behavior is less conclusive than in the Settling Case and would require further data collection and analysis. In IAA-type aggregate, the inner shell has 4% of stresses that are greater than half the maximum internal stress found across samples in contrast to the middle shell that exhibits only 0.4% of such stresses, and to the outer shell where no stress greater than half the maximum stress is present. In CCA-type aggregates, the inner shell contains roughly 8% of stresses greater than half the maximum internal stress found across samples, the middle shell 3%, while the outer shell has only 0.4% of such stresses. We also note that the stresses induced by a shear flow are much larger in CCA-type aggregates, with the largest internal stress found across sample being almost a factor of two greater than in the IAA case. In panels 4.10(c) and (d) we focus on the tail of the distribution and use a log-log scale to show only the stresses equal or greater than half of the largest internal stress computed across samples, for IAA-type and CCA-type aggregates, respectively. We find that a greater proportion of large stresses consistently lie in the inner shell than in the middle and outer shell, for both types of aggregate.

The propensity of the largest stress caused by a shear flow to be located in the inner shell is reflected in the relative masses found after rupture, as shown in Figure 4.11. When we break the aggregate in two at the location of the maximum internal stress, we see that broken-up aggregates have more sizes closer to half the initial aggregate than in the Settling Case (see Figure 4.8), and that very small and very large broken-up aggregates are rare. In fact, for IAA-type aggregates, the average smaller aggregate has a mass that is roughly 28% of the original mass while the larger aggregate has a mass that is roughly 72% of the original mass. For CCA-type aggregates, we find that they tend to break into two aggregates whose relative masses are roughly 33% and 67% of the original mass, for the smaller and larger aggregate, respectively.

In Figure 4.12, we plot the norm of the nondimensional maximum internal stress computed for all the samples analyzed vs. the maximum radius of the aggregates, in a log-log scale, and perform linear regression to the data. We see that the maximum internal stress scales roughly quadratically with the aggregates' maximum radius, both for IAA-type and CCA-type aggregates, as shown by the black lines in panels (a) and (b), whose slopes are found to be 1.92 and 1.67, respectively. We note that since any shear can be written as the sum of a rotation and a strain

$$\vec{u}^\infty(\vec{x}) = \frac{1}{2}\vec{\omega} \wedge \vec{x} + \bar{\bar{E}}\vec{x}, \tag{4.25}$$
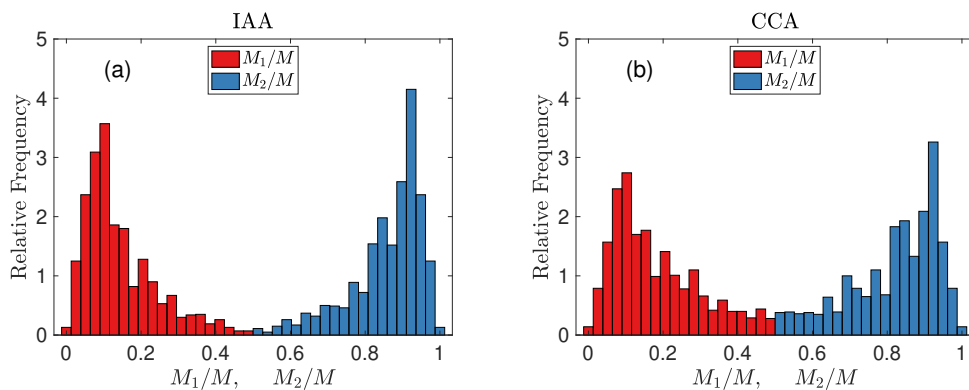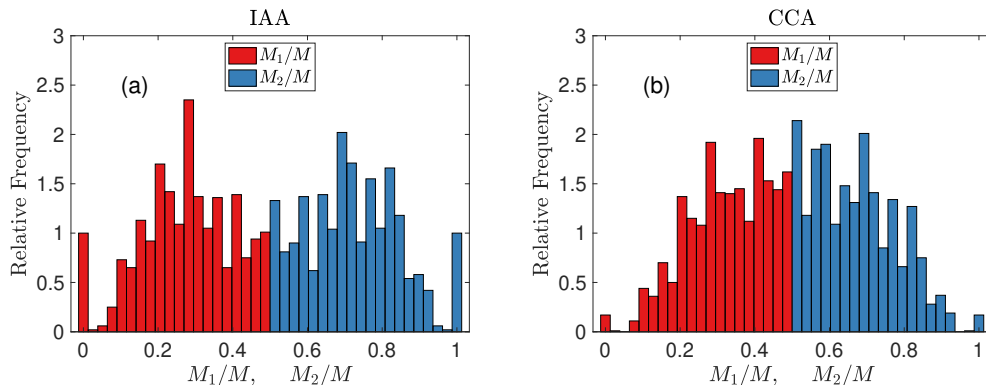
Figure 4.11: Relative mass for IAA-type, panel (a), and CCA-type aggregates, panel (b), for $M = 25, 50, 100, 150, 200$ for all the samples collected in our simulations. We display the ratio between the mass of the smaller of the two aggregate and the original in red, while the ratio between the larger of the two aggregates and the the original is shown in blue.
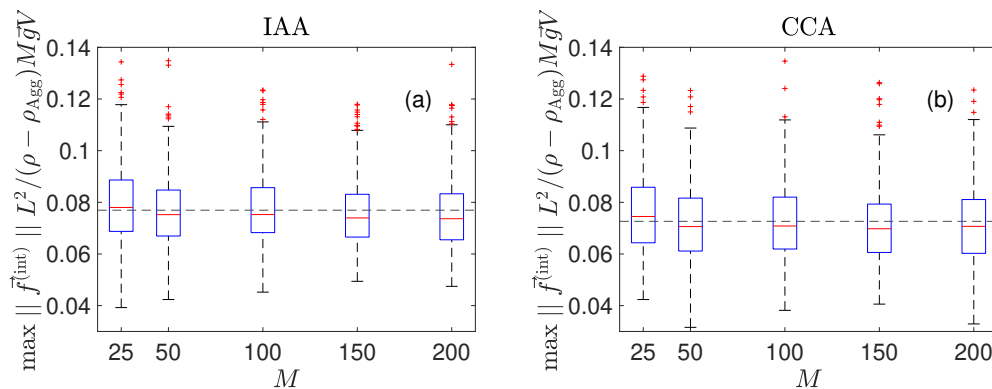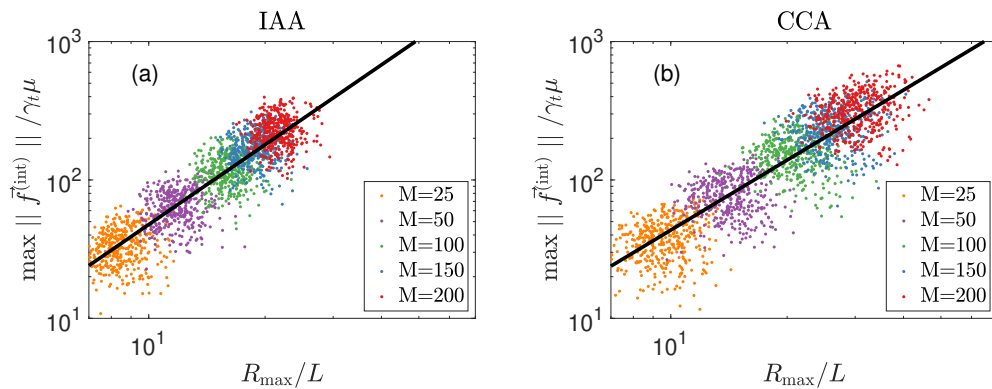

Figure 4.12: Plot of the maximum internal stress computed on each aggregate in the simulations, as a function of the maximum radius $R_{\max}$, for the case of a shear background flow, on a log-log scale, for all the samples collected in our simulations. The number of cubes in aggregates span from $M = 25$ to $M = 200$. The black lines represent the best linear fits to the data. The slopes of the lines were found to be 1.92 and 1.67 for IAA-type and CCA-type aggregates, respectively.

in our case one can set $\vec{\omega} = -\gamma_t \hat{k}$ for the angular velocity, and

$$\bar{\bar{E}} = \frac{1}{2} \begin{bmatrix} 0 & \gamma_t & 0 \\ \gamma_t & 0 & 0 \\ 0 & 0 & 0 \end{bmatrix} \qquad (4.26)$$

for the strain tensor, and then use Eq. (4.25) to impose the background flow $\vec{u}^\infty(\vec{x}) = \gamma_t y [1, 0, 0]^T$. It was shown in Ref. [106] that extensional flows cause a straining force that scales quadratically with the characteristic length-scale of fractal aggregates. As it can be seen from the best-fits (black lines) in Figure 4.12(a) and (b), roughly the same scaling is found between the maximum internal stresses in the aggregates and the maximum radius. Thus, our findings indicate that the extensional contribution to the shear flow is what induces the internal stresses on the aggregates, and suggest that solid objects exposed to a rotational background flow would simply freely rotate with the flow, experiencing no internal stresses as a result. Consistent with our findings on the distribution of all the internal stresses induced by a shear flow, see Figure 4.10, we also observe that CCA-type aggregates experience much larger maximum internal stresses under shear than IAA-type aggregates, presumably because their maximum radius is greater which allows for a greater impact of the extensional portion of the flow.

4.4 Conclusions

In this work, we implemented a boundary integral formulation of Stokes Equations to characterize stresses induced on fractal aggregates by an external force or background flow. We studied the external and internal stresses in marine aggregates of different densities settling under gravity in a fluid at rest, or exposed to a laminar shear flow in the absence of forces. We investigated the impact of these different conditions on the distribution of internal stresses in the aggregates, and quantified how the largest stresses scale with the mass and size of the aggregates.

We found that imposing an external force proportional to the mass of the aggregates (Settling Case) induces internal stresses of a magnitude that scales as the aggregate's weight divided by the area of a single square, with a proportionality constant of approximately 0.08. The stress distribution was found to be similar in more compact aggregates (IAA) and less compact ones (CCA), with a power-law decay with exponent approximately -3 in both cases, indicating that the same distribution can probably be used to model the stresses of aggregates with different fractal dimensions. When aggregates were allowed to break at the location of the maximum internal stress, we found that the relative masses of the newly formed objects distribute in a fairly uneven manner, and

that aggregates of both types rarely break at the far edges of their structure. On average, IAA-type aggregates break up in two aggregates whose relative masses are roughly 85% and 15% of the original mass, for the larger and smaller aggregate, respectively, while CCA-type aggregates break up in two aggregates whose relative masses are roughly 80% and 20% of the original mass, for the larger and smaller aggregate, respectively. This is also consistent with the fact that regions closer to the center of the aggregates have a greater number of large stresses compared to the far edges, both for IAA- and CCA-type aggregates. While the overall distribution of the relative masses is similar in both types of aggregates, it is noteworthy that CCA-type aggregates have a greater likelihood to break close to their center of mass, compared to IAA-type aggregates, and thus would sometimes, albeit rarely, yield aggregates whose masses are roughly equal. This is likely a consequence of the way CCA-type aggregates are built. As clusters of different sizes collide into each other, they typically merge via one of the longer branches in their structure. Thus, the resulting aggregate tends to have a less compact region near its center of mass, which is more likely to experience largest stresses, and thus break up, as a result of settling.

In aggregates exposed to laminar shear in the absence of forces (Shear Case), we found that the largest stresses are much more likely to be found close to the center of mass for both IAA- and CCA-type aggregates with an even greater prevalence than for the Settling Case. The stress distribution was again found to be qualitatively similar in more compact aggregates (IAA) and less compact ones (CCA) across shells, exhibiting a power-law behavior, with exponent of roughly -2 for the inner shell, where most of the large stresses are found, for both aggregate types. This indicates that to model stresses sufficiently large to lead to rupture, in aggregates exposed to laminar shear, the same distribution can likely be used. We also note that CCA aggregates experience larger stresses than IAA aggregates for a given mass, as CCA aggregates have a greater span that is more affected by shear than IAA aggregates. When allowed to break at the location of the maximum internal stress, we found that the relative masses of the newly formed objects distribute roughly uniformly. On average, IAA-type aggregates break up in two aggregates whose relative masses are roughly 72% and 28% of the original mass, for the larger and smaller aggregate, respectively, while CCA-type aggregates break up in two aggregates whose relative masses are roughly 67% and 33% of the original mass, for the larger and smaller aggregate, respectively. In addition, we found that the maximum internal stress scales almost quadratically with the maximum radius of the aggregates, as it grows like $\max||\vec{f}^{(\mathrm{int})}|| \sim (R_{\max})^{1.92}$ for IAA-type aggregates and $\max||\vec{f}^{(\mathrm{int})}|| \sim (R_{\max})^{1.67}$ for CCA-type aggregates. Since it was shown in Ref. [106] that an extensional flow acting on aggregates would induce a straining force that scales quadratically with their characteristic length scale, our findings indicate that when aggregates are exposed to laminar shear, it is

the extensional component of the shear flow that induces stresses in the aggregates.

This study gives insights on how to build a more accurate reversible aggregation model. For instance, our findings indicate how stochastically-generated internal stresses should be distributed based on their distance to the center of mass of the aggregate. From our results we expect that CCA-type objects would tend to break into denser and denser objects whose structures resemble that of IAA-type aggregates. Moreover, for a given density difference, aggregates would likely reach a maximal size before the stresses induced by their settling causes them to break. Furthermore, while we modeled the action of laminar shear as it is physically relevant and often studied in experimental settings [91], we found that the leading cause of stress in aggregates exposed to shear comes from the extensional component of the flow, rather than the rotational one. Thus, if a model of aggregate dynamics were to include the action of a background flow, our results suggest that the incorporation of an extensional flow would capture the dominant effects while the translational and rotational components of the flows would have less impact.

Chapter 5

Conclusion and future work

In this Thesis, I presented three frameworks that describe simulations of fluid systems at small scales and discussed how these frameworks can be used to model the behavior of reactive gas mixtures and characterize aggregate dynamics. In Chapter 2, I presented the framework of reactive fluctuating hydrodynamics (RFHD), and showed that this continuum-stochastic approach is well-suited to model the dynamics of reactive gases at the mesoscale. As discussed in Section 2.2, the incorporation of stochastic chemistry into the framework of fluctuating hydrodynamics is achieved by the inclusion of a source term, modeled via a chemical Langevin equation (CLE) approach, into the fluctuating Navier Stokes equations [63]. This allows to accurately model the transport properties of fluids at the mesoscale [94], and properly characterize the stochastic nature of chemical reactions, without resorting to a particle-based description of the chemistry. Moreover, it was shown in Section 2.4.2 that this CLE-based formulation can be readily incorporated into existing massively parallelized solvers for non-reactive FHD [16] thus combining high fidelity and computational efficiency.

An example where these processes are important is at the onset of density-driven instabilities in fluids. It is also known both from experiments [65] and numerical simulations [55] that in systems where fluids are separated by a flat interface in the presence of a density gradient, thermal fluctuations play a fundamental role in the onset of fingering patterns instability. When reaction is also present, it was found that these systems show asymmetric and much faster growth of these fingering patterns, compared to non-reactive systems. Since it was shown in Section 2.4.3 that to properly capture thermal fluctuations in reactive gas mixtures, one needs to fully characterize the temperature dependence of the rate constants, our RHFD model would then greatly extend the ability of existing frameworks to accurately reproduce the onset of instability in certain reactive fluid mixtures. Another example in which the findings of this research could be useful

is to help design more accurate numerical methods to simulate heterogeneous catalysis [35], a key component of many industrial processes, ranging from the refining of crude oil, to the synthesis of organic and inorganic chemicals [87]. This type of reaction usually involves a solid catalytic surface where gas-phase chemicals react, releasing the products of these reactions onto a surrounding reactive gas. Since this process is characterized by the interaction of a gas phase and a solid surface, then the formulation discussed in Section 2.2 could be critical to realistically simulate the behavior of the reactive bulk of gas in these systems. In particular, close to the catalytic surface, at mesoscopic scales, accurately capturing the impact of thermal fluctuations in the reactive gas can be essential to ensure the proper exchange of information between the gas and solid phase.

In Chapters 3 and 4, I discussed the importance of various aspects that contribute to the dynamical evolution of aggregates in low Reynolds number regimes. In Chapter 3, I presented a novel particle-based approach to model the formation mechanisms of fractal aggregates, based on the framework of Diffusion-Limited Cluster Aggregation (DLCA). Traditionally, the fluids community has studied aggregates for the role they play in the oceanic carbon cycle [44], as they subtract carbon dioxide from the atmosphere and sink from the surface of the ocean towards the ocean floor. In my model, improving on traditional DLCA approaches, clusters are allowed to randomly rotate, and the impact of aggregates' size on their diffusivity is accounted for to characterize their dynamical evolution. I investigated how rotational effects, size-dependent diffusivities and settling impact the aggregates' fractal dimension and growth rate. I found that rotation accelerates the growth of the aggregates as it increases aggregate motion and raises the likelihood of collision. Rotation was also found to decrease the resulting aggregates' fractal dimension, again a result consistent with increasing the likelihood that long, narrow limbs encounter each other as they rotate. I also found that size-dependent diffusivities slow down the growth of the aggregate, but have little to no impact on their fractal dimension. Finally, the incorporation of settling into the model led to clusters that grow more quickly, are smaller in their vertical than in their horizontal extents, and have a lower fractal dimension than typical DLCA aggregates.

In Chapter 4, I discussed a boundary integral formulation of Stokes equations to characterize the stresses in aggregates exposed to some external force or background flow. This continuum deterministic approach is useful to model fluid flow around solid objects in low Reynolds number regimes. This framework is used to compute the flow and stresses on fractal aggregates made of cubic particles whose boundary is a simple collection of squares. On such a simple boundary, one can compute the internal and external stresses induced by the action of some background flow or external force and even treat analytically the apparent singularity that arises. I analyzed how the type of conditions that aggregates are exposed to affect the distribution of stresses in aggregates of different structures. I

found that, when settling in a fluid at rest, both more compact and less compact aggregates experience small stresses that scale as about 8% of their weight. Moreover, when allowed to break at the location of the maximum internal stress, the relative masses of the two newly formed aggregates distribute well away from an even balance. However, less compact aggregates, have a slightly higher likelihood to also break closer to their center of mass, compared to more compact ones. On the other end, when exposed to a shear background flow, both more compact and less compact aggregates tend to experience large stresses closer to their center of mass. This leads to a more uniform distribution for the relative masses of the newly formed aggregates. Furthermore, for both more and less compact aggregates exposed to laminar shear, the maximum stress scales roughly quadratically with the maximum radius of the aggregates, indicating that the extensional component of the flow is what induces the stresses.

The models presented in Chapters 3 and 4 provide valuable insights on how to properly characterize the formation and disruption mechanisms of aggregates and aim to better describe aggregates typically observed in experiments [90]. To the best of my knowledge, aggregation models typically do not include stochastic background flows, and thus are not capable of capturing the effects of localized eddies, which might cause variations in translational and rotational diffusivities to an even greater extent than molecular motion. In Section 3.5, it was shown that the way in which diffusivities are modeled has a significant impact on the growth of aggregates, and thus capturing the effects of localized eddies could be important to properly characterize aggregates formation. Furthermore, while most aggregation models tend to only study the structure of the aggregates [50], the growth rate of aggregates should also be analyzed, as it can help estimate the time that marine aggregates spend in a water column. The results provided in Chapter 3 can help give a more realistic description of an aggregate's progression towards the deep ocean. One other important feature, in addition to size-dependent diffusivities, that is typically under-discussed in most models is the impact of gravitational effects on aggregate growth dynamics. In Section 3.5.3, it was shown that accounting for gravitational effects in the formation mechanism of aggregates, via the incorporation of a size-dependent settling speed, leads to a speed-up in the aggregates growth, and that capturing this effect is particularly critical for large aggregates. These aggregates, in turn, are also more likely to experience stresses large enough to lead to break-up. In Chapter 4, I showed that aggregates settling under the influence of gravity experience large stresses that tend to lead to rupture away from their edges. Moreover, many recent experimental efforts have aimed to characterize the breaking of marine aggregates exposed to some background flow [90]. Given that the formulation discussed in Section 4.2 allows for the ready incorporation of background flows in the model, this approach is well-equipped to provide a more realistic description of disaggregation typically observed in experiments [91]. In this context, the

findings of Section 4.3.2 could also be a integral part in the design of experiments that aim to reproduce the breaking of marine aggregates in a realistic and efficient manner. For instance, since it was shown that it is the extensional component of a laminar shear flow that induces stresses in aggregates, this can give insights on how to construct more efficient experimental settings to characterize disaggregation. Ultimately, providing a well-justified disaggregation mechanism is an important step toward obtaining a more complete, and physically relevant model of aggregation that extends beyond the early stages of formation. Furthermore, while the realistic description of aggregates break-up is extremely important especially in the context of marine systems, the results of this model could be extended to other types of aggregates. For instance, granular aggregates have a tendency to deform [79] rather than break, and thus the characterization of the external and internal stresses discussed in Chapter 4 could be useful in settings where capturing aggregates deformation is also relevant.

In conclusion, the research that I conducted during my Ph.D. is relevant to fields spanning from chemistry to oceanography, and its results can help advance our understanding of many physical processes. This research helped me foster an interest in the study of Fluid Dynamics within the broader context of multi- and interdisciplinary Science. Therefore, I hope to continue working on the mathematical and numerical modeling of fluid systems, and that the work I conducted during my Ph.D. will be valuable to help me extend my career and research horizons. I aim to widen my understanding of numerical methods for Partial Differential Equations, and study physical phenomena where the interaction of multiple scales, and the presence of multi-physics, require the design of massively parallelized software optimized for distributed multi-core architectures and modern GPU computing.

Bibliography

[1] P. J. Linstrom and W. G. Mallard, Eds., *NIST Chemistry WebBook*, NIST Standard Reference Database Number 69, National Institute of Standards and Technology, Gaithersburg MD, 20899. Web address: `https : / / webbook . nist . gov / chemistry`.

[2] E. V.-E. A. Donev, A. L. Garcia, and J. B. Bell, *On the accuracy of finite-volume schemes for fluctuating hydrodynamics*, 2010.

[3] H. M. Aktulga, S. A. Pandit, A. C. T. van Duin, and A. Y. Grama, "Reactive molecular dynamics: numerical methods and algorithmic techniques", SIAM Journal on Scientific Computing **34**, C1–C23 (2012).

[4] F. Alexander and A. Garcia, "The direct simulation monte carlo method", Computers in Physics **11**, 588–593 (1997).

[5] A. L. Alldredge, T. J. Cowles, S. MacIntyre, J. E. B. Rines, P. L. Donaghay, C. F. Greenlaw, D. V. Holliday, M. M. Dekshenieks, J. M. Sullivan, and J. R. V. Zaneveld, "Occurrence and mechanisms of formation of a dramatic thin layer of marine snow in a shallow Pacific fjord", Mar. Ecol. Prog. Ser. **233**, 1–12 (2002).

[6] A. L. Alldredge and C. Gotschalk, "In situ settling behavior of marine snow1", Limnology and Oceanography **33**, 339–351 (1988).

[7] A. L. Alldredge and M. W. Silver, "Characteristics, dynamics and significance of marine snow", Prog. Oceanogr. **20**, 41–82 (1988).

[8] G. Amati and P. Gualtieri, "Serial and parallel performance using a spectral code", in *Parallel computational fluid dynamics 2000*, edited by C. Jenssen, H. Andersson, A. Ecer, N. Satofuka, T. Kvamsdal, B. Pettersen, J. Periaux, and P. Fox (North-Holland, Amsterdam, 2001), pp. 157–163.

[9]G. C. Ansell and E. Dickinson, "Short-range structure of simulated colloidal aggregates", Phys. Rev. A **35**, 2349–2352 (1987).

[10]F. Argoul, A. Arneodo, G. Grasseau, and H. L. Swinney, "Self-similarity of diffusion-limited aggregates and electrodeposition clusters", Phys. Rev. Lett. **61**, 2558–2561 (1988).

[11]M. Arribas, A. Elipe, and M. Palacios, "Quaternions and the rotation of a rigid body", Celest. Mech. Dyn. Astron. **96**, 239–251 (2006).

[12]R. D. Astumian and P. Hänggi, "Brownian motors", Phys. Today **55**, 33–39 (2002).

[13]K. Balakrishnan, A. L. Garcia, A. Donev, and J. B. Bell, "Fluctuating hydrodynamics of multispecies nonreactive mixtures", Phys. Rev. E **89**, 013017 (2014).

[14]C. J. Bates, I. Yildirim, J. B. Tenenbaum, and P. Battaglia, "Modeling human intuitions about liquid flow with particle-based simulation", en, PLoS Comput. Biol. **15**, e1007210 (2019).

[15]J. B. Bell, A. L. Garcia, and S. A. Williams, "Computational fluctuating fluid dynamics", ESAIM: Math. Model. Numer. Anal. **44**, 1085–1105 (2010).

[16]J. B. Bell, A. Nonaka, C. Kim, D. Ladiges, and A. Donev, *Stochastic hybrid models and algorithms for fluids (fhdex) v1*, [Computer Software] `https://doi.org/10.11578/dc.20190122.2`, Jan. 2018.

[17]D. Bertsekas and W. Rheinboldt, *Constrained optimization and lagrange multiplier methods*, Computer science and applied mathematics (Elsevier Science, 2014).

[18]A. K. Bhattacharjee, K. Balakrishnan, A. L. Garcia, J. B. Bell, and A. Donev, "Fluctuating hydrodynamics of multi-species reactive mixtures", J. Chem. Phys. **142**, 224107 (2015).

[19]X. Bian, C. Kim, and G. E. Karniadakis, "111 years of Brownian motion", Soft Matter **12**, 6331 (2016).

[20]X. Bian, C. Kim, and G. E. Karniadakis, "111 years of brownian motion", en, Soft Matter **12**, 6331–6346 (2016).

[21]P. Borrell, C. J. Cobos, and K. Luther, "Falloff curve and specific rate constants for the reaction $NO_2 + NO_2 \rightleftarrows N_2O_4$", J. Phys. Chem. **92**, 4377–4384 (1988).

[22]R. Brady and R. Ball, "Fractal growth of copper electrodeposits", Nature **309**, 225–229 (1984).

[23]C. Brouzet, R. Guiné, M.-J. Dalbe, B. Favier, N. Vandenberghe, E. Villermaux, and G. Verhille, "Laboratory model for plastic fragmentation in the turbulent ocean", Physical Review Fluids **6**, 024601 (2021).

[24] A. B. Burd and G. A. Jackson, "Particle aggregation", Ann. Rev. Mar. Sci. **1**, 65–90 (2009).

[25] J. Cai, N. Lu, and C. M. Sorensen, "Analysis of fractal cluster morphology parameters: structural coefficient and density autocorrelation function cutoff", J. Colloid Interface Sci. **171**, 470–473 (1995).

[26] R. K. Chakrabarty, H. Moosmüller, W. P. Arnott, M. A. Garro, G. Tian, J. G. Slowik, E. S. Cross, J.-H. Han, P. Davidovits, T. B. Onasch, and D. R. Worsnop, "Low fractal dimension cluster-dilute soot aggregates from a premixed flame", Phys. Rev. Lett. **102**, 235504 (2009).

[27] A. J. Chorin, "Numerical solution of the navier-stokes equations", Mathematics of Computation **22**, 745–762 (1968).

[28] R. Coyle, G. Hardiman, and K. O. Driscoll, "Microplastics in the marine environment: a review of their sources, distribution processes, uptake and exchange in ecosystems", Case Studies in Chemical and Environmental Engineering **2**, 100010 (2020).

[29] H. M. De La Rosa Zambrano, G. Verhille, and P. Le Gal, "Fragmentation of magnetic particle aggregates in turbulence", Phys. Rev. Fluids **3**, 084605 (2018).

[30] P. J. W. Debye, *Polar molecules* (Dover, New York, 1929).

[31] D. Drikakis, M. Frank, and G. Tabor, "Multiscale computational fluid dynamics", Energies **12**, `10.3390/en12173272` (2019).

[32] A. Einstein, *Investigations on the theory of the Brownian motion* (Dover, New York, 1956).

[33] M. Feig, G. Nawrocki, I. Yu, P.-H. Wang, and Y. Sugita, "Challenges and opportunities in connecting simulations with experiments via molecular dynamics of cellular environments", en, J. Phys. Conf. Ser. **1036**, 012010 (2018).

[34] Z. V. Finkel, J. Beardall, K. J. Flynn, A. Quigg, T. A. V. Rees, and J. A. Raven, "Phytoplankton in a changing world: cell size and elemental stoichiometry", Journal of Plankton Research **32**, 119–137 (2009).

[35] C. M. Friend and B. Xu, "Heterogeneous catalysis: a central science for a sustainable future", Acc. Chem. Res. **50**, 517–521 (2017).

[36] G. Frungieri and M. Vanni, "Aggregation and breakup of colloidal particle aggregates in shear flow: a combined monte carlo - stokesian dynamics approach", Powder Technology **388**, 357–370 (2021).

[37] J. Gallier and D. Xu, "Computing exponentials of skew symmetric matrices and logarithms of orthogonal matrices", Int. J. Robot. Autom. **17**, 1–11 (2002).

[38]M. Garbey, M. Hess, P. Piras, M. Resch, and D. Tromeur-Dervout, "Numerical algorithms and software tools for efficient meta-computing", in *Parallel computational fluid dynamics 2000*, edited by C. Jenssen, H. Andersson, A. Ecer, N. Satofuka, T. Kvamsdal, B. Pettersen, J. Periaux, and P. Fox (North-Holland, Amsterdam, 2001), pp. 225–232.

[39]A. Gastaldi and M. Vanni, "The distribution of stresses in rigid fractal-like aggregates in a uniform flow field", Journal of Colloid and Interface Science **357**, 18–30 (2011).

[40]D. T. Gillespie, "A general method for numerically simulating the stochastic time evolution of coupled chemical reactions", J. Comp. Phys. **22**, 403–434 (1976).

[41]V. Giovangigli, *Multicomponent flow modeling*, Modeling and Simulation in Science, Engineering and Technology (Birkhäuser, Boston, 2012).

[42]J. Happel and H. Brenner, *Low reynolds number hydrodynamics: with special applications to particulate media*, Prentice-Hall international series in the physical and chemical engineering sciences (Prentice-Hall, 1965).

[43]J. O. Hirschfelder, C. F. Curtiss, and R. B. Bird, *Molecular theory of gases and liquids* (John Wiley and Sons, INC., New York, 1954).

[44]S. Honjo, T. Eglinton, C. Taylor, K. Ulmer, S. Sievert, A. Bracher, C. German, V. Edgcomb, R. Francois, M. Iglesias-Rodriguez, B. Van Mooy, and D. Rapeta, "Understanding the role of the biological pump in the global carbon cycle: an imperative for ocean science", Oceanography **27**, 10–16 (2014).

[45]IUPAC, *Compendium of chemical terminology (the "gold book")*, 2nd (Blackwell Scientific Publications, Oxford, 1997).

[46]G. A. Jackson and A. B. Burd, "Aggregation in the marine environment", Env. Sci. Tech. **32**, 2805–2814 (1998).

[47]J.-M. Jin, K. Parbhakar, L. H. Dao, and K. H. Lee, "Gel formation by reversible cluster-cluster aggregation", Phys. Rev. E **54**, 997–1000 (1996).

[48]C. P. Johnson, X. Li, and B. E. Logan, "Settling velocities of fractal aggregates", Environ. Sci. Technol. **30**, 1911–1918 (1996).

[49]S. Jungblut, J.-O. Joswig, and A. Eychmüller, "Diffusion- and reaction-limited cluster aggregation revisited", Phys. Chem. Chem. Phys. **21**, 5723–5729 (2019).

[50]S. Jungblut, J.-O. Joswig, and A. Eychmüller, "Diffusion-limited cluster aggregation: impact of rotational diffusion", J. Phys. Chem. C **123**, 950–954 (2019).

[51]Y. Kantor and W. T.-A., "Mechanical stability of tenuous objects", Journal de Physique Lettres, Edp sciences **45**, 675–679 (1984).

[52]R. J. Kee, F. M. Rupley, E. Meeks, and J. A. Miller, *CHEMKIN-III: a FORTRAN chemical kinetics package for the analysis of gas-phase chemical and plasma kinetics*, tech. rep. (Sandia National Lab. (SNL-CA), Livermore, CA (United States), 1996).

[53]J. Keizer, *Statistical thermodynamics of nonequlibrium processes* (Springer-Verlag, New York, 1987).

[54]J. R. Kilps, B. E. Logan, and A. L. Alldredge, "Fractal dimensions of marine snow determined from image analysis of in situ photographs", Deep Sea Res. Part I: Oceanographic Res. Pap. **41**, 1159–1169 (1994).

[55]C. Kim, A. Nonaka, J. B. Bell, A. L. Garcia, and A. Donev, "Fluctuating hydrodynamics of reactive liquid mixtures", J. Chem. Phys. **149**, 084113 (2018).

[56]C. Kim, A. Nonaka, J. B. Bell, A. L. Garcia, and A. Donev, "Stochastic simulation of reaction-diffusion systems: a fluctuating-hydrodynamics approach", J. Chem. Phys. **146**, 124110 (2017).

[57]K. S. Kim, C. Kim, G. E. Karniadakis, E. K. Lee, and J. J. Kozak, "Density-dependent finite system-size effects in equilibrium molecular dynamics estimation of shear viscosity: hydrodynamic and configurational study", J. Chem. Phys. **151**, 104101 (2019).

[58]M. Kolb, "Reversible diffusion-limited cluster aggregation", Journal of Physics A: Mathematical and General **19**, L263–L268 (1986).

[59]M. Kolb, R. Botet, and R. Jullien, "Scaling of kinetically growing clusters", Phys. Rev. Lett. **51**, 1123–1126 (1983).

[60]D. Kondepudi, *Introduction to modern thermodynamics* (Wiley, 2008).

[61]P. Kundu and I. Cohen, *Fluid mechanics* (Elsevier Science, 2010).

[62]K. J. Laidler, "A glossary of terms used in chemical kinetics, including reaction dynamics (IUPAC Recommendations 1996)", Pure Appl. Chem. **68**, 149–192 (1996).

[63]L. D. Landau and E. M. Lifschitz, eds., *Statistical physics vol 5 course of theoretical physics* (Pergamon Press, 1958).

[64]J. H. Lee, C. Kim, and M. E. Colvin, "Molecular dynamics studies of the melting kinetics of superheated crystals", J. Phys. Chem. C **126**, 4199 (2022).

[65]L. Lemaigre, M. A. Budroni, L. A. Riolfo, P. Grosfils, and A. De Wit, "Asymmetric Rayleigh-Taylor and double-diffusive fingers in reactive systems", Physics of Fluids **25**, 014103 (2013).

[66]A. Lemarchand and B. Nowakowski, "Fluctuation-induced and nonequilibrium-induced bifurcations in a thermochemical system", Mol. Simul. **30**, 773–780 (2004).

[67] R. J. LeVeque, *Finite difference methods for ordinary and partial differential equations* (Society for Industrial and Applied Mathematics, 2007).

[68] R. J. LeVeque, *Finite volume methods for hyperbolic problems*, Cambridge Texts in Applied Mathematics (Cambridge University Press, 2002).

[69] M. Y. Lin, H. M. Lindsay, D. A. Weitz, R. C. Ball, R. Klein, and P. Meakin, "Universal reaction-limited colloid aggregation", Phys. Rev. A **41**, 2005–2020 (1990).

[70] P. J. Linstrom and W. G. Mallard, "The NIST Chemistry WebBook: A chemical data resource on the internet", J. Chem. Eng. Data **46**, 1059–1063 (2001).

[71] B. E. Logan and D. B. Wilkinson, "Fractal geometry of marine snow and other biological aggregates", Limnol. Oceanogr. **35**, 130–136 (1990).

[72] J. A. Manion, R. E. Huie, R. D. Levin, D. R. Burgess Jr., V. L. Orkin, W. Tsang, W. S. McGivern, J. W. Hudgens, V. D. Knyazev, D. B. Atkinson, E. Chai, A. M. Tereza, C.-Y. Lin, T. C. Allison, W. G. Mallard, F. Westley, J. T. Herron, R. F. Hampson, and D. H. Frizzell, *NIST Chemical Kinetics Database*, NIST Standard Reference Database 17, Version 7.0 (Web Version), Release 1.6.8, Data version 2015.09, National Institute of Standards and Technology, Gaithersburg, Maryland, 20899-8320. Web address: `https://kinetics.nist.gov`.

[73] P. Meakin, "Diffusion-controlled cluster formation in 2–6-dimensional space", Phys. Rev. A **27**, 1495–1507 (1983).

[74] P. Meakin, "Diffusion-limited aggregation in three dimensions: results from a new cluster-cluster aggregation model", J. Colloid Interface Sci. **102**, 491–504 (1984).

[75] P. Meakin, "Formation of fractal clusters and networks by irreversible diffusion-limited aggregation", Phys. Rev. Lett. **51**, 1119–1122 (1983).

[76] P. Meakin, "The effects of rotational diffusion on the fractal dimensionality of structures formed by cluster–cluster aggregation", J. Chem. Phys. **81**, 4637–4639 (1984).

[77] P. Messina, "The exascale computing project", Computing in Science & Engineering **19**, 63–67 (2017).

[78] E. Moro, "Hybrid method for simulating front propagation in reaction-diffusion systems", Phys. Rev. E **69**, 060101 (2004).

[79] A. Muqtadir, S. Al-Dughaimi, and J. Dvorkin, "Deformation of granular aggregates: static and dynamic bulk moduli", Journal of Geophysical Research: Solid Earth **125**, e2019JB018604 (2020).

[80] E. C. Okonkwo, I. Wole-Osho, I. W. Almanassra, Y. M. Abdullatif, and T. Al-Ansari, "An updated review of nanofluids in various heat transfer devices", J. Therm. Anal. Calorim. **145**, 2817–2872 (2021).

[81] M. Özcan, "Why equilibrium constants are unitless", J. Phys. Chem. Lett. **13**, 3507–3509 (2022).

[82] M. Polimeno, C. Kim, and F. Blanchette, "Toward a realistic model of diffusion-limited aggregation: rotation, size-dependent diffusivities, and settling", ACS Omega **7**, 40826–40835 (2022).

[83] C. Pozrikidis, *Boundary integral and singularity methods for linearized viscous flow*, Cambridge Texts in Applied Mathematics (Cambridge University Press, 1992).

[84] J. Rotne and S. Prager, "Variational treatment of hydrodynamic interaction in polymers", J. Chem. Phys. **50**, 4831–4837 (1969).

[85] P. G. Saffman and M. Delbrück, "Brownian motion in biological membranes", Proc. Nat. Acad. Sci. **72**, 3111–3113 (1975).

[86] F. Sassa, G. C. Biswas, and H. Suzuki, "Microfabricated electrochemical sensing devices", Lab Chip **20**, 1358–1389 (2020).

[87] M. Schmal, *Heterogeneous catalysis and its industrial applications* (Springer International Publishing, 2016).

[88] A. Sengar, J. Kuipers, R. van Santen, and J. Padding, "Towards a particle based approach for multiscale modeling of heterogeneous catalytic reactors", Chemical Engineering Science **198**, 184–197 (2019).

[89] A. Sharma, M. J. Brazell, G. Vijayakumar, S. Ananthan, L. Cheung, N. deVelder, M. T. Henry-de-Frahan, N. Matula, P. Mullowney, J. Rood, P. Sakievich, A. Almgren, P. S. Crozier, and M. Sprague, "Exawind: open-source cfd for hybrid-rans/les geometry-resolved wind turbine simulations in atmospheric flows", Wind Energy **27**, 225–257 (2024).

[90] Y. Song and M. J. Rau, "A novel method to study the fragmentation behavior of marine snow aggregates in controlled shear flow", Limnology and Oceanography: Methods **20**, 618–632 (2022).

[91] Y. Song and M. J. Rau, "Viscous fluid flow inside an oscillating cylinder and its extension to Stokes' second problem", Physics of Fluids **32**, 043601, 10.1063/1.5144415 (2020).

[92] C. M. Sorensen, "The mobility of fractal aggregates: a review", Aerosol Sci. Tech. **45**, 765–779 (2011).

[93]C. M. Sorensen, J. Cai, and N. Lu, "Light-scattering measurements of monomer size, monomers per aggregate, and fractal dimension for soot aggregates in flames", Appl. Opt. **31**, 6547–6557 (1992).

[94]I. Srivastava, D. R. Ladiges, A. J. Nonaka, A. L. Garcia, and J. B. Bell, "Staggered scheme for the compressible fluctuating hydrodynamics of multispecies fluid mixtures", Phys. Rev. E **107**, 015305 (2023).

[95]M. M. Takayasu and F. Galembeck, "Determination of the equivalent radii and fractal dimension of polystyrene latex aggregates from sedimentation coefficients", J. Colloid Interface Sci. **202**, 84–88 (1998).

[96]M. Tong, "Review of particle-based computational methods and their application in the computational modelling of welding, casting and additive manufacturing", Metals **13**, `10.3390/met13081392` (2023).

[97]M. E. Tuckerman, B. J. Berne, and G. J. Martyna, "Molecular dynamics algorithm for multiple time scales: Systems with long range forces", The Journal of Chemical Physics **94**, 6811–6815 (1991).

[98]A. Vailati, R. Cerbino, S. Mazzoni, C. J. Takacs, D. S. Cannell, and M. Giglio, "Fractal fronts of diffusion in microgravity", Nat. Commun. **2**, 290 (2011).

[99]N. VAN KAMPEN, "Chapter ix - the langevin approach", in *Stochastic processes in physics and chemistry (third edition)*, edited by N. VAN KAMPEN, Third Edition, North-Holland Personal Library (Elsevier, Amsterdam, 2007), pp. 219–243.

[100]N. VAN KAMPEN, "Chapter viii - the fokker–planck equation", in *Stochastic processes in physics and chemistry (third edition)*, edited by N. VAN KAMPEN, Third Edition, North-Holland Personal Library (Elsevier, Amsterdam, 2007), pp. 193–218.

[101]"Preface to the third edition", in *Stochastic processes in physics and chemistry (third edition)*, edited by N. VAN KAMPEN, Third Edition, North-Holland Personal Library (Elsevier, Amsterdam, 2007), p. xi.

[102]R. Vreeker, L. L. Hoekstra, D. C. den Boer, and W. G. M. Agterof, "Fractal aggregation of whey proteins", Food Hydrocoll. **6**, 423–435 (1992).

[103]P. Wiltzius, "Hydrodynamic behavior of fractal aggregates", Phys. Rev. Lett. **58**, 710–713 (1987).

[104]T. A. Witten and L. M. Sander, "Diffusion-limited aggregation, a kinetic critical phenomenon", Phys. Rev. Lett. **47**, 1400–1403 (1981).

[105]H. Yamakawa, "Transport properties of polymer chains in dilute solution: hydrodynamic interaction", J. Chem. Phys. **53**, 436–443 (1970).

[106] E. Yoo, S. Khatri, and F. Blanchette, "Hydrodynamic forces on randomly formed marine aggregates", Phys. Rev. Fluids **5**, 044305 (2020).

[107] A. Zaccone, M. Soos, M. Lattuada, H. Wu, M. U. Bäbler, and M. Morbidelli, "Breakup of dense colloidal aggregates under hydrodynamic stresses", Physical Review E **79**, 061401 (2009).

[108] J. de Zarate and J. Sengers, *Hydrodynamic fluctuations in fluids and fluid mixtures* (Elsevier Science, 2006).

[109] W. Zhang, A. Almgren, V. Beckner, J. Bell, J. Blaschke, C. Chan, M. Day, B. Friesen, K. Gott, D. Graves, M. P. Katz, A. Myers, T. Nguyen, A. Nonaka, M. Rosso, S. Williams, and M. Zingale, "Amrex: a framework for block-structured adaptive mesh refinement", J. Open Source Softw. **4**, 1370 (2019).

[110] W. Zhang, A. Myers, K. Gott, A. S. Almgren, and J. B. Bell, "Amrex: block-structured adaptive mesh refinement for multiphysics applications", CoRR **abs/2009.12009** (2020).

[111] K. Zhao, B. Vowinckel, T.-J. Hsu, B. Bai, and E. Meiburg, "Cohesive sediment: intermediate shear produces maximum aggregate size", Journal of Fluid Mechanics **965**, A5 (2023).

[112] C. Ziegler, A. Wolf, W. Liu, A.-K. Herrmann, N. Gaponik, and A. Eychmüller, "Modern inorganic aerogels", Ang. Chem. Int. Ed. **56**, 13200–13221 (2017).

A

Appendix for Chapter 2

A.1 Chemistry Formulation Based on Partial Pressures

In Section 2.3, our chemistry formulation is presented in terms of molar concentrations $[X_s]$. Equivalently, it can be given in terms of partial pressures $P_s = [X_s]RT$. In this section, we summarize the corresponding expressions for our main results. Here we assume that the equilibrium constant $\overline{K}_r$ and rate constants $\overline{k}_r^{\pm}$ are defined in terms of P_s/P^{st} so that

$$\overline{K}_r = \prod_{s=1}^{N_{\text{spec}}} \frac{(P_s/P^{st})^{\nu_{sr}^-}}{(P_s/P^{st})^{\nu_{sr}^+}} \quad \text{at equilibrium,} \tag{A.1}$$

$$a_r^{\pm} = \overline{k}_r^{\pm} \prod_{s=1}^{N_{\text{spec}}} (P_s/P^{st})^{\nu_{sr}^{\pm}}. \tag{A.2}$$

Note that these partial pressure based quantities are related to the corresponding molar concentration based quantities as

$$\overline{K}_r(T) = K_r(T) \left(\frac{RT}{P^{st}}\right)^{\Delta n_r}, \quad \overline{k}_r^{\pm}(T) = k_r^{\pm}(T) \left(\frac{RT}{P^{st}}\right)^{-n_r^{\pm}}, \tag{A.3}$$

where $\Delta n_r = \sum_{s=1}^{N_{\text{spec}}} \nu_{sr}$ and $n_r^{\pm} = \sum_{s=1}^{N_{\text{spec}}} \nu_{sr}^{\pm}$.

When partial pressures are employed instead of molar concentrations, it is more convenient to use $\overline{\mu}_s^{\circ}(T)$ instead of $\mu_s^{\circ}(T)$, see Eq. (2.11). Note that these quantities satisfy

$$\overline{\mu}_s^{\circ}(T) = \mu_s^{\circ}(T) + \frac{RT}{M_s} \log \frac{P^{st}}{RT}. \tag{A.4}$$

In the resulting expressions for $\overline{K}_r$ and $\overline{k}_r^{\pm}$ for the general case considered in Section 2.3.1, the per-particle chemical potential $\hat{\mu}_s^{\circ}(T)$ is replaced by $\hat{\overline{\mu}}_s^{\circ}(T) = (M_s/RT)\overline{\mu}_s^{\circ}(T)$. Specifically, Eqs. (2.15) and (2.18) become respectively

$$\overline{K}_r(T) = \exp\left(-\sum_{s=1}^{N_{\text{spec}}} \nu_{sr} \hat{\overline{\mu}}_s^{\circ}(T)\right), \tag{A.5}$$

$$\overline{k}_r^{\pm}(T) = \lambda_r(T) \exp\left(\sum_{s=1}^{N_{\text{spec}}} \nu_{sr}^{\pm} \hat{\overline{\mu}}_s^{\circ}(T)\right). \tag{A.6}$$

For the constant heat capacity model considered in Section 2.3.2, Eq. (2.32) becomes

$$\hat{\overline{\mu}}_s^{\circ}(T) - \hat{\overline{\mu}}_s^{\circ}(T^{st}) = \frac{M_s \epsilon_s}{R}\left(\frac{1}{T} - \frac{1}{T^{st}}\right) - \hat{c}_{p,s} \log \frac{T}{T^{st}}, \tag{A.7}$$

where $\hat{c}_{p,s} = (M_s/R)c_{p,s}$. Thus, Eq. (2.33) becomes

$$\overline{K}_r(T) = \overline{K}_r(T^{st}) \exp\left[-\frac{\overline{A}_r}{R}\left(\frac{1}{T} - \frac{1}{T^{st}}\right)\right]\left(\frac{T}{T^{st}}\right)^{\overline{B}_r}, \tag{A.8}$$

where $\overline{A}_r = A_r$ and $\overline{B}_r = B_r + \Delta n_r$. Finally, when the rate constants are given in the form of the modified Arrhenius equation,

$$\overline{k}_r^{\pm}(T) = \overline{k}_r^{\pm}(T^{st}) \exp\left[-\frac{\overline{\alpha}_r^{\pm}}{R}\left(\frac{1}{T} - \frac{1}{T^{st}}\right)\right]\left(\frac{T}{T^{st}}\right)^{\overline{\beta}_r^{\pm}}, \tag{A.9}$$

the parameters $\overline{\alpha}^{\pm}$ and $\overline{\beta}^{\pm}$ must satisfy

$$\overline{\alpha}_r^- = \overline{\alpha}_r^+ - \overline{A}_r, \quad \overline{\beta}_r^- = \overline{\beta}_r^+ - \overline{B}_r, \tag{A.10}$$

for thermodynamic consistency.

A.2 Structure Factor Analysis for Dimerization

For a one-dimensional two-species ideal gas mixture undergoing a reversible dimerization reaction at equilibrium, we show that our chemistry formulation gives the correct flat structure factor spectra as predicted by the equilibrium statistical mechanics. Following the fact that adding chemical reactions should not change the thermodynamic equilibrium state of the system, we show that the correct equilibrium structure factor

spectra established by nonreactive FHD are not disturbed by the inclusion of our chemistry model. Here, we denote transpose and complex transpose by $(\cdot)^T$ and $(\cdot)^*$, respectively.

We first consider the nonreactive system. For our purposes, let $\mathbf{U} = [\delta\rho_1, \delta\rho_2, v, \delta T]^T$, where $\delta\rho_s = \rho_s - \rho_s^{eq}$ and $\delta T = T - T^{eq}$. Like a one-species system [2], the linearized FHD equations for a two-species system can be written as

$$\frac{\partial}{\partial t}\mathbf{U} = -\frac{\partial}{\partial x}\left(\mathbf{A}_1\mathbf{U}\right) + \frac{\partial^2}{\partial x^2}\left(\mathbf{A}_2\mathbf{U}\right) + \frac{\partial}{\partial x}\left(\mathbf{B}\boldsymbol{\mathcal{Z}}\right), \tag{A.11}$$

where the first, second, and third terms in the right-hand side correspond to hyperbolic, dissipative, and stochastic fluxes, respectively, and $\boldsymbol{\mathcal{Z}}$ is a collection of independent standard Gaussian white noise fields. Since transport coefficients are dependent on composition [15], it is possible but tedious to derive explicit expressions of $\mathbf{A}_1$, $\mathbf{A}_2$, and $\mathbf{B}$. Note, however, that we do not need explicit expressions. Instead, we assume that the linearized FHD equations (A.11) guarantees thermodynamic consistency. In other words, the following equation [2], from which the structure factors $\mathbf{S}(k) = V\langle\widehat{\mathbf{U}}_k\widehat{\mathbf{U}}_k^*\rangle$ can be determined,

$$\left(-ik\mathbf{A}_1 - k^2\mathbf{A}_2\right)\mathbf{S}(k) + \mathbf{S}(k)\left(ik\mathbf{A}_1^T - k^2\mathbf{A}_2^T\right) + \mathbf{B}\mathbf{B}^T = 0, \tag{A.12}$$

is satisfied by the correct structure factors $\mathbf{S}^{eq}$, which are obtained from the equilibrium statistical mechanics [15, 13]:

$$\mathbf{S}^{eq} = \mathrm{diag}\left(\frac{M_1}{N_A}\rho_1^{eq}, \frac{M_2}{N_A}\rho_2^{eq}, \frac{k_B T^{eq}}{\rho_1^{eq} + \rho_2^{eq}}, \frac{k_B (T^{eq})^2}{c_{v,1}\rho_1^{eq} + c_{v,2}\rho_2^{eq}}\right). \tag{A.13}$$

We now consider the reactive system undergoing dimerization. By using $M_1\Omega_1 = -M_2\Omega_2$ and expressing $\partial(\delta T)/\partial t$ in terms of $\partial\rho_s/\partial t$ and $\partial(\rho E)/\partial t$, we write the linearized FHD equations as

$$\frac{\partial}{\partial t}\mathbf{U} = \mathbf{A}_0\mathbf{U} - \frac{\partial}{\partial x}\left(\mathbf{A}_1\mathbf{U}\right) + \frac{\partial^2}{\partial x^2}\left(\mathbf{A}_2\mathbf{U}\right) + \frac{\partial}{\partial x}\left(\mathbf{B}\boldsymbol{\mathcal{Z}}\right) + \mathbf{b}z, \tag{A.14}$$

Here, z is a standard Gaussian white noise field and the additional terms are given as

$$\mathbf{A}_0\mathbf{U} = M_2\overline{\Omega}_2\begin{bmatrix}-1\\1\\0\\\phi\end{bmatrix}, \quad \mathbf{b}z = M_2\widetilde{\Omega}_2\begin{bmatrix}-1\\1\\0\\\phi\end{bmatrix}, \tag{A.15}$$

where

$$\phi = \frac{(\epsilon_1 - \epsilon_2) + (c_{v,1} - c_{v,2})T^{eq}}{c_{v,1}\rho_1^{eq} + c_{v,2}\rho_2^{eq}}. \tag{A.16}$$

To derive explicit expressions of $\mathbf{A}_0$ and $\mathbf{b}$, we linearize the rate constants,

$$k^\pm(T) = k_{eq}^\pm \left\{ 1 + \left(\frac{\alpha^\pm}{RT^{eq}} + \beta^\pm \right) \frac{\delta T}{T^{eq}} \right\}, \tag{A.17}$$

where $k_{eq}^\pm = k^\pm(T^{eq})$, and obtain

$$M_2 \overline{\Omega}_2 = k_{eq}^- \rho_2^{eq} \left\{ 2 \frac{\delta \rho_1}{\rho_1^{eq}} - \frac{\delta \rho_2}{\rho_2^{eq}} + \psi \frac{\delta T}{T^{eq}} \right\}, \quad \text{where } \psi = \frac{A}{RT^{eq}} + B, \tag{A.18}$$

$$M_2 \widetilde{\Omega}_2 = \sqrt{2 \frac{M_2}{N_A} k_{eq}^- \rho_2^{eq}} \ z. \tag{A.19}$$

Thus, we finally obtain

$$\mathbf{A}_0 = k_{eq}^- \rho_2^{eq} \begin{bmatrix} -\frac{2}{\rho_1^{eq}} & \frac{1}{\rho_2^{eq}} & 0 & -\frac{\psi}{T^{eq}} \\ \frac{2}{\rho_1^{eq}} & -\frac{1}{\rho_2^{eq}} & 0 & \frac{\psi}{T^{eq}} \\ 0 & 0 & 0 & 0 \\ \frac{2\phi}{\rho_1^{eq}} & -\frac{\phi}{\rho_2^{eq}} & 0 & \frac{\phi\psi}{T^{eq}} \end{bmatrix}, \quad \mathbf{b} = \sqrt{2 \frac{M_2}{N_A} k_{eq}^- \rho_2^{eq}} \begin{bmatrix} -1 \\ 1 \\ 0 \\ \phi \end{bmatrix}. \tag{A.20}$$

The structure factors $\mathbf{S}(k)$ resulting from Eq. (A.14) can be determined by

$$\left(\mathbf{A}_0 - ik\mathbf{A}_1 - k^2 \mathbf{A}_2 \right) \mathbf{S}(k) + \mathbf{S}(k) \left(\mathbf{A}_0^T + ik\mathbf{A}_1^T - k^2 \mathbf{A}_2^T \right) + \mathbf{B}\mathbf{B}^T + \mathbf{b}\mathbf{b}^T = 0. \tag{A.21}$$

Hence, if the following condition is satisfied by $\mathbf{S}^{eq}$, $\mathbf{A}_0$, and $\mathbf{b}$,

$$\mathbf{A}_0 \mathbf{S}^{eq} + \mathbf{S}^{eq} \mathbf{A}_0^T + \mathbf{b}\mathbf{b}^T = 0, \tag{A.22}$$

by combining that Eq. (A.12) is satisfied by $\mathbf{S}^{eq}$, one can show that $\mathbf{S}^{eq}$ satisfies Eq. (A.21). By using explicit expressions of $\mathbf{S}^{eq}$, $\mathbf{A}_0$, and $\mathbf{b}$ (see Eqs. (A.13) and (A.20)), one can easily show that Eq. (A.22) holds. Therefore, our chemistry formulation gives the correct structure factors.

We have a couple of remarks for this analysis. First, by comparing Eq. (A.12) (nonreactive case) and Eq. (A.21) (reactive case), one can predict that errors in the structure factors appear at small k values if a thermodynamically-inconsistent chemistry formulation is used. This is because the contribution of the additional reactive terms containing $\mathbf{A}_0$ and $\mathbf{b}$ becomes less significant in Eq. (A.21) for larger k values and the two equations becomes the same asymptotically in the large k limit. Second, using the definitions of A and B (see Eq. (2.34)), one can show that

$$\psi = -\frac{M_2}{RT^{eq}} \left(c_{v,1} \rho_1^{eq} + c_{v,2} \rho_2^{eq} \right) \phi. \tag{A.23}$$

Hence, if $\epsilon_1 + c_{v,1}T^{eq} = \epsilon_2 + c_{v,2}T^{eq}$, that is, the specific internal energies of A and A_2 coincide, both ψ and ϕ become zero. In this special case, the temperature dependence in $\mathbf{A}_0$ and $\mathbf{b}$ disappears but thermodynamic consistency is still maintained. Similarly, simple models, such as the Brusselator, that use "color chemistry" (species are thermally indistinguishable) are themodynamically consistent despite using constant rates.

A.3   Numerical Scheme

In this section, we describe the numerical method used to solve the FNS equations (2.1a)-(2.1c) for reactive gas mixtures. We will focus our discussion on the temporal integrator used, and refer the interested reader to Ref. [94] for a detailed description of the spatial discretization, implemented using the Finite Volume method on a staggered-grid. We note that our numerical approach takes advantage of the AMReX framework [109], which allows for massive parallelization and GPU-accelerated performance.

The fluctuating Navier–Stokes (FNS) equations [13, 18]:

$$\frac{\partial \rho_s}{\partial t} = -\nabla \cdot (\rho_s \mathbf{u}) - \nabla \cdot \boldsymbol{\mathcal{F}}_s + m_s \Omega_s, \tag{A.24a}$$

$$\frac{\partial (\rho \mathbf{u})}{\partial t} = -\nabla \cdot (\rho \mathbf{u}\mathbf{u}^T) - \nabla P - \nabla \cdot \mathbf{\Pi}, \tag{A.24b}$$

$$\frac{\partial (\rho E)}{\partial t} = -\nabla \cdot (\rho E \mathbf{u} + P\mathbf{u}) - \nabla \cdot \boldsymbol{\mathcal{Q}} - \nabla \cdot (\mathbf{\Pi} \cdot \mathbf{u}). \tag{A.24c}$$

can be written in a more compact form

$$\partial_t \mathbf{U} = -\nabla \cdot \mathbf{F}_H - \nabla \cdot \mathbf{F}_D - \nabla \cdot \mathbf{F}_S + \mathbf{H} \equiv \mathbf{R}(\mathbf{U}, Z), \tag{A.25}$$

where $\mathbf{U} = [\rho_s, \rho\mathbf{u}, \rho E]$ is the set of hydrodynamic variables, while $\mathbf{F}_H$, $\mathbf{F}_D$ and $\mathbf{F}_S$ are

$$\mathbf{F}_H = \begin{bmatrix} \rho_s \mathbf{u} \\ \rho \mathbf{u}\mathbf{u}^T + P \\ \mathbf{u}(\rho E + P) \end{bmatrix}, \quad \mathbf{F}_D = \begin{bmatrix} \overline{\boldsymbol{\mathcal{F}}}_s \\ \overline{\mathbf{\Pi}} \\ \overline{\boldsymbol{\mathcal{Q}}} + \overline{\mathbf{\Pi}} \cdot \mathbf{u} \end{bmatrix}, \tag{A.26}$$

$$\mathbf{F}_S = \begin{bmatrix} \widetilde{\boldsymbol{\mathcal{F}}}_s \\ \widetilde{\mathbf{\Pi}} \\ \widetilde{\boldsymbol{\mathcal{Q}}} + \widetilde{\mathbf{\Pi}} \cdot \mathbf{u} \end{bmatrix}, \tag{A.27}$$

and represent the hyperbolic, diffusive and stochastic fluxes, respectively. The term $\mathbf{H}$ embeds all the external forcing, and in this work on reactive chemistry takes the form

$\mathbf{H} = [\Omega_s, \mathbf{0}, 0]^T$. The right-hand side of eq. (A.25) is written as $\mathbf{R}(\mathbf{U}, Z)$, where Z is the spatiotemporal discretization of the Gaussian white noise (GWN) field $\mathcal{W}$. For temporal integration, we use a three-stage, low-storage Runge–Kutta (RK3) scheme [2], in which the stochastic fields are discretized in time so that only two GWN fields, say Z^A and Z^B, are required. Note that these fields are generated independently in each FHD cell at the beginning of each time step. Since chemistry source terms are given in the form of Langevin equation, they are readily incorporated into the RK3 scheme. Furthermore, since the species mass densities ρ_s is discretized at the center of each FHD cell, the evaluation of the source term Ω_s occurs at the cell centers. This allows our formulation to be valid both on collocated [13] and staggered [94] grids.

The three stages of the RK3 scheme per time step can be written as follows

$$\mathbf{U}^{n+1/3} = \mathbf{U}^n + \Delta t \mathbf{R}(\mathbf{U}^n, Z_1),$$
$$\mathbf{U}^{n+2/3} = \frac{3}{4}\mathbf{U}^n + \frac{1}{4}[\mathbf{U}^{n+1/3} + \Delta t \mathbf{R}(\mathbf{U}^{n+1/3}, Z_2)],$$
$$\mathbf{U}^{n+1} = \frac{1}{3}\mathbf{U}^n + \frac{2}{3}[\mathbf{U}^{n+2/3} + \Delta t \mathbf{R}(\mathbf{U}^{n+2/3}, Z_3)],$$

where the random fields Z_i, $i = 1, 2, 3$, are defined as linear combinations of Z^A and Z^B

$$Z_1 = Z^A + \beta_1 Z^B,$$
$$Z_2 = Z^A + \beta_2 Z^B,$$
$$Z_3 = Z^A + \beta_3 Z^B.$$

$$\text{(A.28)}$$

The values of the weights β_i are $\beta_1 = (2/\sqrt{2} + \sqrt{3})/5$, $\beta_2 = (-4/\sqrt{2} + 3\sqrt{3})/5$ and $\beta_3 = (2 - 2\sqrt{3})/10$, to guarantee weak second-order accuracy, following Ref. [2].

A.4 Numerical Results
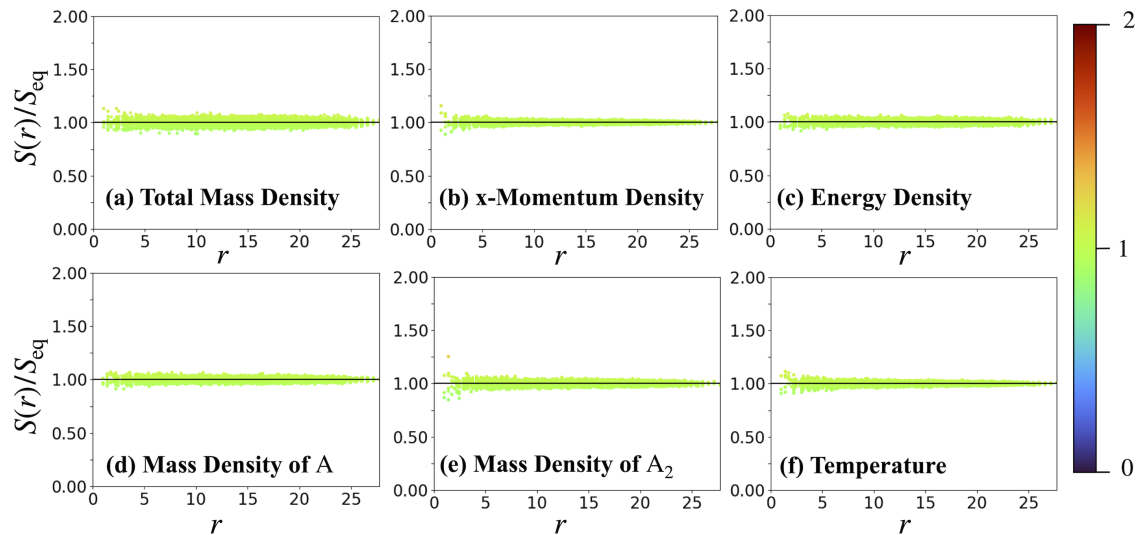
A.4.1 Nonreactive FHD

Figure A.1: Equilibrium structure factor spectra obtained from non-reactive FHD. For various field variables, the structure factor values $S(\mathbf{k})$ are normalized by the theoretical values S_{eq} and plotted versus $r = \sqrt{\kappa_x^2 + \kappa_y^2 + \kappa_z^2}$, where $\kappa_i = k_i \left(\frac{2\pi}{L}\right)^{-1}$ is the integer wave index in the i-direction. Panels show the structure factors for (a) ρ, (b) ρu_x, (c) ρE, (d) ρ_1, (e) ρ_2, and (f) T. Each data point is colored based on its normalized value $S(r)/S_{eq}$ (see the color bar). The horizontal black line is drawn at the expected theoretical value for visual clarity.

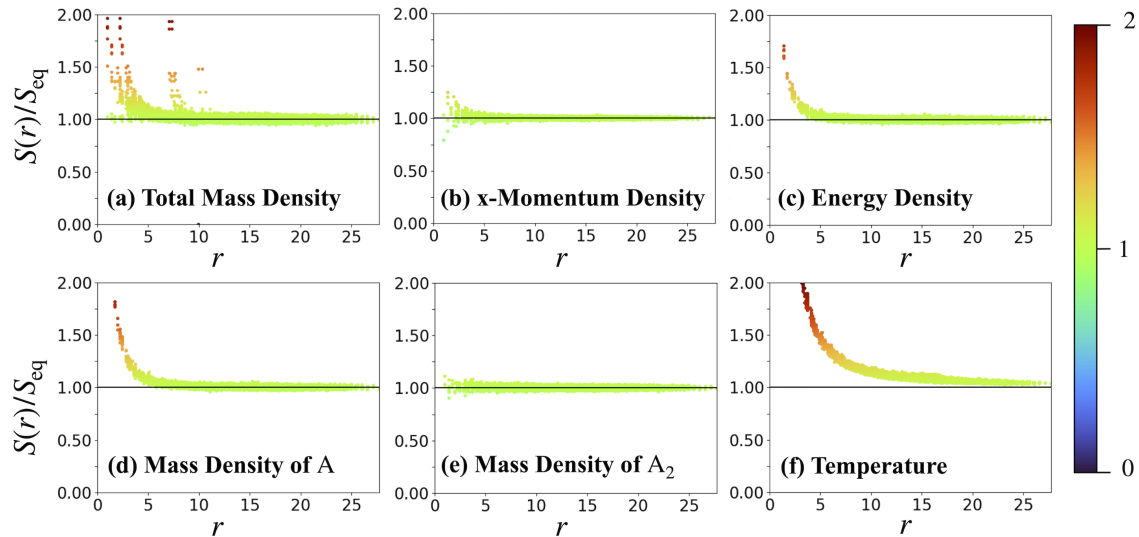## A.4.2 Temperature Independent Rate Constants

Figure A.2:   Equilibrium structure factor spectra obtained from reactive FHD based on the temperature-independent rate constants formulation of reactive chemistry. For various field variables, the structure factor values $S(\mathbf{k})$ are normalized by the theoretical values S_{eq} and plotted versus $r = \sqrt{\kappa_x^2 + \kappa_y^2 + \kappa_z^2}$, where $\kappa_i = k_i \left(\frac{2\pi}{L}\right)^{-1}$ is the integer wave index in the i-direction. Panels show the structure factors for (a) ρ, (b) ρu_x, (c) ρE, (d) ρ_1, (e) ρ_2, and (f) T. Each data point is colored based on its normalized value $S(r)/S_{eq}$ (see the color bar). The horizontal black line is drawn at the expected theoretical value for visual clarity.

Appendix B

Appendix

Appendix for Chapter 4

B.1 Derivation of formulation to account for background flow

Following Ref. [83], the velocity of a flow computed on a point outside, inside or on the surface of a solid object can be written as

$$u_j(x_0) = -\frac{1}{8\pi\mu} \int_S f_i(x) G_{ij}(x, x_0) dS(x) + \frac{1}{8\pi} \int_S u_i(x) T_{ijk}(x, x_0) n_k(x) dS(x). \quad \text{(B.1)}$$

Here the indices represent Einstein notation. In general $\vec{x}_0$ can be outside of S, inside the volume whose boundary is S, or on S. Since we are interested in computing the stresses on the surface of the object, we will denote with $\vec{x}_s$ any point that lie on the surface of the aggregates, whereas $\vec{x}_0$ will denote points that lie outside of the surface of the aggregates. Furthermore, in our formulation, $\vec{x}_s$ will always correspond to the center of the face of a cube. Finally, we introduce a disturbance flow, caused by the presence of a solid object in a fluid, and define its velocity to be $\vec{u}^D = \vec{V} + \vec{\Omega} \wedge \vec{x} - \vec{u}^\infty$, where $\vec{u}^\infty$ represents the fluid's velocity in absence of the object. In summary,

- $\vec{u}$ is what we call the *true velocity*
- $\vec{u}^\infty$ is the *background flow*
- $\vec{u}^D$ is a *disturbance flow* such that $\vec{u}^D = \vec{u} - \vec{u}^\infty$
- S is the *surface* of the aggregate
- $\vec{x}_0$ is a point *outside* of the aggregate

- $\vec{x}_{\mathrm{s}}$ is a point *on the surface* of the aggregate

Re-writing eq. (B.1) in terms of $\vec{u}^D$ yields

$$u_j^D(x_0) = -\frac{1}{8\pi\mu}\int_S f_i^D(x)G_{ij}(x,x_0)dS(x) + \frac{1}{8\pi}\int_S u_i^D(x)T_{ijk}(x,x_0)n_k(x)dS(x). \quad \text{(B.2)}$$

Then, we compute (B.2) in the limit where $\vec{x}_0 \to \vec{x}_{\mathrm{s}}$. In general, while the single layer is always continuous, the integral with the double layer introduces a singularity. Thus, we will use the fact that, from [83] we know that

$$\lim_{\vec{x}_0\to\vec{x}_{\mathrm{s}}}\int_S u_i(x)T_{ijk}(x,x_0)n_k(x)dS(x) = \pm 4\pi u_j(x_{\mathrm{s}}) + \int_S^{PV} u_i(x)T_{ijk}(x,x_{\mathrm{s}})n_k(x)dS(x),$$
$$\text{(B.3)}$$

where PV indicates that the integral is evaluated in the Principle Value sense. The $\pm$ of the first term on the right-hand side, corresponds to the cases where $\vec{x}_0$ approaches S from outside the object (+), or from inside (-), in the direction of the normal. Since we are using the outward pointing normal in our formulation, we will limit our discussion to (+) case. Thus, taking the limit for $\vec{x}_0 \to \vec{x}_{\mathrm{s}}$ on both sides of eq. (B.2) yields

$$u_j^D(x_{\mathrm{s}}) = -\frac{1}{8\pi}\int_S f_i^D(x)G_{ij}(x,x_{\mathrm{s}})dS(x) \qquad\qquad \text{(B.4)}$$
$$+ \frac{1}{8\pi}\left(4\pi u_j^D(x_{\mathrm{s}}) + \int_S^{PV} u_i^D(x)T_{ijk}(x,x_{\mathrm{s}})n_k(x)dS(x)\right),$$

which, after simplification becomes

$$u_j^D(x_{\mathrm{s}}) = -\frac{1}{8\pi}\int_S f_i^D(x)G_{ij}(x,x_{\mathrm{s}})dS(x) \qquad\qquad \text{(B.5)}$$
$$+ \frac{1}{2}u_j^D(x_{\mathrm{s}}) + \frac{1}{8\pi}\int_S^{PV} u_i^D(x)T_{ijk}(x,x_{\mathrm{s}})n_k(x)dS(x).$$

Now we plug in $\vec{u}^D = \vec{V} + \vec{\Omega}\wedge\vec{x} - \vec{u}^\infty$ on both sides, and use the identities [83]

$$\int_S \vec{V}\cdot\bar{\bar{T}}(\vec{x},\vec{x}_{\mathrm{s}})\cdot\hat{n}dS(\vec{x}) = -4\pi\vec{V}, \quad \int_S(\vec{\Omega}\wedge\vec{x}_{\mathrm{s}})\cdot\bar{\bar{T}}(\vec{x},\vec{x}_{\mathrm{s}})\cdot\hat{n}dS(\vec{x}) = -4\pi\vec{\Omega}\wedge\vec{x}_{\mathrm{s}} \quad \text{(B.6)}$$

to solve the double layer integrals for the solid body motion part. This yields

$$\vec{V} + \vec{\Omega}\wedge\vec{x}_{\mathrm{s}} - \vec{u}^\infty(\vec{x}_{\mathrm{s}}) = -\frac{1}{8\pi\mu}\int_S f_i^D(x)G_{ij}(x,x_s)dS(x)$$
$$+ \frac{1}{2}(\vec{V} + \vec{\Omega}\wedge\vec{x}_{\mathrm{s}} - \vec{u}^\infty(\vec{x}_{\mathrm{s}}))$$
$$+ \frac{1}{8\pi}\left(-4\pi(\vec{V} + \vec{\Omega}\wedge\vec{x}_{\mathrm{s}}) - \int_S^{PV} u_i^\infty(x)T_{ijk}(x,x_s)n_k(x)dS(x)\right).$$
$$\text{(B.7)}$$

After simplification and rearranging terms, we obtain

$$\vec{V} + \vec{\Omega} \wedge \vec{x}_s + \frac{1}{8\pi\mu} \int_S f_i^D(x) G_{ij}(x, x_s) dS(x) = \frac{1}{2} u^\infty(x_s) \tag{B.8}$$

$$- \frac{1}{8\pi} \int_S^{PV} u_i^\infty(x) T_{ijk}(x, x_s) n_k(x) dS(x), \tag{B.9}$$

which, along with the equations for Torque and Force, will give the linear system (4.10) that we solve for $\vec{V}$, $\vec{\Omega}$ and the external stresses $\vec{f}^D$.